Site U1326[1]

Expedition 311 Scientists[2]

Chapter contents

Background and objectives

Site U1326 (proposed Site CAS-03C; Collett et al., 2005) is located on top of the first uplifted ridge of accreted sediments along the margin-perpendicular transect established during Integrated Ocean Drilling Program (IODP) Expedition 311 (Fig. F3 in the "Expedition 311 summary" chapter). The newly acquired bathymetry data from the University of Washington show a collapse structure near the originally proposed Site CAS-03B (Collett, Riedel, Malone, et al., 2005) that was previously unrecognized (Fig. F5 in the "Expedition 311 summary" chapter). A map with the site survey seismic data acquired in the area is shown in Figure F1. We switched former alternate Site CAS-03C to the primary site to avoid coring into the slump feature because it may locally complicate the history of deposition, fluid flux, and related gas hydrate formation.

The head wall of the slump feature is ~250 m high and the slump has eroded a ~2.5 km long section into the ridge. Slump material can be identified in the bathymetry data and previously in SeaMARCII acoustic imagery (Davis et al., 1987). Because of the steep slope, it is difficult to seismically image the deposit. A striking characteristic of the ridge is the occurrence of several linear features crossing the ridge in an east–west direction (Fig. F5 in the "Expedition 311 summary" chapter). These linear features are clearly associated with faults as seen in Figure F2. The faults outcrop at the seafloor and generate a seafloor displacement of as much as 25 m. These faults can be seismically traced from the surface down through the sedimentary section to depths below the bottom-simulating reflector (BSR). The occurrence of the faults is limited to the location of the slump scar, and the ridge heals to either end at the southeast and northwest limits, where the sediments are not faulted but appear seafloor parallel. Overall, the seismic character of the ridge changes from the southwest to the northeast across the ridge, with the southwest-facing part of the ridge characterized by strong, semicontinuous reflectivity (Figs. F3, F4), whereas the seismic reflectivity disappears underneath the northeast-facing flank of the ridge (Fig. F5). The slopes on the flanks of the ridge are relatively steep, making seismic imaging challenging, but the ridge is generally symmetrical so the differences in the seismic character of the ridge cannot be explained by simple variable acquisition parameters. It is possible that the internal deformation of the sediments may increase toward the northwest-facing flank and results in a loss of seismic coherency similar to that observed in accreted sediments along this margin.

[1] Expedition 311 Scientists, 2006. Site U1326. *In* Riedel, M., Collett, T.S., Malone, M.J., and the Expedition 311 Scientists. *Proc. IODP,* 311: Washington, DC (Integrated Ocean Drilling Program Management International, Inc.). doi:10.2204/iodp.proc.311.104.2006
[2] Expedition 311 Scientists' addresses.

doi:10.2204/iodp.proc.311.104.2006

A BSR is present underneath most of the ridge, especially seen in the lower frequency seismic data (Fig. F3). However, the multichannel seismic data along Line PGC9902_CAS03a show that the BSR is practically absent underneath the slump feature where the most heavily faulted sediments occur. As a result of the complicated nature of the seafloor, imaging capabilities may be limited especially in the high-frequency data (see Fig. F4 in the "Site U1328" chapter).

The coring and logging objectives at this site were tied to completing the transect of scientific drill sites across the northern Cascadia margin near Vancouver Island. Site U1326 is the closet location to the deformation front and probably represents the tectonically youngest occurrence of gas hydrate on the northern Cascadia margin.

At this western end-member site of gas hydrate evolution in the accretionary prism, the objectives include

- Studying the distribution of gas hydrate,
- Defining the nature of the BSR,
- Developing baseline geochemical and microbiological profiles, and
- Obtaining data needed to ground-truth remotely acquired imaging techniques such as seismic or controlled-source electromagnetic (CSEM) surveys.

The operational plan to achieve these objectives was based on a general three-hole concept, which includes

- A logging-while-drilling/measurement-while-drilling (LWD/MWD) hole;
- A continuously cored hole to characterize geochemical and microbiological baselines and proxies for gas hydrate;
- An additional "tools" hole for specialized pressure coring systems, including the IODP Pressure Core Sampler (PCS) and the HYACINTH Fugro Pressure Corer (FPC) and HYACE Rotary Corer (HRC) systems, combined with selected spot-coring using the conventional extended core barrel (XCB) system; and
- A wireline logging program in the tools hole using the triple combination and Formation MicroScanner-sonic tool strings.

Operations

Hole U1326A

After transiting in dynamic positioning (DP) mode from Hole U1325A and downloading the data from the LWD/MWD tools, the LWD/MWD bottom-hole assembly (BHA) was tripped to the seafloor. Hole U1326A (proposed Site CAS-03C; Collett et al., 2005) was spudded at 1445 h on 22 September 2005 at an estimated seafloor depth of 1828.1 meters below sea level (mbsl; 1839.0 meters below rig floor [mbrf]). To avoid blowing out the top of the hole, we changed the spud-in parameters to 100 gallons per minute (gpm) circulation with 10–15 rpm rotation. At 10 meters below seafloor (mbsf), top drive rotation was increased to 40 rpm. At 29 mbsf, parameters were increased to maintain a 50 m/h rate of penetration (ROP) with a minimum circulation of 270 gpm. The LWD/MWD safety protocol was followed without incident and required no corrective action (see **"Downhole logging"** in the "Methods" chapter). The hole was drilled to a total depth (TD) of 300 mbsf. After displacing the hole with 10.5 ppg sepiolite mud, the drill string was pulled clear of the seafloor at 0600 h on 23 September, ending operations in Hole U1326A. The pipe was pulled to a safe distance above the seafloor in preparation for the DP transit to Site U1327.

Hole U1326B

After completing Hole U1325D, we pulled the drill pipe back to ~1600 mbrf and transited ~2.8 nmi in DP mode to Site U1326. We spudded Hole U1326B at 1205 h on 23 October 2005, but the core contained only 1.55 m of sediment, which was not ideal for the planned shallow microbiological and geochemical studies. Based on recovery in Core 1H, the estimated seafloor depth is 1828.4 mbsl (1840.0 mbrf).

Hole U1326C

The bit was set at 1834 mbrf (2 m lower than in Hole U1326B), and without offsetting, Hole U1326C was spudded at 1245 h on 23 October 2005. The first core recovered 3.93 m of sediment, indicating a seafloor depth of 1828.0 mbsl (1839.6 mbrf). On the fourth advanced piston corer (APC) run (~30 mbsf), we unexpectedly hit APC refusal and switched to XCB coring. XCB coring advanced the hole to a depth of 82.7 mbsf, which was followed by three consecutive pressure core deployments within a high electrical resistivity zone identified on LWD/MWD downhole logs. The first pressure core system deployed was the FPC, which recovered a partial core (15 cm) at less than full pressure (see **"Pressure coring"**). The second system to be deployed was the PCS, which recovered a partial core under pressure. The third pressure core system deployed was the HRC, which was damaged at the bottom of the hole because of excessive ship heave (>4 m) and packing of formation sands around the outer barrel. The HRC cutting shoe and a spacer

section came unscrewed and were left in the hole, which resulted in the termination of Hole U1326C at a TD of 86.7 mbsf.

Hole U1326D

After tripping the BHA back to the seafloor, the ship was moved 30 m southwest (15 m southwest of Hole U1326A) (Fig. F6). Hole U1326D was spudded at 1130 h on 24 October 2005 and drilled to a depth of 78.8 mbsf in preparation for continued coring operations. Because of problems associated with heave, which worsened throughout the day, we decided to suspend all pressure coring operations for the remainder of the expedition to avoid the possibility of damaging the tools and losing the last hole with little operational time remaining. XCB coring deepened the hole to 271.4 mbsf with an average recovery of 63.3% (Table T1). With forecasts of deteriorating weather conditions on the morning of 26 October, it was decided to stop coring at a depth of 271.4 mbsf and deepen the hole to a TD of 300 mbsf by drilling, which allowed us to gain time and complete logging, rigging down, and securing the rig floor before the expected arrival of the forecasted storm. Despite the marginal conditions, we did attempt three deployments with the Davis-Villinger Temperature Probe (DVTP) at 252.2, 271.4, and 300 mbsf, which yielded marginally useful data.

After completing coring operations, the hole was prepared for logging with a wiper trip followed by displacing the hole with weighted mud. We decided to conduct a single downhole logging run with a nonstandard IODP tool string, which included the Scintillation Gamma Ray Tool (SGT), Phasor Dual Induction Tool (DIT), and the Dipole Sonic Imager (DSI). At 2315 h on 26 October, the tool string was deployed in the hole and lowered to 298.4 mbsf. Two successful passes were made from this depth and the tool was back on deck at 0345 h. The drill string was pulled clear of the seafloor at 0530 h on 27 October, ending operations in Hole U1326D.

Transit to Victoria, British Columbia

After tripping the drill string to the rig floor, recovering two beacons, and securing the ship for transit, we departed under deteriorating sea states (with 40–45 kt sustained winds gusting to >50 kt) at 1320 h on 27 October 2005. We made the short 157 nmi transit to Victoria in 22 h at an average speed of 7.1 kt. Expedition 311 officially concluded with the first line ashore at 1225 h on 28 October.

Lithostratigraphy

Site U1326 is located at the far western downslope end of the Expedition 311 transect, on the first uplifted ridge of accreted sediments. Three of the four holes (Holes U1326A–U1326D) at this site were cored; Hole U1326B was cored to 1.5 mbsf (1.5 m cored), Hole U1326C to 86.7 mbsf (85.7 m cored), and Hole U1326D to 300 mbsf (192.6 m cored). Recovery was excellent in Hole U1326B (103.3%) but limited in Holes U1326C (63.5%) and U1326D (63.3%).

We divided the 271.4 m thick sedimentary section recovered from Holes U1326C and U1326D into three lithostratigraphic units (Fig. F7) based on visual inspection of the cores and analysis of smear slides. Other parameters, such as mineralogy data from X-ray diffraction (XRD) analyses, helped to better define the entire stratigraphic section. The results were also compared and correlated with seismic data, downhole LWD/MWD data, and physical property measurements.

Lithostratigraphic units

Lithostratigraphic Unit I

Intervals: Sections 311-U1326B-1H-1 through 1H-CC and 311-U1326C-1H-1 through 4H-1

Depths: Hole U1326B: 0.00–1.55 mbsf and Hole U1326C: 0.00–24.13 mbsf

Age: Holocene–Pleistocene (<0.3 Ma)

Unit I is mainly composed of dark gray (N4) and dark greenish gray (5GY 4/1) silty clay and clay, and clay with diatoms (Fig. F8). Gradual color changes from dark gray to dark greenish gray are observed especially in Core 311-U1326C-3H (Fig. F8). Minor lithologies are silty clay with foraminifers, dark gray foraminifer sand, dark gray silt, silty sand, and sand layers or lenses (Fig. F9). The silt and sand layers in Sections 311-U1326C-2H-2, 2H-5 through 2H-7, 3H-1, 3H-3, 3H-4, and 4H-1 are all tilted in the same direction. The single layers show varying thickness from a few millimeters to ~10 cm. In Section 311-U1326C-2H-2, layers show coarsening-upward sequences. The major nonbiogenic components of Unit I are clay minerals, quartz, feldspar, opaque minerals, accessory minerals, biotite, and some rock fragments. Rare to moderate sulfide mottling, appearing as dark gray (N4) stains, occurs in Sections 311-U1326C-1H-2, 2H-2, 2H-4, 2H-5, 3H-1, and 3H-3 through 3H-6. Small sulfide concretions (<2 mm) are present in Sections 311-U1326C-1H-2, 2H-5, and 2H-6.

The major biogenic components of Unit I are diatoms (as much as 10% in Sample 311-U1326C-3H-6, 90 cm). Foraminifers occur as well and are especially abundant (35%) in Sample 311-U1326C-1H-2, 40 cm. Visibly observed foraminifers occur in Section 311-U1326C-1H-CC. Bivalve shell fragments are ob-

served in Sections 311-U1326C-1H-2 (Fig. F10) and 3H-5, and sponge spicules are seen in Sections 311-U1326C-3H-4 and 3H-5.

Some small sedimentary structures related to soft-sediment deformation are observed in Section 311-U1326C-2H-5. Greenish patches, rich in glauconite, are present in intervals 311-U1326C-1H-2, 30–65 cm; 2H-4, 15–65 cm; and 2H-5, 0–10 cm. Unlithified carbonate cement, as well as partly lithified carbonate, is observed in intervals 311-U1326B-1H-1, 95–102 cm (nonstoichiometric dolomite; 46 mol% $MgCO_3$) (Fig. F11); 1H-1, 149–150 cm (Fig. F12); and 1H-2, 62–64 cm. Some small concretions (millimeter scale) are present in Section 311-U1326C-3H-1. The Unit I/II boundary is marked by the disappearance of diatoms and calcareous fossils and an increase in silty and sandy layers in the minor lithology.

Lithostratigraphic Unit II

Intervals: Sections 311-U1326C-4H-1 through 10X-CC and 311-U1326D-2X-1 through 7X-CC

Depths: Hole U1326C: 24.13–82.70 mbsf and Hole U1326D: 88.40–146.30

Age: Pleistocene (>0.3 Ma)

Unit II is composed of dark gray (N4) clay and silty clay and dark olive-gray (5Y 3/2) clay locally interbedded with dark gray (N4) silt, silty sand, and sand layers (Fig. F13). In the lower part of Unit II, some sand patches occur within clay or silty clay (Fig. F14). Some silty or sandy layers show fining-upward sequences in Sections 311-U1326C-6X-4, 7X-2, 9X-2, 311-U1326D-2X-4, and 7X-3. Parallel laminations are present in Sections 311-U1326C-6X-5 and 311-U1326D-3X-5. Silt laminae are observed in Sections 311-U1326D-9X-4 and 10X-1.

The major nonbiogenic components of Unit II are clay minerals, quartz, feldspar, accessory minerals (mainly amphibole), opaque minerals, and biotite. Rare sulfide mottling is observed in the upper (Sections 311-U1326C-5X-1 and 5X-3) and lower (Sections 311-U1326D-5X-1, 5X-4, 6X-3, 6X-CC, and 7X-3) part of this unit. Sulfide concretions are present in Sections 311-U1326D-5X-1 and 5X-2. Dropstones (<1.5 cm) are found in the lower part of Unit II (Sections 311-U1326D-4X-4, 4X-5, 5X-4, and 6X-3) (Fig. F14). Unlithified carbonate cements are present in Sections 311-U1326C-6X-1, 8X-CC, and 311-U1326D-5X-2 (Fig. F15). A lithified carbonate is found in Section 311-U1326C-9X-2.

Biogenic components are almost absent in Unit II. There are no diatoms. Foraminifers, nannofossils, and organic fragments are rarely present on the basis of smear slide observations. Pieces of brownish wood fragments are observed in Section 311-U1326D-5X-5.

Soft-sediment deformation is observed over an interval of two cores in the upper part of Unit II (Cores 311-1326C-5X through 6X) (Fig. F16). A fault displacing silty layers in a normal sense is present at the bottom part of the zone of soft sediment deformation (interval 311-1326C-6X-5, 24–26 cm) (Fig. F17).

In Unit II, we observed soupy and mousselike textures. Soupy textures are present in Sections 311-U1326C-7X-3 and 8X-1. Mousselike textures are observed in Sections 311-U1326C-7X-3 and 311-U1326D-2X-1, 2X-4, 3X-1, and 7X-1. The Unit II/III boundary is marked by the appearance of diatoms (see **"Biostratigraphy"**), although their abundance is low and at the beginning of coring-related biscuiting.

Lithostratigraphic Unit III

Interval: Sections 311-U1326D-8X-1 through 20X-CC

Depth: 146.30–271.40 mbsf

Age: Pleistocene (>0.3 Ma)

Unit III is mainly composed of dark greenish gray (5GY 4/1) and dark gray (N4) clay, clay with diatoms, silty clay, and silty clay with diatoms. Coarser grained dark gray (N4) and very dark gray (N3) clayey silt, sandy silt, silt, sand-silt-clay, silty sand, and sand occur as minor lithologies in Unit III (Fig. F17). Fining-upward sequences are observed in Sections 311-U1326D-10X-3 and 20X-5. Drilling biscuits and other coring-related disturbance features are present throughout most of the unit.

The major nonbiogenic components of Unit III are clay minerals, quartz, feldspar, accessory minerals, opaque minerals, and biotite. Rare to moderate sulfide mottles are only present in the upper part of Unit III in Sections 311-U1326D-8X-3, 9X-2, 11X-2, 11X-4, and 20X-7. Small (<5 mm) concretions are present in Sections 311-U1326D-11X-5 and 12X-1. A dark, round, volcanic rock fragment (1.5 cm × 2 cm) is observed in Section 311-U1326D-17X-1, and an olive colored rock fragment (1 cm × 1.5 cm) is seen in Section 311-U1326D-20X-5.

The biogenic components differ from Unit II. The major lithology contains some fossils, diatoms, foraminifers, siliceous spicules, and organic debris. The most important fossils are diatoms (as much as 37% in Sample 311-1326D-20X-5, 87 cm).

Angular, partly lithified carbonates occur in intervals 311-U1326D-9X-1, 0–2 cm, 16 cm, 18–19 cm, 25 cm (Fig. F18), and 46–47 cm. XRD analysis confirms a combination of high-Mg calcite (8 mol% $MgCO_3$) and nonstoichiometric dolomite (34 mol% $MgCO_3$).

Unlithified carbonate cements are present in Sections 311-U1326-12X-5, 12X-CC, and 20X-3. A lithified carbonate nodule is present in Section 311-U1326D-16X-1.

Soupy sediment textures related to the presence of gas hydrate are present in Sections 311-U1326D-11X-2, 13X-1, and 17X-1. Mousselike sediment textures are present in Sections 311-U1326D-10X-1, 11X-2, 11X-4, 13X-1, 14X-1, 14X-3, 16X-1, 16X-3, 16X-4, 17X-1, 17X-5, 18X-2, and 18X-4 (Figs. **F19, F20**).

Environment of deposition

Site U1326 recovered a sequence that corresponds to slope basin sediments (see **"Background and objectives"**).

Lithostratigraphic Unit III is characterized by fine-grained (clay to silty clay) detrital sediments with few, thin silty/sandy interlayers from turbidites. Generally abundant, mostly marine diatoms (see **"Biostratigraphy"**) occur throughout this unit. We interpret this interval as mixed hemipelagic-turbiditic deposition. The presence of authigenic carbonate cement shows that diagenetic processes are active in Unit III.

Lithostratigraphic Unit II is characterized by fine-grained (clay to silty clay) detrital sediments with intervals of frequent silty/sandy interlayers. We interpret the coarser interlayers as turbiditic deposits, the frequent occurrence of which might indicate times of active tectonism. Below 30.4 mbsf, abundant soft-sediment deformation and dipping strata (also inferred from logging results; see evidence of layers dipping to the northeast in **"Downhole logging"**) show that tectonism is more active at this westernmost end of the transect drilled during Expedition 311. The presence of unlithified authigenic carbonate cement and a lithified carbonate shows that diagenetic processes are active in Unit II (see also **"Interstitial water geochemistry"**).

Lithostratigraphic Unit I is characterized by fine-grained (clay to silty clay) detrital sediments with thin silty/sandy interlayers from turbidites. Soft-sediment deformation observed in Section 311-U1326C-2H-5 (~10 mbsf) may be potentially related to a slump (see also **"Interstitial water geochemistry"**). Foraminifers, bivalve shell fragments, sponge spicule remains, mottling, and bioturbation, together with the high marine/nonmarine ratio of diatoms suggest hemipelagic sedimentation mixed with turbiditic inputs (coarse-grained facies). The presence of unlithified carbonate cement shows that diagenetic processes are active in Unit I.

Biostratigraphy

Cores were recovered from Holes U1326B, U1326C, and U1326D. Sample 311-U1326B-1H-CC, the only sample obtained from Hole U1326B, was barren of diatoms. Holes U1326C and U1326D contain a ~270 m thick Quaternary sedimentary sequence. The biostratigraphy determined for Site U1326 was based on an examination of all core catcher samples from the three cored holes (Table **T2**).

Diatoms

Diatoms are generally very rare to barren and poorly preserved in most of the samples from Site U1326. Only a few samples contain common to abundant and poorly to moderately preserved diatoms. Samples 311-U1326C-2H-CC (13.62 mbsf) and 3H-CC (22.13 mbsf) contain common to abundant diatom assemblages dominated by *Stephanopyxis* spp. and *Thalassionema nitzschioides* and are accompanied by rare occurrences of *Neodenticula seminae*. A large number of resting spores of *Chaetoceros* were observed in Sample 311-U1326C-3H-CC. Samples 311-U1326C-4H-CC through 10X-CC and 311-U1326D-2X-CC through 7X-CC have rare diatoms or are barren. Common to rare diatoms from Samples 311-U1326D-8X-CC through 10X-CC (150.50–172.87 mbsf) and 19X-CC (254.44 mbsf) are characterized by dominant occurrences of *Stephanopyxis* spp. and *T. nitzschioides* and rare occurrences of *N. seminae* and *Proboscia curvirostris*. Samples 311-U1326D-8X-CC and 9X-CC (150.50–160.00 mbsf) are also characterized by rare occurrences of *Thalassiosira jouseae* and abundant occurrences of resting spores of *Chaetoceros*. All samples with common to abundant diatoms are dominated by marine diatoms (>90%), but some samples with rare diatoms (Samples 311-U1326C-1H-CC and 5H-CC and 311-U1326D-13X-CC) are dominated by nonmarine diatoms.

The interval between the shallowest sample and Sample 311-U1326C-3H-CC (3.88–22.13 mbsf) contains *N. seminae* but lacks *P. curvirostris* and is assigned to North Pacific Diatom (NPD) Zone 12 (*N. seminae* Zone; 0–0.3 Ma). A diatom zonal assignment is not possible for the interval between Samples 311-U1326C-4H-CC and 10X-CC or from 311-U1326D-2X-CC through 7X-CC (28.27–141.65 mbsf) because these intervals contain no diatoms or zonal marker species. The last occurrence (LO) of *P. curvirostris* was recognized in Sample 311-U1326D-8X-CC (150.50 mbsf), marking the NPD Zone 12/11 boundary (*P. curvirostris* Zone). The interval between the LO of *P. curvirostris* and Sample 311-U1326D-19X-CC (150.50–254.44 mbsf) contains *P. curvirostris* but

lacks *Actinocyclus oculatus* and was assigned to NPD Zone 11 (*P. curvirostris* Zone; 0.3–1.0 Ma). Sample 311-U1326D-20X-CC (270.69 mbsf) cannot be assigned to a diatom zone because it is barren. The NPD Zone 12/11 boundary is likely within the above mentioned barren interval (28.27–141.65 mbsf), but its exact depth determination requires postcruise analysis of additional samples at more closely spaced intervals.

Interstitial water geochemistry

The main objectives at this site were to document the evolution of the interstitial water (IW) chemistry and the distribution of gas hydrate at the westernmost uplifted ridge of the Cascadia accretionary prism.

A total of 75 IW samples were processed from two holes cored at Site U1326. In Hole U1326C, 27 whole-round samples, 10–40 cm in length, were retrieved at the catwalk. The sampling frequency was two per section in the uppermost 10 m (Sections 311-U1326C-1H-1 through 2H-4), followed by one to three samples per core to TD of the hole. The sediment collected from Core 311-U1326C-5X, the first XCB core, was too disturbed and unsuitable for IW extraction. Two samples contained gas hydrate (Samples 311-U1326C-6X, 83–96 cm, and 7X-3, 74–101 cm). Based on lithology, infrared (IR) camera images, and visual core observations, these samples were split into five subsamples, thus three extra samples were processed. In addition, two samples from pressure Core 311-U1326C-12P were collected, generating a total of 30 IW samples from this hole.

In Hole U1326D, 37 IW samples were collected at a sampling frequency of one to two per core depending on recovery. Most whole-round IW samples were 10–50 cm in length, except for the deepest cores, from which we collected 100 cm long samples in an effort to obtain sufficient volumes of interstitial fluid. Because of the weather conditions and severe ship heave, the recovered sediment was highly disturbed and only a few clean sediment "biscuits" were retrieved from these long whole-round samples. Six of the samples were divided based on IR imaging and lithology (as described below), yielding eight additional samples for processing for a total of 45 IW samples from this hole.

In an effort to characterize the IW chemistry associated with gas hydrate–bearing sediment and to compare it with sediment with an IW composition more typical of background conditions, whole-round samples were chosen from intervals with the highest IR temperature anomalies and from zones with less anomalous thermal signals within the zone of gas hydrate occurrence. Three samples from Hole U1326C and eight samples from Hole U1326D were collected to evaluate the chlorinity of the IW associated with intervals where gas hydrate presence was inferred from IR anomalies. These samples were imaged again with a handheld IR camera, photographed, and described prior to the squeezing process, documenting the association of gas hydrate mostly with sand horizons, as previously observed at Sites U1325 and U1328. Sand and clay lithologies were split and squeezed separately.

The IW data collected at Site U1326 are listed in Table **T3.** Because of the lithified nature of the formation, XCB coring was used for the collection of a large portion of IW samples. Because XCB coring yields relatively more disturbed cores, these cores are more likely to be contaminated with the drilling fluid than APC cores. Sulfate concentration below the depth of the sulfate/methane interface (SMI) was used to identify and quantify contamination by the drilling fluid, and the sulfate-corrected data are listed in Table **T4.** The sulfate-corrected data for Holes U1326C and U1326D are illustrated in Figures **F21, F22, F23,** and **F24.**

Salinity and chlorinity

The salinity and chlorinity profiles at this site point to a deeper fluid with a chloride concentration higher than seawater (>585 mM; Fig. **F21**), indicative of low-temperature diagenetic reactions in the deeper parts of the site. As suggested for Site U1325, a plausible candidate for such a reaction is the alteration of volcanic ash to clay minerals and/or zeolites. These reactions consume H_2O and, therefore, increase the in situ chlorinity values.

In the zone extending from ~45 to 270 mbsf (the seismically inferred BSR is at ~230 mbsf), salinity and chlorinity data show discrete excursions to fresher values, indicating that gas hydrate was present in the cores and dissociated prior to processing the samples, consistent with observations of distinct negative thermal excursions in IR scans (see **"Physical properties"**). Indeed, the lower salinity and chlorinity points shown in Figure **F21** represent samples collected to specifically target the more pronounced IR temperature anomalies. Similar to Sites U1325 and U1328, our observations at this site indicate that gas hydrate predominantly occupies the sandy layers. The minimum salinity and chlorinity values recorded are 4.6 and 90.1 mM (13.5% and 16% of seawater value, respectively) and were measured in a gas hydrate–bearing, 6 cm thick coarse-sand layer recovered in Sample 311-U1326C-6X-4, 83–96 cm. This sample, retrieved from 44.9 mbsf, also represents the first IR temperature anomaly in Hole U1326C. At

53.4 mbsf, Sample 311-U1326C-7X-3, 74–101 cm, contained small amounts of gas hydrate. Beneath these intense chlorinity and IR anomalies, there is little indication of gas hydrate presence until ~83.8 mbsf, below which multiple chlorinity excursions, with values as much as 39% fresher than seawater, were recorded in various sand-bearing intervals.

The degree of dilution of the IW by gas hydrate dissociation shows an approximate linear decrease with depth, from ~48 mbsf, where the lowest chlorinity and salinity values are observed, to ~220 mbsf (Fig. F21). This zone overlaps with the highest gas hydrate concentrations inferred from a zone of high resistivity in the LWD records, which lies between ~70 and 100 mbsf (see "Downhole logging"). This trend in the gas hydrate distribution suggests that a fault or a steeply dipping sand layer supplies methane to sediment at shallower depths. This is supported by the distinct molecular composition of the gas hydrate at the cemented, coarse sand at 44.9 mbsf and by the observation of a normal fault in the sediment (see "Organic geochemistry" and "Lithostratigraphy;" Fig. F15). The fluid that transports the methane to this layer also has elevated ethane, as indicated in the gas data (see "Organic geochemistry"). There are three additional interesting observations in Figure F21:

1. In the ~20 m above the seismically inferred BSR, no IR cold anomalies were observed, and the Cl concentration values are equal or close to the background value.
2. Low chlorinity values associated with IR cold anomalies are observed below the seismically inferred depth of the BSR, at the approximate depth of the base of the gas hydrate stability zone (GHSZ), which is at 275 ± 25 mbsf based on a geothermal gradient of ~60°C/km (see "Physical properties").
3. The lack of chlorinity and IR anomalies at 215–225 mbsf reveals the absence of gas hydrate, the reason for which is as yet unclear.

Biogeochemical processes

Intense microbial activity at Site U1326 results in sulfate depletion, phosphate and alkalinity production, and significant Ca and Mg depletion in the IW of the uppermost ~3 m (Figs. F22, F23). Linear interpolation of sulfate concentration versus depth places the SMI at ~2.5 mbsf; however, we noted a hydrogen sulfide smell to a depth of ~10 mbsf while cleaning the whole-round samples. Unexpectedly, Sample 311-U1326C-2H-1, 60–75 cm (4.6 mbsf), yielded a sulfate concentration of 7.6 mM. The appearance of sulfate below the SMI depth could be caused by rapid sediment redeposition (i.e., a slump) or by contamination with drill water during the drilling process. Based on only the shipboard data, it is impossible to distinguish between the two theories.

A first maximum in the Mg/Ca ratio is observed in the interval from just below the depth of the SMI at 3.7 mbsf (Fig. F23) to 9.8 mbsf. In this zone, alkalinity and ammonium concentrations also increase. Alkalinity reaches its first maximum of 23.1 mM at 2.9 mbsf and has a second peak of 19.7 mM at 9.8 mbsf (Fig. F22). This uppermost zone of carbonate precipitation is dominated by the preferential loss of Ca relative to Mg. The Ca concentration falls to ~33% of the original seawater value, but the Mg/Ca molar ratio increases to about twice that of seawater.

A second zone of intense carbonate diagenesis is indicated by large minima in the Mg/Ca ratio and alkalinity, and a minor minimum in ammonium concentration at ~70 mbsf, which corresponds to the depth of a sharp Ca maximum to almost twice seawater value (Fig. F23). These distributions are indicative of dolomitization of the calcite that precipitated in the upper zone of carbonate diagenesis. The Mg involved in the dolomitization reaction has a mixed origin. Some of the Mg is supplied by the original IW and some was expelled from clay ion exchange sites by the high ammonium concentrations, as suggested by the presence of an ammonium minimum between 40 and 100 mbsf.

A third zone of carbonate diagenesis occurs at ~115 mbsf, where Ca concentrations show a second intense minimum to ~32% seawater value. Carbonate precipitation is driven by the high alkalinity and calcium concentration almost twice that of seawater at ~70 mbsf. At such a high Ca concentration, coupled with the high alkalinity and a very low Mg/Ca ratio of 1.1, dolomite cannot form and authigenic calcite precipitates instead.

Sr concentration does not play an important role in the above described carbonate formation and recrystallization zones of the uppermost ~130 m because the various diagenetic carbonates that form or recrystallize have similar Sr concentrations at the prevailing low temperatures.

The decline in the Mg/Ca ratio and increase in Ca concentrations below ~130 mbsf are primarily caused by interaction with the deeper fluid, which is forming by alteration of volcanic ash into a Mg-rich clay and zeolites, as suggested by the K and Sr depth profiles (Figs. F21, F23).

Inorganic diagenetic processes

Two zones of high silica concentrations (lithostratigraphic Units I and III; see "Lithostratigraphy") and a zone of low silica concentrations (Unit II; see

"Lithostratigraphy") are observed (Fig. F24). These zones reflect the depth distribution of diatoms at this site (see "Biostratigraphy").

Lithium shows an interesting concentration depth profile (Fig. F24). Li is depleted in the uppermost 7 m and remains low to ~150 mbsf, suggesting that some volcanic ash is interspersed in the sediment throughout this depth interval. At the depth where the ammonium concentration reaches the 8.1 mM maximum (157 mbsf), Li is expelled from the clays by ion exchange reactions. Both Mg and Li are released from clay ion exchange sites, but the Mg binding energy in the clay ion exchange sites is considerably lower than that of Li, explaining the observed stepwise behavior. Li has slightly higher concentrations relative to seawater below the BSR, and therefore is in the deep fluid.

Diagenetic deep fluid

As indicated in Figures F21, F22, and F24, the deep fluid has higher than seawater chlorinity values, is enriched in Ca and Sr, and is depleted in Mg, K, and B. These distributions are consistent with low-temperature volcanic ash alteration reactions that form Mg and K clay minerals and K-zeolites. As observed at Site U1325, the original IW is evolving with depth into a Ca-Cl brine. Extrapolating the slopes of the Mg and Ca concentration versus depth profiles suggests that Mg should reach zero concentration at 600–700 mbsf, which is ~200 m deeper than at Site U1325, and at this depth Ca concentration will be about three times that of seawater.

Organic geochemistry

The shipboard organic geochemistry program for Site U1326 included analysis of the composition of volatile hydrocarbons (C_1–C_5) and nonhydrocarbon gases (i.e., O_2 and N_2) from headspace (HS) gas samples, void gas samples, gas samples recovered during PCS degassing experiments, and dissociated gas hydrate. Sediment from the IW squeezecakes was analyzed for inorganic carbon (IC) content (also expressed as weight percent $CaCO_3$), total carbon (TC), and total nitrogen (TN). Total organic carbon (TOC) was calculated as the difference between the TC and IC. A total of 70 samples for HS and solid-state analysis were collected at Site U1326. Most of the HS samples were collected on the cut end of core sections facing the IW samples so that the gas and IW data could be integrated. The near-surface sediments from Core 311-U1326C-1H were sampled at high depth resolution to define the SMI. Six pairs of HS samples were collected from inside and outside each IR anomaly interval and were imaged with the IR camera to confirm that the samples contained sediment from the cold section of the core.

We collected 44 void gas samples at Site U1326 from depths where gas cracks in the sediment were first observed (6.1 mbsf) to a TD of 269.1 mbsf. A gas sample was also collected from a PCS degassing experiment conducted with Core 311-U1326C-12P (see "Pressure coring").

The primary objectives of the organic geochemistry sampling program at this uplift site were to

- Determine the origin (microbial vs. thermogenic) of the gases recovered by HS gas, void gas, and PCS degassing techniques;
- Investigate the relationship between the gas composition and the distribution of gas hydrate in the system; and
- Describe the carbon and nitrogen contents of the sediments.

Hydrocarbons

Headspace gas and void gas compositions

Hydrocarbon HS gas measurements from Holes U1326C and U1326D are listed in Table T5 and plotted relative to depth in Figure F25. Results are reported in parts per million by volume (ppmv) of methane, ethane, ethylene, and propane in the air headspace of a 25.41 ± 0.18 mL serum vial and as the millimolar concentration of dissolved methane in the IW (see "Organic geochemistry" in the "Methods" chapter). Methane content increased rapidly from 37 ppmv in the near-surface sample (0.8 mbsf) to ~17,000 ppmv at 6.2 mbsf. There was a general trend toward lower HS methane content with depth below ~10 mbsf. In the deeper sections of Holes U1326C and U1326D, the methane HS concentration generally varied between ~2000 and 5000 ppmv. Values above that range were usually associated with samples targeting IR anomalies. Low concentrations of ethane (<2.0 ppmv) were occasionally observed, whereas ethylene and propane were detected in two samples. A few air samples collected from the catwalk area during Site U1326 operations had an average concentration of 2.45 ± 0.39 ppmv (n = 3) methane, which is slightly higher than the current atmospheric methane concentration (~1.7 ppmv). The data reported in Table T5 are uncorrected for the atmospheric contribution.

The composition of gas from voids in the core liner is shown in Table T6 and displayed relative to depth (excluding methane) in Figure F26. With the exception of several samples that contained a large percentage of air, the void gas was almost entirely methane. Carbon dioxide concentrations ranged between

0.0% and ~0.4%, and hydrogen sulfide was absent in all samples.

Although the ΣC_{2+} hydrocarbon void gas concentrations were <125 ppmv for all samples, their relative abundance and distribution were valuable for describing the gas hydrate system at Site U1326. Ethane was the most abundant C_{2+} hydrocarbon in the void gas. Low concentration (<25 ppmv) in the uppermost 35.3 m was underlain by an interval extending to 72 mbsf with 44–82 ppmv ethane. In this same interval, two gas hydrate samples were collected, significant pore water freshening (see **"Interstitial water geochemistry"**) was observed, and IR temperature anomalies (see **"Physical properties"**) were imaged. Ethane and methane (the only void gases present in that interval) support Structure I gas hydrate formation (Sloan, 1998). The shallow sediments, therefore, most likely contained Structure I gas hydrate.

With greater depth, ethane concentration returned to the near-surface concentration before increasing again. Increasing ethane concentration was accompanied by increasing propane concentration. Maximum concentrations of ethane (122 ppmv at 244 mbsf) and propane (56 ppmv at 217 mbsf) occurred near the depth of the seismically inferred BSR (~234 ± 2.5 mbsf). Isobutane concentration was elevated within the same interval, with a maximum of ~10 ppmv at 228 mbsf. Propane and *i*-C_4 are known Structure II gas hydrate formers (Sloan, 1998). Therefore, enrichment of propane and *i*-C_4 in the void gas is an indication of decomposed Structure II gas hydrate.

There was a marked decrease in the C_1/C_2 ratio in the 44–72 mbsf interval where the near-surface gas hydrate was collected. Within that interval, C_1/C_2 ratios from void, gas hydrate, and PCS gases were virtually identical (Tables **T6, T7**).

The C_1/C_2 ratio returned to near-surface values below the shallow gas hydrate zone and then decreased gradually with depth to ~180 mbsf. The variation of the *i*-C_4/*n*-C_4 ratio in the deeper cores was, however, more distinct and informative than the C_1/C_2 ratio. Whereas *i*-C_4 is sequestered by Structure II gas hydrate, *n*-C_4 is not. Consequently, elevated *i*-C_4/*n*-C_4 ratio indicates decomposition of Structure II gas hydrate. The *i*-C_4/*n*-C_4 ratio from 132 mbsf to the base of Hole U1326D was elevated. The maximum value of *i*-C_4/*n*-C_4 (~19) occurred at 198.6 mbsf and is a strong indication that Structure II gas hydrate was present at that depth (Fig. **F27**).

Evidence of different molecular ratios associated with gas hydrate at different depths at the same location suggests that the local gas hydrate system may be supported by different gas-bearing source fluids or that the hydrocarbon composition of the fluids was altered during fluid migration from depth. An association between a steeply dipping sand layer at ~45 mbsf and concentrated gas hydrate in the shallow horizon indicates fluid migration along structural fractures (see **"Interstitial water geochemistry"**).

Gas composition expressed as the C_1/C_2 ratio of HS and void gas is plotted relative to sediment temperature in Figure **F28.** Sediment temperature is based on the calculated geothermal gradient of 60°C/km (see **"Physical properties"**). The monitoring of the C_1/C_2 ratio in void and HS gas samples and its relationship to temperature was developed as a safety guideline by the Joint Oceanographic Institutions for Deep Earth Sampling (JOIDES) Pollution Prevention and Safety Panel during the Ocean Drilling Program. C_1/C_2 ratios are described as either "normal" or "anomalous" depending upon where they plot relative to the slightly diagonal line in Figure **F28.** All values measured at Site U1326 were within the acceptable "normal" limits for safe drilling (Pimmel and Claypool, 2001).

Biogeochemical processes

The IW and HS gases from Cores 311-U1326C-1H and 2H were sampled at high depth resolution (approximately two samples per 1.5 m section) to define the SMI. The depth of sulfate depletion was 2.9 mbsf, but a deeper "peak" was measured at 4.6 mbsf (Fig. **F29**). It was suggested that this second peak may be related to a slump feature or drilling fluid contamination (see **"Interstitial water geochemistry"**). The increasing concentration of methane to 6.2 mbsf is not necessarily consistent with the former interpretation because consumption of methane would be expected at the "second" SMI. The shallow and thin SMI is located between ~2.3 and 3 mbsf.

Sediment carbon and nitrogen composition

The sediment IC, carbonate ($CaCO_3$), TC, TOC, and TN concentrations and C/N ratio from Site U1326 are listed in Table **T8** and plotted relative to depth in Figure **F30.** High-resolution depth profiles were obtained for the uppermost 13 m. No data were obtained below 198 mbsf because the ship was under way in rough seas by the time the samples from that interval were freeze dried. The solid-state carbon and nitrogen vertical profiles displayed transitions that agree remarkably well with the defined lithostratigraphic units (see **"Lithostratigraphy"**). The carbonate content is relatively high (average = 0.73 wt%) in the depth interval corresponding to lithostratigraphic Unit I (0–24.1 mbsf), low in Unit II (24.1–

146.3 mbsf; average = 0.19 wt%), and intermediate in Unit III (146.3–271.4 mbsf; average = 0.41 wt%). The highest value was measured at 2.15 mbsf, which is the depth roughly corresponding with the SMI. TOC displays a similar distribution with average contents of 0.51, 0.34, and 0.45 wt% in lithostratigraphic Units I, II, and III, respectively. C/N ratios in lithostratigraphic Unit I are ~11.1, which indicates the highest terrestrial contribution of organic matter among all sites investigated during Expedition 311. This conclusion is interesting considering Site U1326 is the greatest distance from land. C/N ratios in lithostratigraphic Units II (average = ~8) and III (average = ~7.7) are similar, though a low C/N value of 2.1 at 131 mbsf skewed the average value for lithostratigraphic Unit II downward.

Microbiology

Site U1326 is located along the transect of sites established during Expedition 311 across the northern Cascadia accretionary prism at the westernmost uplifted ridge of the accretionary prism. It was the last site sampled for microbiology. Efforts continued to obtain live anaerobic methane oxidizers, potentially unknown gas hydrate–associated microbial communities, high pressure adapted microorganisms, and methanogens. Subsampling for direct cell counts and biological contamination tests continued at this site.

Microbiological sampling

Sampling from the mudline (Sample 311-U1326C-1H-1, 0–3 cm) in Hole U1326C and the deepest core (Sample 311-U1326D-20X-1, 70–80 cm; 263 mbsf) in Hole U1326D targeted microorganisms for aerobic and anaerobic high-pressure culturing.

Methanogenesis can occur in most anaerobic environments, but it becomes the major metabolic strategy when other electron donors such as nitrate, Fe(III), and sulfate are depleted. We sampled regularly downhole to below the depth of the predicted BSR to quantify methanogenesis in these sediments (see **"Microbiology"** in the "Methods" chapter).

Contamination tests

Contamination tests at previous sites had verified that the interior of APC cores and the center of biscuits in XCB cores yielded samples with low amounts of exogenous microbial contamination. At this site we focused contamination tests on sand layers, gas hydrate–bearing sediments, and shallow APC cores where soupy texture is common.

Perfluorocarbon tracers

Samples for perfluorocarbon tracers and fluorescent microsphere analyses were taken immediately from the ends of APC whole-round cut sections on the catwalk. Extra sediment samples for microsphere analysis were collected from split cores in the core laboratory because it was possible to differentiate between sand layers, biscuits, and drilling slurry. Sediment samples associated with gas hydrate were collected from the ends of whole-round sections when the presence of gas hydrate was indicated by the data collected on the catwalk using the IR camera. Samples were analyzed as described and the raw data are presented in Table **T9.**

Fluorescent microspheres

We detected very small but nonzero numbers of fluorescent microspheres in the interior of the mudline APC core, which was very soupy at this site. Tests on sand layers, which were widely distributed at this site, showed that the interiors of sand layers were possibly contaminated with microspheres but at a very low level. One of the gas hydrate–bearing samples indicated that the interior of the sediment was contaminated with the microspheres at a very low level.

Shipboard analysis

Samples were taken from the top (Sample 311-U1326C-1H-1, 0–3 cm) and bottom (Sample 311-U1326D-20X-1, 70–80 cm; 263 mbsf) of the sedimentary section for inoculation of enrichment cultures targeting high-pressure adapted heterotrophic and sulfate-reducing microorganisms. Samples were maintained at low temperature, and dilution series were inoculated to culture for microorganisms at 55.1 MPa and 4°C. Cultures for sulfate reducers required preparation in the anaerobic chamber and were fed formate, acetate, or lactate as a carbon source.

Physical properties

Site U1326 is located at the crest of the westernmost accretionary ridge on the Expedition 311 transect across the northern Cascadia margin accretionary complex. A major objective of this site was to determine the physical properties and gas hydrate distribution in this distal accretionary ridge.

Physical properties were measured in cores recovered from Holes U1326B, U1326C, and U1326D. Hole U1326C extended to 86.7 mbsf, where it was abandoned for technical reasons. Coring in Hole U1326D began at 78.8 mbsf and continued to 271.4 mbsf.

Figure F31 presents an overview of the physical property data obtained from these two holes. All cores from this site were systematically scanned upon arrival on the catwalk to detect IR anomalies indicative of gas hydrate dissociation during core recovery. Cold temperature anomalies were observed at a wide range of depths from 40 to 250 mbsf, and catwalk sampling was conducted based on these IR scans. Numerous IW samples were taken based on the IR images to extend the chlorinity anomaly database and to calibrate IR data as a proxy for in situ gas hydrate concentration. Two sections with thick sandy and silty zones and high gas hydrate saturation were examined in more detail. In the following sections we discuss these data and compare them to data acquired at other sites.

Infrared images

All cores were scanned on the catwalk following the track-mounted IR camera procedures described in "Physical properties" in the "Methods" chapter. Portable Document Format images of the scans of all cores are available in the "Site U1326 core descriptions." Temperature arrays in the format of comma-separated value files were exported from the IR camera software and then concatenated for each core. The arrays were then further concatenated for all cores available in a given hole. Figure F32 shows cold thermal anomalies in the concatenated false-color IR images for Holes U1326C and U1326D. This figure also shows the Hole U1326A LWD resistivity data and the pore water saturation derived from these data for comparison.

As a precursor to quantitative studies of the temperature anomalies, downhole temperatures were averaged for each pixel row in the IR temperature array, excluding pixels ~1 cm from the edge of the image and 2 cm along the midline of the image to eliminate the major thermal artifacts in the images. On first look, a striking aspect of Hole U1326D is that it is consistently colder below ~150 mbsf (Fig. F33A). Comparison of the temperature profile with the ambient temperature on the catwalk indicates that this change in core liner temperature is closely correlated with a rapid change in ambient air temperature. The IR camera measures the temperature of the surface of the core liner, which is a function of the gradient between the air temperature outside the liner and the temperature of the core. In Figure F32, the cold core liner temperature makes it more difficult to see that the entire interval from 40 mbsf to the base of Hole U1326D contains many distinct cold anomalies. The ΔTs of these cold anomalies are not affected by changes in ambient temperature because the background temperature and the cold temperature excursions are affected equally. Figure F34 shows the ambient temperature and light intensity on the catwalk for the entire expedition and the acquisition times of individual cores. During the first 9 days of the cruise, when LWD data were acquired, light intensity and temperature show strong diurnal variations. During coring, skies were overcast and openings in the catwalk wall were shielded; consequently, ambient temperatures varied in a relatively small range except for cold periods on 2 October and 25 October 2005.

Many of the IR anomalies were used to identify samples for IW chemical studies. Sample 311-U1326C-6X-4, 83–96 cm, is shown in Figure F35. This sample contained pore-filling gas hydrate in a 4–5 cm thick, medium- to coarse-grained sand layer. The gas hydrate appeared to be filling pores in the sand. Upon physical dissection, it was clear that the central part of the sand layer contained more gas hydrate than sediment, suggesting both pore-filling and grain-supporting gas hydrate in this sample. The IR image and temperature profile in Figure F35 show that the temperature of the gas hydrate at the time of core processing was as low as –2.4°C. The chlorinity anomaly corresponding to this IR anomaly was 197.7 mM, which represents very strong pore water freshening (see Table T3). A moisture and density (MAD) sample was taken from the sand layer containing the gas hydrate. This sample was notable for its relatively coarse grain size and the occurrence of buff-colored fine silt or clay coating on the sand grains after drying. MAD results were as follows: bulk density = 2.21 g/cm^3, grain density = 2.84 g/cm^3, and porosity = 34.7%. The porosity value is among the lowest measured and is consistent with the relatively coarse grain size of the sample.

Another notable gas hydrate occurrence was at 246 mbsf in Hole U1326D. The lower part of Core 311-U1326D-18X was characterized by an unusually thick cold anomaly (Fig. F33B, F33C). The upper part of this anomaly was processed by the inorganic geochemists and the lower part (Section 311-U1326-18X-4) was opened immediately after sectioning on the catwalk. The sediment in this core (Fig. F33D) had a very unusual texture. It remained cohesive and was "foamy" rather than being soupy or mousselike (i.e., it felt like foam rubber to the touch). Sediment in this section lost its foamy texture in <1 h, collapsing to a stiff, dry sediment that occupied ~25% of the original volume in the core liner. Additional analyses will be performed postcruise to better understand the reasons for and implications of this unusual sediment character.

Sediment density and porosity

Gamma ray attenuation (GRA) densities were measured on the multisensor track (MST) and bulk density, grain density, and porosity were calculated from the measured wet and dry weights and dry volume of the sediments (MAD measurements; Table T10). Both estimates of density were compared to in situ densities measured by the LWD/MWD tools (Fig. F31). Significant differences are seen between MAD and LWD porosities in the uppermost 25 m of Hole U1326C, indicating significant lateral heterogeneity over the ~25 m between Holes U1326A and U1326C or, more likely, problems with the LWD data at these shallow depths. MAD porosities of 53% ± 5% in the uppermost 20 m are unusually low for near-seafloor sediments. The data, however, are consistent with relatively high shear strengths and with unusually high *P*-wave velocities recorded both on the Hamilton frame and by wireline logging. A possible explanation for the difference in shallow sediment characteristics between holes at this site is the presence of a fault between the holes, consistent with the seismic data and uplifted nature of Site U1326. Mass wasting that reveals previously buried and overconsolidated sediments may also be a factor at this site.

Magnetic susceptibility

Magnetic susceptibility at this site was generally high and variable, except in the uppermost 10 m (Fig. F31). Causes for the variability in magnetic susceptibility will be a topic for postcruise research. It is likely related to variable input of silty and sandy turbidites, reflecting different sedimentary environments.

Compressional wave velocity from the multisensor track and Hamilton frame

P-wave velocities were measured using both the MST and the Hamilton frame on a limited number of sections from the top of Hole U1326C (Table T11). Velocity measurements ranged from 1480 to 1580 m/s. Velocities at Site U1326 are much higher in the shallow subsurface than at other sites (Fig. F36). This correlates well with the shear strength data and may be related either to a high carbonate content in the sediments or to mass wasting, which would have exposed previously buried sediments at the seafloor.

Shear strength

Shear strength measurements were made in Holes U1326C and U1326D using both the automated vane shear (AVS) system and the handheld Torvane (Tables T12, T13). Measurements were made on the working half of the split core after resistivity, velocity, and MAD samples had been taken. Efforts were made to take measurements in areas of the core where the sediment was undisturbed by gas expansion and drilling cracks. Measurements were also taken as close as possible to where MAD samples had been extracted. At the top of Hole U1326C, at least two Torvane measurements and one AVS measurement were taken per section. The number of measurements decreased deeper in the hole because of increased disturbance in the cores.

Shear strength generally increases with depth (see Fig. F31 for all shear measurements and Fig. F37A for measurements from 0 to 120 mbsf). Shear strength ranges from 5 kPa in sands to 300 kPa in clay. Shear strengths are unusually high in the shallow subsurface (Fig. F37A). The ratio of shear strength to overburden pressure (Fig. F37B) is a measure of the consolidation state of the sediments. A ratio >0.25 indicates that the sediments are overconsolidated for their depth below the seafloor. Overconsolidation can be seen in the uppermost 20 m of Hole U1326C (Fig. F37C). This correlates well to the high *P*-wave velocity and may be caused by high carbonate content in the shallow sediments or to mass wasting, which has been documented nearby and would have exposed previously buried sediments at the seafloor.

Electrical resistivity

Electrical resistivity was measured in Holes U1326B, U1326C, and U1326D using both the contact and noncontact methods. Measurement interval using the contact system varied depending on the quality of the core. Measurements taken with the noncontact method were made every 2.5 cm. Gas expansion of the core caused the results to be very scattered. The high degree of scatter may also be caused by the large amount of sand at this site.

Resistivity values ranged from 0.3 to 2.5 Ωm (Table T14; Fig. F38A). The higher value obtained at ~45 mbsf was attributed to cracks in the sediment. The formation factor was calculated for the contact resistivity measurements assuming a pore water salinity of 3.4% (Fig. F38B). Pore water resistivities were calculated from the IW salinities using equations developed by Fofonoff (1985) and corrected to 20°C (Fig. F38A). Archie's parameters were then determined by fitting Archie's equation to the formation factor and MAD porosities (Fig. F38D). Because of the wide range of resistivity and the large number of sand layers within the cores, two sets of parameters were determined: one for porosities >0.45 and the other for porosities <0.45. For porosities >0.45, the cementation coefficient m = 1.38 and the tortuosity coefficient a = 1.78. For porosities <0.45, m = 1.64 and a = 1.11. For comparison with the MAD porosi-

ties, porosities were calculated from the formation factor using the first set of parameters. (Fig. F38C).

Thermal conductivity

Thermal conductivity values were less scattered at this site than at other sites (Table T15; Fig. F31). Examination of split cores in the intervals in which the measurements were taken suggests that thermal conductivities <0.9 W/(m·K) are associated with core disturbance caused by gas expansion. Thermal conductivities of 0.9–1.1 W/(m·K) appear to generally be related to clay-rich intervals, whereas thermal conductivities >1.1 W/(m·K) appear to be related to coarser grained intervals. This relationship will be examined more carefully postcruise. For determination of in situ temperature and heat flow, a constant thermal conductivity value of 1.1 W/(m·K) was assumed.

In situ temperature profile

Four deployments of temperature tools were attempted at Site U1326 (Table T16). A third-generation advanced piston corer temperature (APCT-3) tool deployment on Core 311-U1326C-4H at 30.4 mbsf provided very good quality data (Fig. F39), although the initial frictional pulse was unusually high. The extrapolated temperature at this depth of 4.30°C is similar to the temperature of 4.44°C obtained at 33 mbsf at Site U1325. Unfortunately, the transition to XCB coring occurred immediately after this core, so that no more APCT-3 measurements were possible at this site.

Given the high ship heave, a worsening weather forecast, and limited time available at this last site, the decision was made to only attempt DVTP measurements near the expected base of the GHSZ. Three attempts were made at depths of 252, 271.4, and 300 mbsf. For the last two attempts, mud was pumped into the borehole in an attempt to damp the effect of heave. All three attempts briefly penetrated the seafloor but did not remain coupled to the sediment long enough to estimate in situ temperature by modeling the decay of the frictional pulse generated by probe insertion. Instead, the data show a gradual increase in temperature that appears to approach temperatures in the range of 16°–19°C. Because of questions about the depth to the base of the GHSZ at this site, postcruise work will include an attempt to estimate the in situ temperature by modeling heating of the borehole by the surrounding rock.

Figure F40 shows a compilation of all in situ temperature estimates from Expedition 311 compared to results from Site 889. The implied heat flow, assuming a constant thermal conductivity of 1.1 W/(m·K), is also shown and compared to the regional heat flow determined by Hyndman and Wang (1993). Temperatures at Site U1329 are clearly higher at a given depth. Heat flow across the lower slope (Sites U1325, U1327, and U1328) appears to be depressed compared to the regional heat flow pattern, consistent with perturbation by a high sedimentation rate and upward fluid advection (Hyndman and Davis, 1992). Postcruise analysis will focus on detailed examination of data uncertainties and on the processes that can explain intersite and intrasite variation.

Paleomagnetism

Note: This section was contributed by Jennifer Henderson and Katerina Petronotis (Integrated Ocean Drilling Program, Texas A&M University, 1000 Discovery Drive, College Station TX 77845, USA).

Alternating-field (AF) demagnetization of the sedimentary archive-half sections was used to determine the remanent magnetization components recorded in the recovered core (Fig. F41). The paleomagnetic data will be used postcruise to characterize the magnetic properties of the sediments and to construct a magnetostratigraphy of the sedimentary section recovered at Site U1326. The AF demagnetization applied at 10 and 20 mT should have removed most of the drill string magnetic overprint, but postcruise demagnetization at higher fields will most likely be required.

Questionable data may be associated with remanence measurements over intervals disturbed or deformed by coring. Similarly, magnetic edge effects, which can be large when measurements are within ~5 cm of the edge of a section or void, can give biased results. To avoid interpreting results in these regions, we manually noted the disturbed intervals and voids in the cores. Data from these intervals will be removed prior to postcruise interpretation.

Pressure coring

The main objectives of pressure coring during Expedition 311 were to quantify natural gas composition and concentration in sediments and to determine the nature and distribution of gas hydrate and free gas within the sediment matrix. To achieve these objectives, we

- Measured the quantity and composition of gases released during controlled degassing experiments,
- Conducted nondestructive measurements (X-ray imaging, *P*-wave velocity, gamma ray density) at in situ pressure and during degassing, and

- Preserved hydrate-bearing sediments at in situ pressure for more comprehensive shore-based investigations.

Nondestructive measurements not only provide a direct indication of the existence of gas hydrate, but the resulting data (acoustic impedance) can be used to help interpret regional seismic data. Site U1326, situated on the first uplifted ridge, had a strong BSR. The LWD/MWD data from Hole U1326A displayed the highest resistivity values seen during Expedition 311, with gas hydrate saturations calculated from Archie's equation as high as 60% (see **"Gas hydrate and free gas occurrence"**). There were also high resistivities below the estimated depth of the BSR (234 mbsf), potentially indicating free gas (see **"Gas hydrate and free gas occurrence"**). Specific objectives at Site U1326 were to confirm and quantify the presence of gas hydrate above the BSR, targeting the very high resistivity layer near 90 mbsf, and free gas below the BSR.

Operation of pressure coring systems

Pressure coring tools were deployed only three times at Site U1326 (Table **T17**): one FPC core (Core 311-U1326C-11Y), one PCS core (Core 311-U1326C-12P), and one HRC core (Core 311-U1326C-13E). The pressure coring tools were deployed in succession in a narrow interval between 82.7 and 86.7 mbsf, where the Hole U1326A LWD data had shown very high resistivity values. Figure **F42** shows the pressure history of the cores during deployment, coring, recovery, and chilling in the ice shuck. Figure **F43** displays the same data plotted as a pressure/temperature trajectory, showing the stark contrast between a deployment where the core remains clearly inside the gas hydrate stability field (Core 311-U1326C-11Y) and one that ends up in the laboratory well outside the gas hydrate stability field (Core 311-U1326C-12P).

The FPC deployment that recovered Core 311-U1326C-11Y was unexceptional until the sand line tension, when lifting the bit from the BHA exceeded the expected load by 2 tons. It was later concluded that a significant amount of sand had entered the BHA and had hindered the recovery. Scouring the outer barrel of the FPC also indicated clean sand had been penetrated. The autoclave was retrieved under nearly full pressure (17.5 MPa, compared with an in situ pressure of 19.2 MPa). X-ray images showed that this core was very short (15 cm) and situated in the center of the core barrel, implying that the core below it had washed out of the core liner. The liner and recovered portion of Core 311-U1326C-11Y were transferred from the autoclave, analyzed in the Pressure Multisensor Core Logger (MSCL-P; see **"Measurements on HYACINTH cores"**), and transferred to a storage chamber for further shore-based studies.

The PCS deployment (Core 311-U1326C-12P) recovered a partial core at 3.4 MPa. While the core was in the X-ray system, we observed a gas bubble trapped in the inner core barrel. After degassing was completed, the short core was extruded and some very coarse sand and rocky material was found in the outer core barrel.

During the final deployment with the HRC (Core 311-U1326C-13E), the lower part of the autoclave and bit assembly were lost, ending operations in Hole U1326C. The failure was the result of two joints becoming unscrewed during coring. Fine sand found near the top of the tool, 11 m above the bottom, led us to conclude that sand and fluid must have flowed back up the BHA and into the tool during the deployment, jamming the corer in a way that allowed the left-hand threads to come unscrewed.

Degassing experiments

At Site U1326, Core 311-U1326C-12P, which was the only PCS core recovered successfully under pressure, was investigated by controlled shipboard degassing experiments (Table **T18**). This core was taken at a depth of 83.7 mbsf.

The degassing experiment included the following steps. First, the volume and density of sediment inside the inner core barrel of the PCS was monitored by X-ray analysis. Next, the PCS was slowly degassed in a temperature-controlled laboratory (7°C), and the volume and composition of released gas and water, the pressure inside the core, and the ambient air pressure and temperature were monitored (Table **T19**) as described in **"Pressure coring"** in the "Methods" chapter. During the degassing procedure, the vertical density distribution of the PCS cores was repeatedly determined by GRA scans to examine the evolution of gas voids within the sediment. After degassing was completed, we X-rayed the PCS core again, collected the water remaining in the outer core barrel for mass balance considerations, curated the sediment that was extruded from the core, and subsampled it for IW chemistry, dissolved gases, and physical property analyses.

The degassing of Core 311-U1326C-12P yielded 21.0 L of gas. The composition of the released gas did not change significantly in the course of degassing (Table **T19**). Methane was the major component, accounting on average for 91.7% ± 2% of the emitted gas. Nitrogen was the second most abundant gas, contributing 6.1% ± 3% to the gas released. Carbon dioxide, ethane, and higher hydrocarbon concentrations were below the detection limit of the Agilent gas chromatograph used for continuous gas analysis during the degassing experiment (Table **T19**). A subset of gas samples was analyzed using

methods described in "Organic geochemistry" in the "Methods" chapter and yielded an average ethane value of 54 ppmv and C_1/C_2 ratios >16,000. Recovery was particularly low for Core 311-U1326C-12P; the recovered core length was estimated at 35–40 cm from the gamma ray density profiles, though only 27 cm of sediment was extruded from the 1 m long PCS core barrel. Assuming that all methane was released from 40 cm of recovered sediment, mass balance calculations yield a pore space methane concentration of 2965 mM. This concentration equates to 35% of free gas or 40% of gas hydrate in the pore space (Tables T20, T21; Fig. F44). The pressure inside the PCS core dropped below the predicted gas hydrate stability conditions when the port valve of the PCS was first opened and water expanded from the outer core barrel into the manifold system. Therefore, no pressure plateaus or rebounds from dissociation of gas hydrate could be expected and a steady decrease of core pressure versus removed gas volume was observed (Fig. F45).

The X-ray image taken before the core was degassed (Fig. F46) showed 28 cm of sediment at the top of the barrel, along with a gas bubble in the inner core barrel below this sediment. The water below the sediment also appeared to contain some suspended sediment. Repeated gamma ray density profiles (Fig. F46) showed that the sediment at the top of the core remained stationary throughout the degassing experiment, and that a small plug of sediment (~10 cm long) near 60 cm core depth also stayed in place during degassing. However, by the time the final X-ray image was taken, the lower plug of sediment had been homogenized and distributed along the core. Chlorinity measurements in the upper portion of the core show pore water freshening.

Measurements on HYACINTH cores

Simultaneous and automated gamma ray density, *P*-wave velocity, and X-ray measurements were made in the MSCL-P system on Core 311-U1326C-11Y. All measurements took place at 18 MPa (near recovery pressure; 95% of in situ pressure). The velocity and density profiles are shown alongside the X-ray image in Figure F47. The sediments have high velocities compared to density (Fig. F48) indicating there may be some gas hydrate in this short sample, especially when compared to other pressure cores retrieved during Expedition 311 (see "Pressure coring" in the "Site U1327" chapter). This core was transported to the Pacific Geoscience Center, Sidney, B.C., directly after Expedition 311 and was rapidly depressurized. When the core was removed from the storage chamber, some bubbling and "fizzing" was observed in the hard silty material. The sample was considered to be too small and disturbed to warrant being stored under pressure and was curated in a plastic bag.

Gas hydrate concentration, nature, and distribution

Mass balance calculations were only performed for Core 311-U1326C-12P, recovered from a depth of 83.7 mbsf. The gas hydrate content is estimated at 40%, placing it in the GHSZ (Fig. F44) regardless of the choice of thermal gradient (see "In situ temperature profile"). This pressure core was targeted at a zone of extremely high resistivity seen in the LWD data from Hole U1326A, and we can confirm that this high-resistivity zone contains gas hydrate.

IR images (see "Infrared images") and visual observations in the chemistry laboratory show that most of the gas hydrate is associated with sandy layers at Site U1326. Core 311-U1326C-11Y captured some extremely coarse sands and indurated material that was observed to fizz upon depressurization and warming and most likely contained gas hydrate. The core material missing from the base of this core, the sediment/water/gas mixture in the PCS, and the spectacular, spontaneous disassembly of the HRC highlight the difficulty in recovering gas hydrate–bearing sands.

Downhole logging

Logging while drilling

Operations

Hole U1326A was spudded at 1839 mbrf water depth (drillers depth) at 1320 h on 22 September 2005. LWD tools included the GeoVISION resistivity tool, the EcoScope tool, the SonicVISION tool, the TeleScope MWD tool, the ProVision nuclear magnetic resonance tool, and the ADNVISION tool. For details on each tool and the measurements it makes, see "Downhole logging" in the "Methods" chapter.

Similar to the other sites, the uppermost 10 m of the hole was drilled with a rotation rate of 10–15 rpm, a pump flow rate of 190 gpm, and an ROP of 10–15 m/h. We then increased these rates to 40 rpm and 220 gpm until 30 mbsf, and then to 60 rpm and 270 gpm (to start the MWD telemetry), keeping the instantaneous ROP below 50 m/h with depth. The target depth of 300 mbsf (2139 mbrf) was reached at 0410 h on 23 September. Considering the proximity between Holes U1326A and U1327A (~8 nmi apart), it was decided to raise the drill string above the seafloor and move by DP to the location of Hole U1327A without tripping back to the surface.

Gas monitoring with real time logging-while-drilling/measurement-while-drilling data

The LWD logs were acquired to plan coring and pressure coring operations in subsequent holes at Site U1326. As Hole U1326A was drilled without coring, the LWD/MWD data had to be monitored for safety to detect gas entering the borehole. As explained in **"Downhole logging"** in the "Methods" chapter, the primary measurement used for gas monitoring was annular pressure while drilling, which is measured by the EcoScope tool in the borehole annulus. We looked for sudden decreases >100 psi in the annular pressure, which could be caused by low-density gas entering the borehole. We also monitored pressure increases of the same magnitude, which could be the result of fluid acceleration caused by a gas kick (Aldred et al., 1998).

Figure **F49** shows the measured borehole fluid pressure profile in Hole U13265A after subtraction of the best-fit linear trend. The borehole fluid pressure shows only small fluctuations over the trend, except for a positive pressure anomaly (~30 psi) centered at 182 mbsf. Whereas positive drilling fluid pressure anomalies at other sites were correlated with hole enlargements, the ultrasonic caliper log (Fig. **F49**) shows no hole diameter anomaly near 182 mbsf; thus, the reason for the pressure increase is not clear. One possibility is that a partial borehole collapse somewhere above the LWD string caused a sudden influx of cuttings in the annulus. The observed fluid pressure anomalies were well below the 100 psi level that would have required preventive action.

We also monitored the coherence of the sonic waveforms acquired by the SonicVISION tool, focusing on the velocity of the fluid wave in the borehole. Loss of coherence in the waveforms and a slower velocity for the drilling fluid indicate the presence of gas. The sonic waveform coherence image in Figure **F49** shows almost everywhere a well-defined fluid arrival with a slowness of ~200 µs/ft, which corresponds to the expected fluid velocity of ~1500 m/s. The only anomalies are at two intervals (80–87 and 258–261 mbsf), where the fluid arrival suddenly disappears. As will be shown later, these two intervals are characterized by high resistivity. The shallower one is presumably a gas hydrate–rich interval where some gas hydrate dissociation may have generated free gas during drilling. The deeper interval is located below the BSR depth, estimated from seismic reflection data (234 mbsf), and may contain free gas. Even if the low coherence of the drilling fluid arrival was caused by free gas, it is important to stress that the fluid pressure anomalies were small and that if gas was in the drilling fluid it had to be in low concentrations.

Logging data quality

Figure **F49** also shows the quality control logs for Hole U1326A. The ROP was generally 60 m/h or less in the interval from the seafloor to TD. This is sufficient to record one measurement every 4 cm (~25 measurements/m) in the GeoVISION resistivity, and no significant resolution loss was observed with variation in ROP. The ultrasonic caliper log, which is a direct measurement of the borehole diameter recorded by the EcoScope tool, is our best indicator of borehole size. It shows a large washout near the seafloor (10–20 mbsf), where the hole diameter reached 13 inches (33 cm), and many smaller hole enlargements throughout the rest of the hole. In several cases, borehole diameter restrictions (<9 inches or 23 cm) can be observed immediately below these enlargements (e.g., at 110, 206, and 226 mbsf), suggesting that the washouts were generated above resistant intervals that were hard to drill. Except for these enlargements and restrictions, the hole diameter was generally just above 10 inches (25 cm).

Despite these hole irregularities, the density correction, calculated from the difference between the short- and long-spaced density measurements, generally varies from 0 to 0.2 g/cm^3 (Fig. **F49**), showing the good quality of the density measurements. Figure **F50** is a summary of the Hole U1326A LWD gamma ray, density, resistivity, and resistivity image logs with density and porosity measurements from cores from Holes U1326C and U1326D superimposed (see **"Physical properties"**).

The depth relative to the seafloor was fixed for all LWD logs by identifying the step change in the gamma ray log associated with the seafloor. For Hole U1326A, the gamma ray logging pick for the seafloor was at a depth of 1838 mbrf.

Wireline logging

Operations

Hole U1326D was drilled to a depth of 300 mbsf, which was reached at 1330 h on 26 October 2005. The weather conditions were favorable (ship's heave was ~3 m), but because of a poor weather forecast that required that we leave the site by midday on 27 October, it was decided to run a single, armless tool string that included the most critical log still missing (sonic velocity). The tool string consisted of the SGT, the DSI, and the DIT. For details on the different tools, see **"Downhole logging"** in the "Methods" chapter.

After hole preparation, rig up of the tool string started at 2210 h and was completed at 2308 h on 26 October. The bottom of the hole was reached without complications at 2139 mbrf (302 mbsf), and we

started logging a first pass at 0034 h on 27 October. The first pass was completed at 1936 mbrf (99 mbsf), with the top of the 34 m long tool string just below the drill pipe. We lowered the tool string to the bottom of the hole again and started a second pass at 0127 h. The tool string reached the seafloor at 0235 h, and was pulled back onto the rig floor at 0345 h. Rig down of all wireline equipment was completed at 0505 h on 27 October.

Logging data quality

As we did not run a caliper log in Hole U1326D, we cannot clearly determine the effects of hole diameter on the wireline logging measurements. There are a few intervals (e.g., ~100 and 180 mbsf) where both the gamma ray and the induction resistivities have very low values, which could be the result of an enlarged hole (Fig. **F51**). Apart from these anomalous intervals, the gamma ray and induction logs are of very good quality.

A comparison of the gamma ray, resistivity, and acoustic logs measured in the two passes show an excellent correlation (Fig. **F51**). The acoustic waveforms and slowness-time coherence projection are shown in Figure **F52.** The velocity profiles acquired in the two passes are very similar, and almost no additional processing was required to derive reliable compressional (V_P) and shear (V_S) wave velocities.

Despite the absence of caliper data, the analysis of the sonic waveforms and coherences in Figure **F52** suggests that the borehole was in good condition. The very clear *P*-wave arrivals in the monopole waveforms generate a strong coherence peak that makes V_P labeling extremely robust over the entire hole. In addition to the clear *P*-wave arrivals, the monopole waveforms also display a strong arrival at ~2 ms, which likely corresponds to a fluid wave with a uniform velocity that creates a second coherence "track" at a nearly constant velocity of ~1500 m/s. In the interval between ~70 and 80 mbsf, where both velocity and resistivity are very high, the monopole waveforms display low amplitudes that are characteristic of very high gas hydrate concentrations. The low waveform amplitudes for most of the lower dipole and a portion of the upper dipole could possibly result from the attenuating influence of disseminated gas hydrate. This effect would be accordingly stronger on the higher frequency waveforms from the lower dipole. This effect could also be the result of poor hole conditions, but the high quality of the monopole waveforms suggests otherwise.

The depths relative to seafloor for all of the wireline logs were fixed by identifying the step change in the gamma ray log associated with the seafloor. The gamma ray pick for the seafloor was at 1837 mbrf in Hole U1326D.

Logging-while-drilling and wireline logging comparison

Figure **F53** shows a comparison of LWD (Hole U1326A) and wireline (Hole U1326D) data, using the gamma ray and resistivity logs. The LWD gamma ray log gives higher readings (100 gAPI on average) than the wireline log (40 gAPI on average), and the curves do not have features that can be easily correlated. Part of the reason for this difference may be that the wireline gamma ray log has not been corrected for the effect of hole size, as we could not run a caliper log. The ultimate reason for this discrepancy is not clearly understood. However, wireline data are consistent with data recorded during Leg 146.

The comparison of resistivities shows similar values measured by the LWD and wireline logs. The prominent, asymmetric resistivity high that is clearly visible in the LWD logs at 72–100 mbsf (Fig. **F50**) is found with the same shape in the wireline resistivity logs, only displaced upward by ~12 m to 60–88 mbsf. Hole U1326D, where the wireline logs were measured, was drilled ~20 m southwest of LWD Hole U1326A. As described in **"Logging-while-drilling borehole images,"** borehole images show layers steeply dipping to the north-northeast. A northward-dipping structure is consistent with finding the same stratigraphic horizon in a shallower position in Hole U1326D compared to Hole U1326A. The resistivity peak centered around 260 mbsf in the LWD resistivity logs, on the other hand, does not clearly correlate to a similar shallower peak in the wireline logs; the wireline logs instead show four peaks between 195 and 255 mbsf that do not have any obvious counterpart in the LWD logs. Finally, as noted earlier, the very low resistivities measured in the wireline logs at ~100 and 180 mbsf are likely to be the result of an enlarged hole.

Logging units

The logged section in Holes U1326A and U1326D can be divided into three logging units, based on obvious changes in the LWD and wireline gamma ray, density, electrical resistivity, and acoustic measurements (Figs. **F50, F51, F52**). These three logging units have no obvious correspondence to the lithostratigraphic units described in **"Lithostratigraphy."** We defined the depth intervals of the logging units mainly on the basis of the more complete suite of LWD logs acquired in Hole U1326A. As noted above, the wireline logs from Hole U1326D show similar horizons in a position that is shallower by ~12 m,

and the depth intervals of the logging units need to be correspondingly adjusted in Hole U1326D.

Logging Unit 1 (0–72 mbsf in Hole U1326A) is characterized by a resistivity trend that steadily increases from ~1 Ωm near the seafloor to ~1.5 Ωm at the bottom of the unit. This increase in resistivity with depth is matched by an increase in density (from 1.7 g/cm³ near the seafloor to 2 g/cm³ at 120 mbsf) and a decrease in porosity (from 70% near the seafloor to 50% at 120 mbsf). This unit shows only a few small resistivity peaks (e.g., at ~52 and 60 mbsf in the LWD logs; Fig. **F50**) that may be attributed to gas hydrate.

Logging Unit 2 (72–240 mbsf in Hole U1326A; 60–228 mbsf in Hole U1326D) is characterized by uniform density and porosity trends, with values around 2 g/cm³ and 45%, respectively. Resistivity shows a prominent high at 72–107 mbsf in Hole U1326A, with peaks above 40 Ωm. This interval of high resistivity displays a number of alternating, thin intervals of very high and low resistivity, spanning the range 2–40 Ωm. These thin intervals are especially well defined between 77 and 90 mbsf (Fig. **F50**). These high and low resistivities are likely to correspond to alternating layers with high and low gas hydrate concentrations, respectively. Below this high-resistivity interval at the top, the rest of Unit 2 (107–240 mbsf in Hole U1326A; 95–228 mbsf in Hole U1326D) has a constant background value of ~1.5 Ωm. The *P*-wave velocities (V_P) measured by wireline logging in Hole U1326D (Fig. **F51**) show highly variable values (between 1750 and >3000 m/s) in the same interval (60–90 mbsf) where the wireline log resistivities reach high values and are variable. The high V_P values are consistent with high concentrations of gas hydrate, as pure gas hydrate has V_P values of 3800–4000 m/s (e.g., Pearson et al., 1983). For the rest of this unit, V_P increases from ~1700 m/s below 90 mbsf to 2000 m/s at the bottom of Unit 2 (228 mbsf in Hole U1326D).

The top of logging Unit 3 (240–300 mbsf in Hole U1326A; 228–288 mbsf in Hole U1326D) shows a subtle increase in density, from ~2 g/cm³ at the top to 2.1 g/cm³ at 255 mbsf, and remains constant to 300 mbsf. This density trend is matched by a corresponding decrease in porosity (from 40% at the top to 35% at 255 mbsf). The background resistivity also increases slightly and displays a clear peak that reaches 5 Ωm at 255–261 mbsf (Fig. **F50**). This resistivity peak could be caused by gas hydrate or free gas. Free gas seems more likely, as this interval is located below the projected BSR depth estimated from seismic reflection data (234 mbsf), and should be below the base of the GHSZ. On the other hand, V_P is at least 1700 m/s in Unit 3 (Fig. **F51**), and there is no sign of the low velocities expected if free gas were present. The relatively high velocities observed could lead to an increase in the depth of the BSR estimated from reflection traveltimes.

Logging-while-drilling borehole images

The GeoVISION, ADNVISION, and EcoScope LWD tools generate high-resolution images of borehole log data. The ADNVISION and EcoScope tools produce images of density and hole radius (computed on the basis of the density correction, which depends on the borehole standoff). The GeoVISION tool produces a gamma ray image and shallow, medium, and deep depth of investigation resistivity images.

Figure **F54** shows some of the LWD images collected by the EcoScope and GeoVISION tools. It should be noted that the display in Figure **F54** is highly compressed in the vertical direction. The unwrapped images are ~90 cm wide (for an 11 inch diameter borehole), and the vertical scale is compressed by a factor of ~37:1. These high-resolution images can be used for detailed sedimentological and structural interpretations and to image gas hydrate distribution in sediments (e.g., in layers, nodules, or fractures). Gas hydrate–bearing sediments exhibit high resistivities within intervals of uniform or low bulk density. Layers with high resistivities and high densities are likely to be low-porosity, compacted, or carbonate-rich sediments.

The images suggest that there may be high concentrations of gas hydrate in thin layers between 81 and 100 mbsf in Hole U1326A, where densities are generally low and high-resistivity, gas hydrate–rich layers (bright in the resistivity images of Fig. **F54**) alternate with low-resistivity layers (dark in the images of Fig. **F54**) that are likely to contain little or no gas hydrate. The images also clearly show a number of hole enlargements, which are imaged as dark bands in Figure **F54** at depths of ~110, 206, and 225 mbsf. These are the same washouts detected by the LWD ultrasonic caliper (Fig. **F49**).

When the images are examined with less vertical exaggeration than in Figure **F54,** they clearly show that the layers identified in Hole U1326A are dipping to the north-northeast with dips between 45° and 85° (Fig. **F55**). This is in agreement with the west-northwest–east-southeast strike of the uplifted ridge where Hole U1326A was drilled and with evidence for landward-dipping reflectors in seismic profiles. It should be pointed out that reflections on the seismic profiles across this ridge show dips of 15° or less, but seismic reflection data cannot image steeply dipping structures. Also, the observation of steep dips in Hole U1326A should be interpreted carefully. In a complex tectonic structure (e.g., a faulted anticline or a

stack of imbricated thrust sheets) the dips measured along a vertical line may vary significantly over short horizontal distances, and their interpretation can be variable (for examples of structural interpretation of dips from borehole images, see Luthi, 2001).

Logging porosities

Sediment porosities can be determined from analyses of recovered cores and from downhole measurements (see **"Physical properties"** and **"Downhole logging,"** both in the "Methods" chapter). Data from the LWD density and neutron logs from Hole U1326A were used to calculate sediment porosities. Core-derived physical property data, including porosities (see **"Physical properties"**), were used to both calibrate and evaluate the log-derived sediment porosities.

The LWD log–derived density measurements were used to calculate sediment porosities (ϕ) using the standard density-porosity relation

$$\phi = (\rho_g - \rho_b)/(\rho_g - \rho_w).$$

We used a constant water density (ρ_w) of 1.03 g/cm^3 and a grain/matrix density (ρ_g) of 2.76 g/cm^3, which is the average grain density measured in core samples (see **"Physical properties"**). The density log–derived porosities range from ~60% near the seafloor to ~40% at 300 mbsf (Fig. **F56**). In several intervals (e.g., 10–20, 105–110, and 205–210 mbsf) hole enlargements resulted in an erroneously low value of density, and corresponding porosity values that are too high.

The LWD neutron porosity log from Hole U1326A (Fig. **F56**) yielded sediment porosities ranging from an average value of ~70% near the seafloor to ~50% at 350 mbsf. As noted earlier, porosities measured by the neutron log are expected to be higher than those computed from the density log in clay-rich sediments because the neutron log essentially measures hydrogen abundance, and hydrogen in clay minerals is counted as porosity. The EcoScope neutron porosity shown in Figure **F56** is the "best thermal neutron porosity," which has been corrected for the effect of clay, so that it is only slightly higher than the density porosity. Like the density porosity, the neutron porosity log also gives values that are too high where the hole is enlarged.

The comparison of core- and LWD-derived porosities in Figure **F56** shows good agreement throughout the logged interval, with the density porosities being slightly lower and the neutron porosities slightly higher than the core porosities.

Gas hydrate and free gas occurrence

As previously discussed (see "**Downhole logging**" in the "Methods" chapter) the presence of gas hydrate is generally characterized by increases in electrical resistivity and acoustic velocity that are not accompanied by a corresponding decrease in porosity. A decrease in porosity alone in a water-saturated sediment can result in an increase in resistivity and acoustic velocity. Resistivity logging data from Holes U1326A and U1326D show a number of positive resistivity anomalies without a corresponding decrease in porosity (Figs. **F50, F51**), suggesting that there are several intervals where gas hydrate may be present.

Water saturation from Archie's equation

To estimate the amount of gas hydrate at Site U1326, we used the Archie relation (e.g., Collett and Ladd, 2000)

$$S_w = [(a \times R_w)/(\phi^m \times R_t)]^{1/n},$$

where

- S_w = water saturation,
- a = tortuosity coefficient,
- R_w = formation water resistivity,
- ϕ = density porosity computed from the ADNVISION enhanced resolution bulk density,
- m = cementation coefficient,
- R_t = GeoVISION high-resolution button deep average resistivity, and
- n = saturation coefficient.

We use the button deep resistivity instead of the ring resistivity because the button deep resistivity matches the resistivities with the greatest depth of investigation measured by the EcoScope tool (except for having a higher resolution), whereas the ring resistivity is generally lower than the EcoScope deep resistivities.

Gas hydrate saturation (S_h) is the percentage of pore space in sediment that is occupied by gas hydrate, which is the complement of the water saturation S_w:

$$S_h = 1 - S_w.$$

The procedure followed to estimate S_w with Archie's relation is illustrated in Figure **F57.** We first computed porosity from the density log as described above with a water density ρ_w of 1.03 g/cm^3 and a grain/matrix density ρ_g of 2.76 g/cm^3 (see **"Physical properties"**).

To estimate the formation water resistivity (R_w), we started by constructing a salinity versus depth function based on IW salinity measurements (see **"Interstitial water geochemistry"**). This salinity versus depth function simply consists of a constant value of 34. At every logging depth, we combined the salinity value with a formation temperature obtained from the geothermal gradient estimated from the downhole formation temperature measurements (see **"In situ temperature profile"**) and used the formulas of

Fofonoff (1985) to obtain the corresponding value of the water resistivity R_w.

To estimate the water saturation S_w we also need to choose values for the Archie coefficients a and m. One way to do this is to choose a logged interval where the sediments can be assumed to be water saturated and to fit a and m to a plot of measured resistivity versus porosity, known as a "Pickett plot" (e.g., Doveton, 1994). In marine sediments, however, the range of porosity is relatively small and it is not possible to obtain a robust estimate of both a and m. We prefer to set $a = 1$, which is physically the most realistic value because it gives a resistivity equal to the formation water resistivity when the porosity is 100%. We then compute an "estimated m" coefficient by

$$m_{est} = -\log(F)/\log(f),$$

where $F = (R_t/R_w)$ is the formation factor. This m_{est} curve should give the appropriate value to be used in Archie's equation in water-saturated intervals and will give anomalously high values in intervals that contain hydrocarbons. A reasonable value of $m = 2.5$ can be chosen from the baseline trend of the m curve shown in Figure **F57.**

The next step is to compute the resistivity R_0 predicted by Archie's equation for a water-saturated formation of a given porosity, which is given by

$$R_0 = (a \times R_w)/\phi^m.$$

Using Archie coefficients of $a = 1$ and $m = 2.5$, we computed an R_0 curve that generally follows the measured resistivity R_t, but is significantly lower than R_t in several intervals, mostly in logging Unit 2 (Fig. **F57**). Finally, we computed the water saturation S_w using a saturation coefficient $n = 2$.

As noted earlier, several hole enlargements resulted in logging density values that are erroneously low and approach water density. In the Archie interpretation, these low densities translate into artificially high porosities, low values for the predicted water-saturated resistivity R_0, and low values of water saturation S_w. These anomalous intervals should be ignored and are marked by gray overlays in Figure **F57.**

Figure **F57** shows a clear interval between 60 and 100 mbsf where the measured resistivity R_t generally exceeds the resistivity R_0 predicted for water-saturated conditions, and where the inferred water saturations can be as low as ~20%. This interval encompasses the bottom of logging Unit 1 and the top of Unit 2, and the high-resolution LWD porosity and resistivity logs used in Figure **F57** show that it is very heterogeneous, being composed of many alternating layers of highly variable porosity and resistivity. We interpret the 60–100 mbsf interval as a sequence of thin, sandy, gas hydrate–rich layers intercalated with clay-rich layers that may contain little or no gas hydrate. This interpretation is in general agreement with the pore water freshening observed in sand layers at Site U1326 (see the pore water salinity data in Fig. **F57** and **"Interstitial water geochemistry"**).

Comparison with infrared images

The IR core images taken on the catwalk measure the core liner temperature, and cold anomalies in the IR images caused by gas hydrate dissociation give an independent "map" of gas hydrate concentrations (see **"Physical properties"**). Figure **F58** shows a comparison of the LWD and wireline resistivity logs with the IR images. Some of the IR cold temperature anomalies correlate with layers of high resistivity. For example, the IR images show a thin cold interval centered at 247 mbsf that corresponds to a high-resistivity peak (~3 Ωm) in the wireline logs). Other cold intervals in the IR images are harder to correlate to high-resistivity peaks in the wireline logs because of incomplete core recovery. The correlation between the IR images (taken on cores from Holes U1326C and U1326D) and the LWD logs (Hole U1326A) needs to be done with care because the dip of the sedimentary structure noted earlier will require a depth shift.

References

Aldred, W., Cook, J., Bern, P., Carpenter, B., Hutchinson, M., Lovell, J., Rezmer-Cooper, I., and Leder, P.C., 1998. Using downhole annular pressure measurements to improve drilling performance. *Oilfield Rev.,* 10(4):40–55.

Collett, T.S., and Ladd, J., 2000. Detection of gas hydrate with downhole logs and assessment of gas hydrate concentrations (saturations) and gas volumes on the Blake Ridge with electrical resistivity log data. *In* Paull, C.K., Matsumoto, R., Wallace, P.J., and Dillon, W.P. (Eds.), *Proc. ODP, Sci. Results,* 164 [Online]. Available from World Wide Web: **http://www-odp.tamu.edu/publications/164_SR/chap_19/chap_19.htm.**

Collett, T.S., Riedel, M., Malone, M.J., and the Expedition 311 Project Team, 2005. Cascadia margin hydrates. *IODP Sci. Prosp.,* 311. **doi:10.2204/iodp.sp.311.2005**

Davis, E.E., Currie, R.G., and Sawyer, B.S., 1987. Marine geophysical maps of western Canada: regional SeaMARC II acoustic image mosaics and Sea Beam bathymetry. *Geol. Surv. Can.,* Maps 2-1987 through 17-1987 (scale 1:250,000).

Davis, E.E., Hyndman, R.D., and Villinger, H., 1990. Rates of fluid expulsion across the northern Cascadia accretionary prism: constraints from new heat flow and multichannel seismic reflection data. *J. Geophys. Res.,* 95:8869–8889.

Doveton, J.H., 1994. Geologic log analysis using computer methods. *AAPG Comp. Appl. Geol.,* 2:169.

Fofonoff, N.P., 1985. Physical properties of seawater: a new salinity scale and equation of state for seawater. *J. Geophys. Res.,* 90:3332–3342.

Hyndman, R.D., and Davis, E.E., 1992. A mechanism for the formation of methane hydrate and seafloor bottom-simulating reflectors by vertical fluid expulsion. *J. Geophys. Res.,* 97:7025–7041.

Hyndman, R.D., and Wang, K., 1993. Thermal constraints on the zone of major thrust earthquake failure: the Cascadia subduction zone. *J. Geophys. Res.,* 98:2039–2060.

Luthi, S.M., 2001. *Geological Well Logs: Their Use in Reservoir Modeling:* Berlin (Springer-Verlag).

Pearson, C.F., Halleck, P.M., McGuire, P.L., Hermes, R., and Mathews, M., 1983. Natural gas hydrate deposits: a review of in-situ properties. *J. Phys. Chem.,* 87:4180–4185.

Pimmel, A., and Claypool, G., 2001. Introduction to shipboard organic geochemistry on the *JOIDES Resolution. ODP Tech. Note,* 30 [Online]. Available from World Wide Web: **http://www-odp.tamu.edu/publications/tnotes/tn30/INDEX.HTM.**

Sloan, E.D., 1998. *Clathrate Hydrates of Natural Gases* (2nd ed.): New York (Marcel Dekker).

Xu, W., 2002. Phase balance and dynamic equilibrium during formation and dissociation of methane gas hydrate. *Fourth Int. Conf. Gas Hydrates,* 19023:199–200.

Xu, W., 2004. Modeling dynamic marine gas hydrate systems. *Am. Mineral.,* 89:1271–1279.

Publication: 28 October 2006
MS 311-104

Figure F1. Location of site survey data around Site U1326 (proposed Site CAS-03C; Collett et al., 2005). Shown are positions of common depth points (CDPs) of multichannel seismic (MCS) data and shot points of single channel seismic (SCS) data. Axes are Universal Transverse Mercator (UTM) projection easting and northing coordinates using the WGS-84 reference.

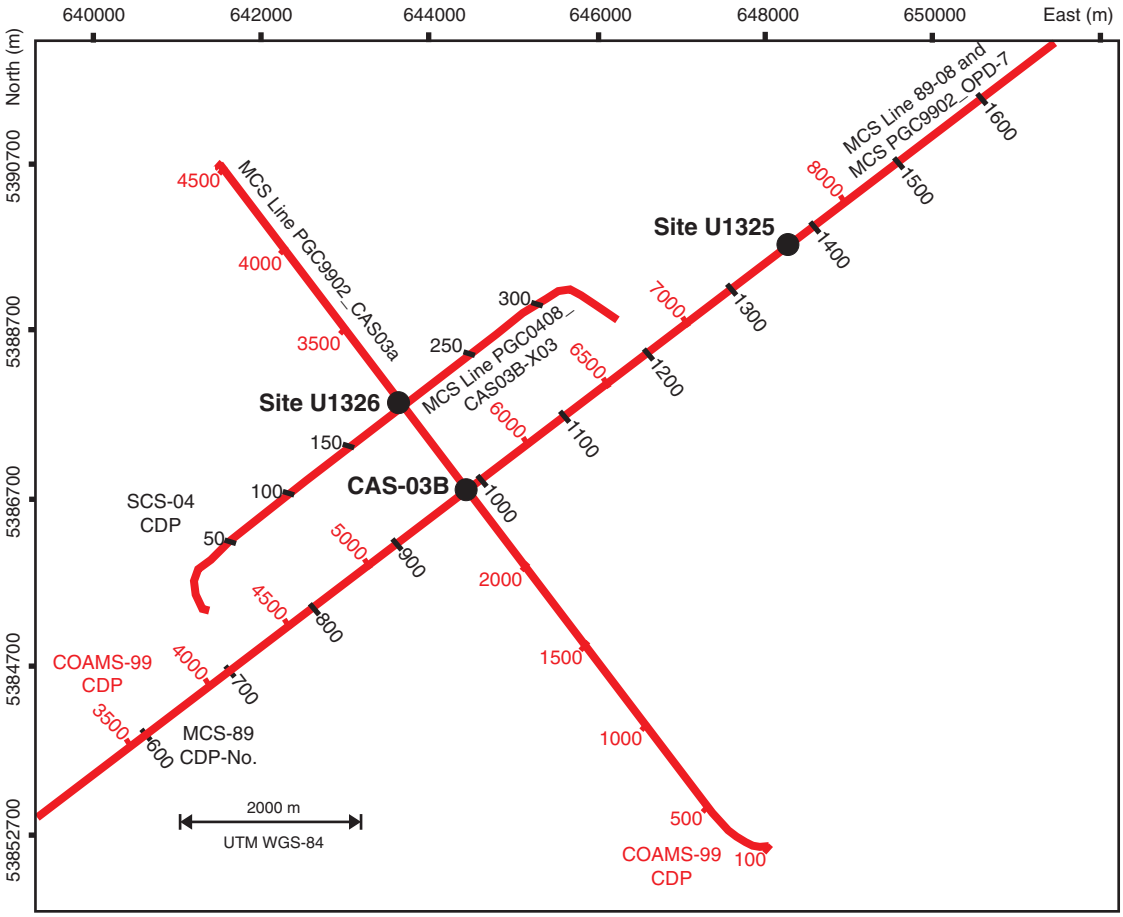

Figure F2. Section of multichannel seismic Line PGC9902_CAS03a crossing the ridge in a southeast–northwest direction. A series of faults is clearly visible resulting in a seafloor displacement of up to 25 m. CDP = common depth point, V.E. = vertical exaggeration, BSR = bottom-simulating reflector.

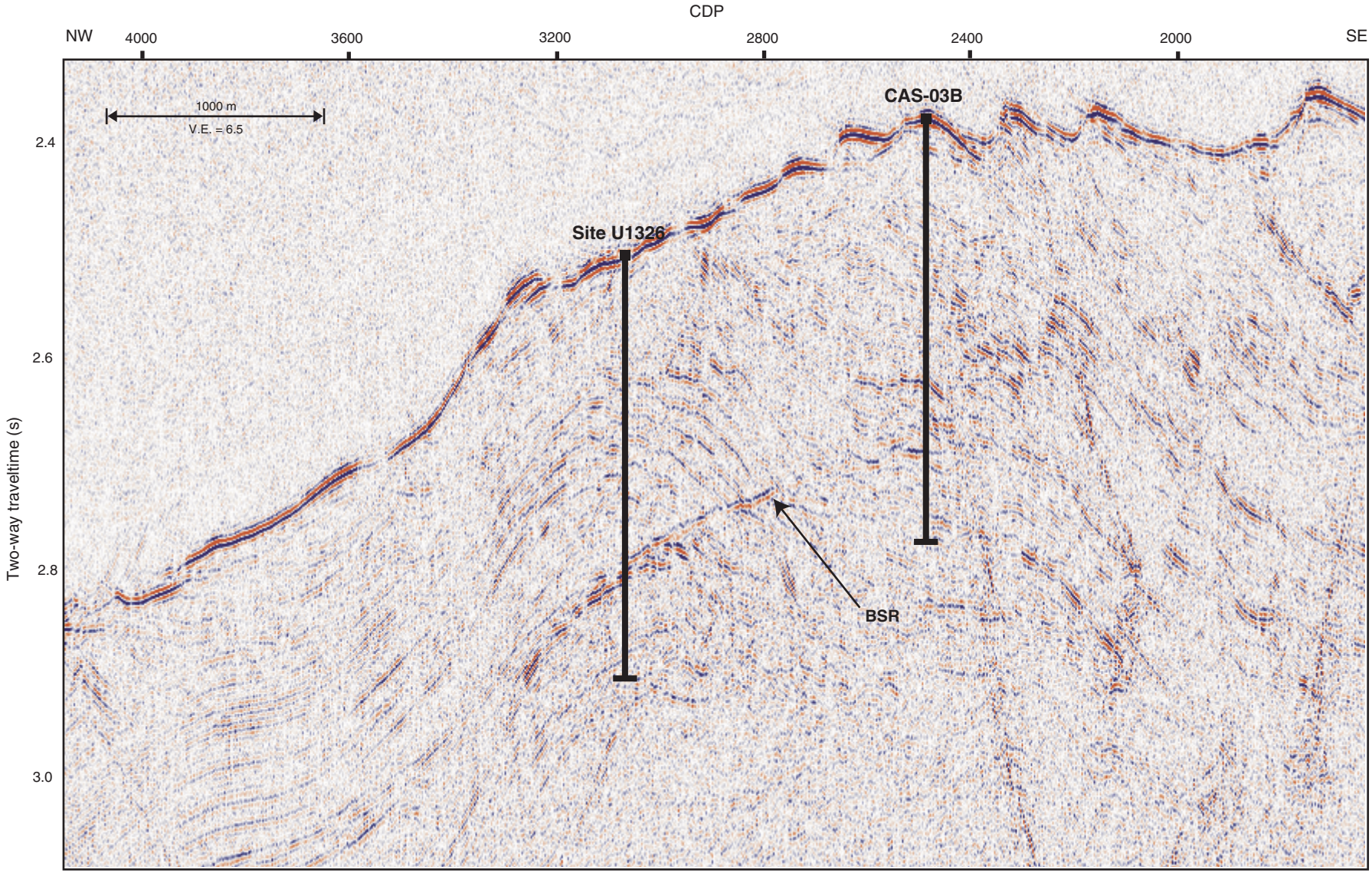

Figure F3. Section of multichannel seismic Line 89-08 crossing the ridge in a southwest–northeast direction. A bottom-simulating reflector (BSR) is prominent underneath the center of the ridge. The reflectivity of the ridge is asymmetric and may reflect changes in internal deformation. CDP = common depth point, V.E. = vertical exaggeration.

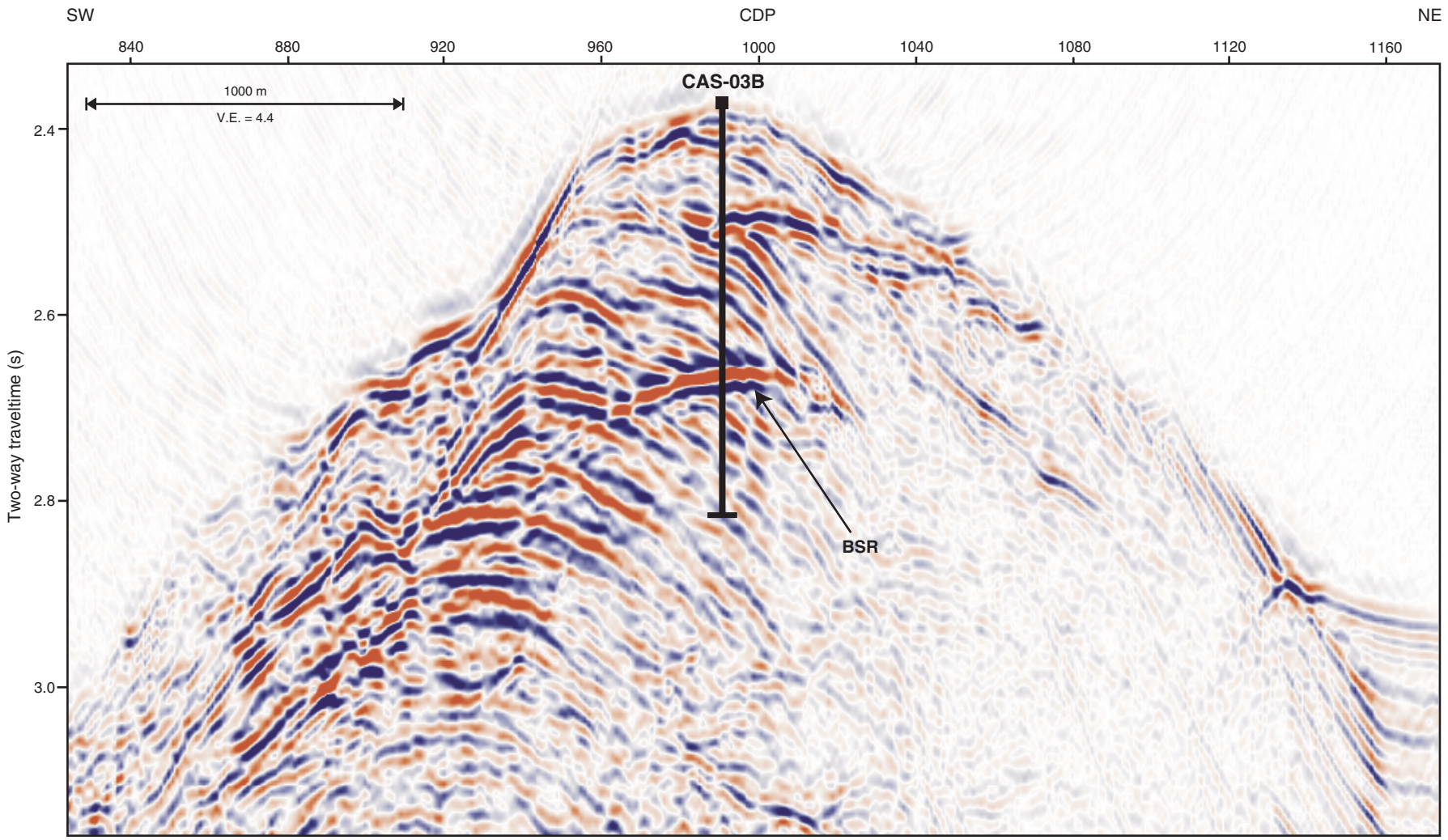

Figure F4. Section of multichannel seismic (MCS) Line PGC9902_ODP-7, identical in location to MCS Line 89-08, crossing the ridge in a southwest-northeast direction. The bottom-simulating reflector (BSR) is less strongly pronounced compared to MCS Line 89-08 and a similar difference in reflectivity pattern between the southwest and northeast flank of the ridge is observed. CDP = common depth point, V.E. = vertical exaggeration.

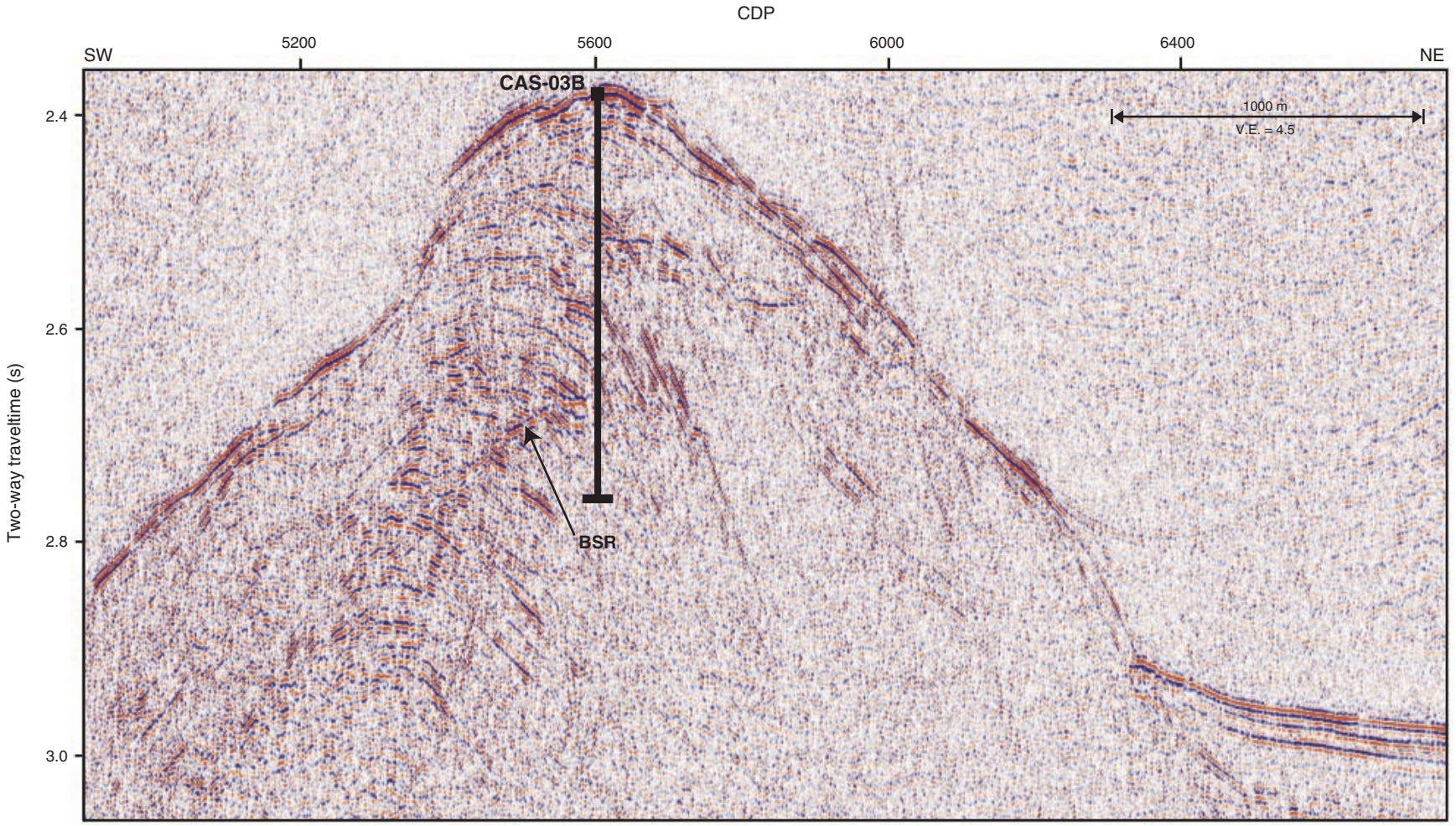

Figure F5. Section of singlechannel seismic Line PGC0408_CAS03B_X03 crossing over Site U1326. BSR = bottom-simulating reflector, CDP = common depth point.

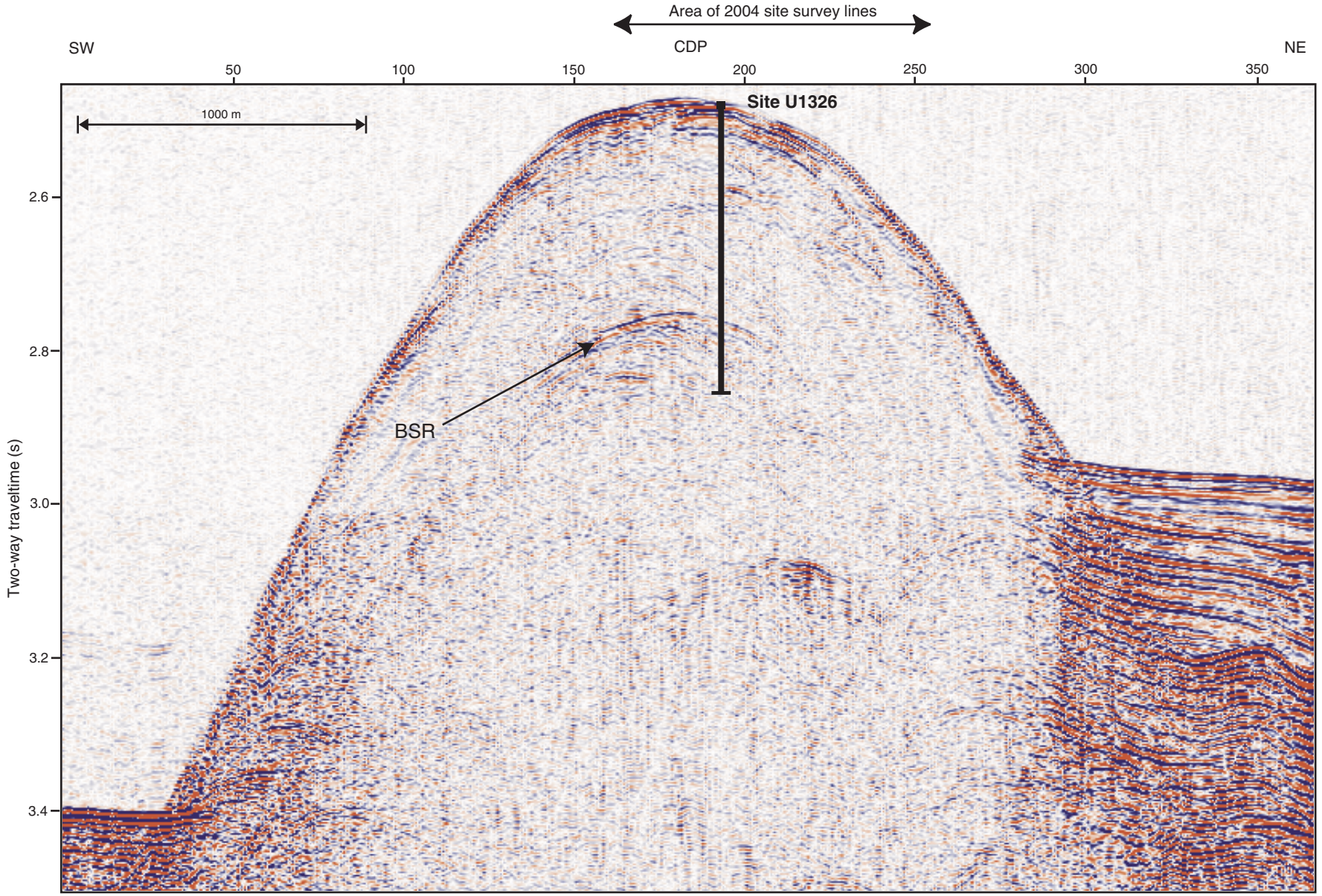

Figure F6. Location of holes drilled at Site U1326, showing track lines with seismic survey shot points. Axes are universal transverse Mercator (UTM) projection easting and northing coordinates using the WGS-84 reference.

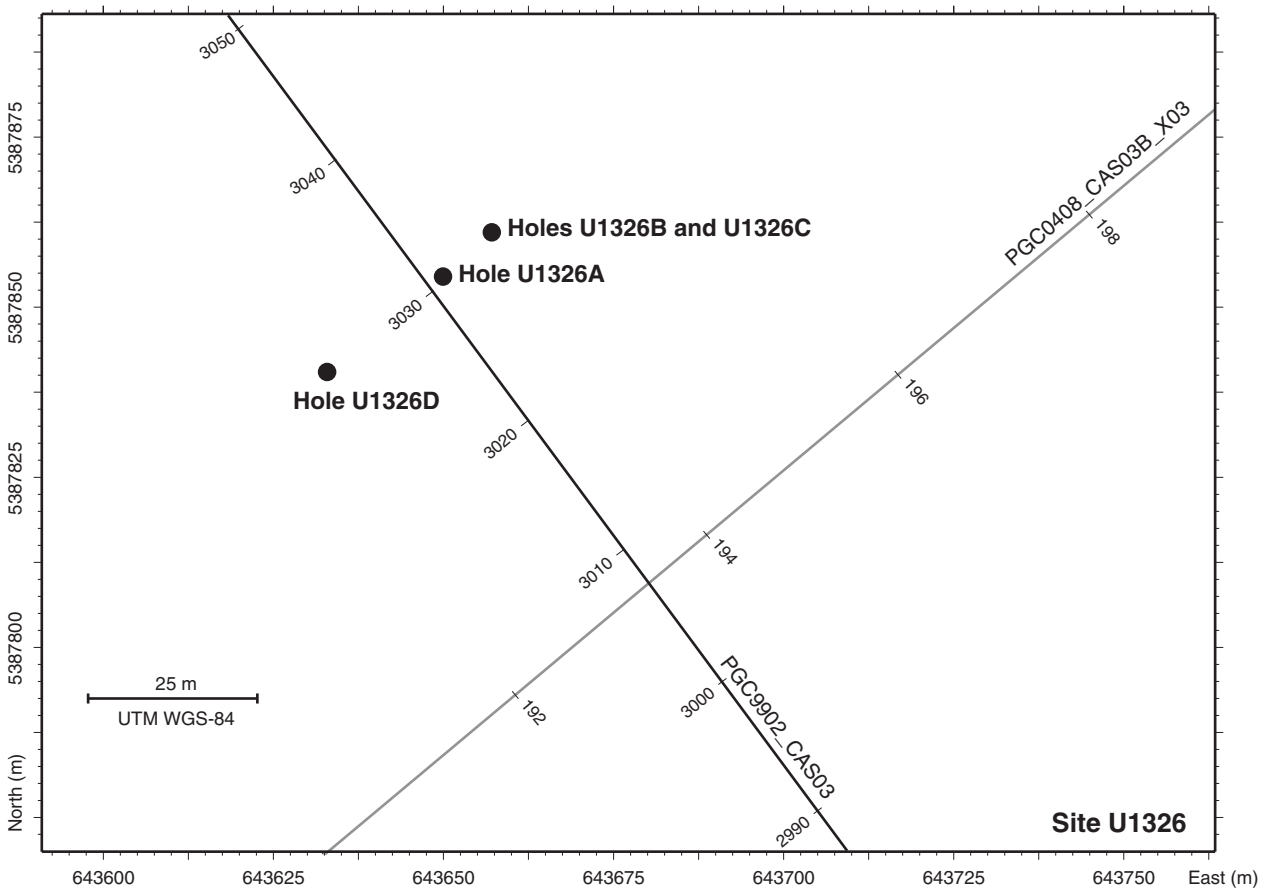

Figure F7. Lithostratigraphic summary for Holes U1326C (solid circles) and U1326D (open squares) showing the percentage of clay, silt, sand, biogenic opal (diatoms, radiolarians, siliceous spicules, silicoflagellates), foraminifers, and nannofossils in the major lithology; clay, silt, and sand in the minor lithology; and AMST color reflectance (a*).

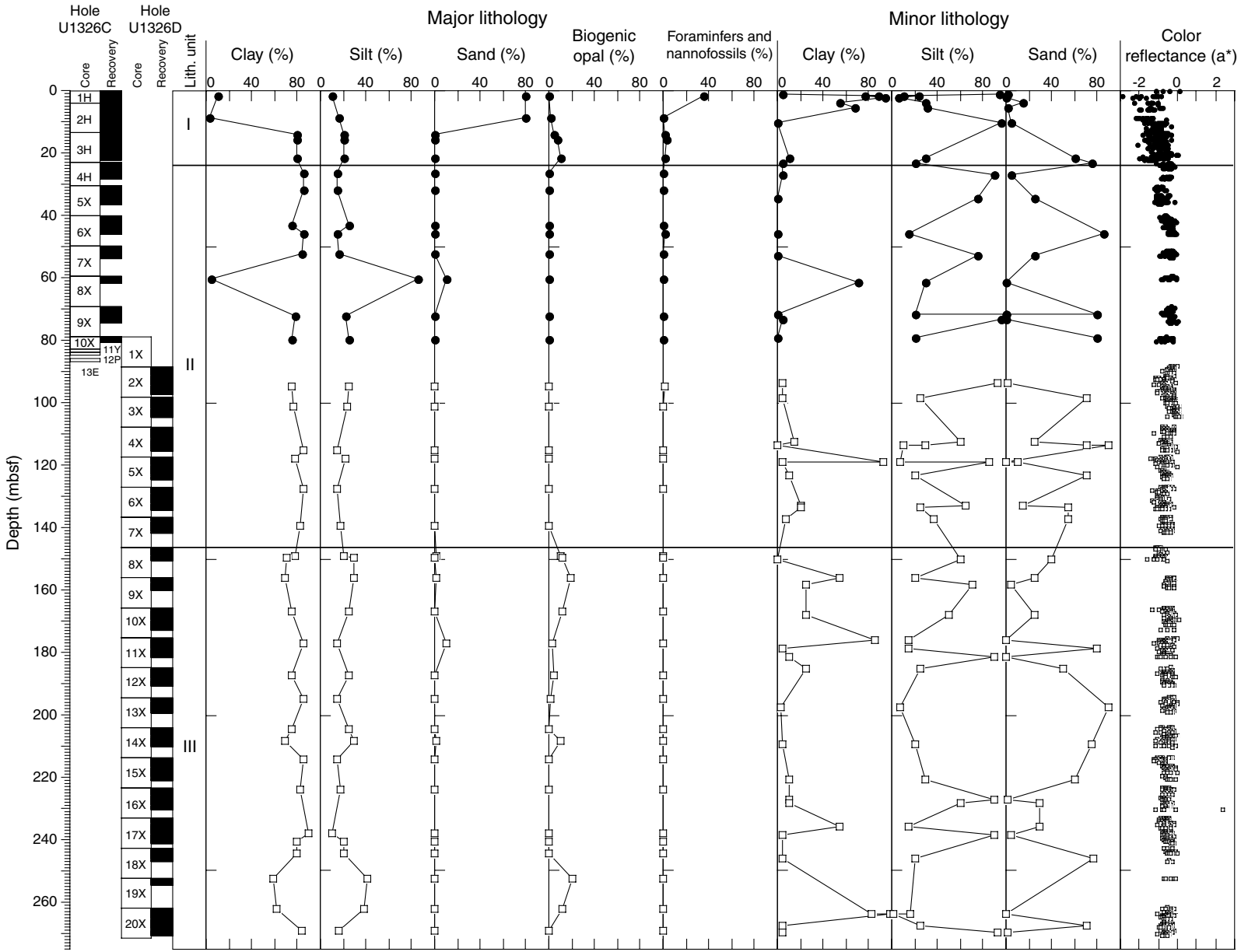

Figure F8. Dipping silty clay showing gradual color changes from dark greenish gray to dark gray in lithostratigraphic Unit I (interval 311-U1326C-3H-3, 80–110 cm). The greenish intervals have more abundant diatoms (as much as 10%).

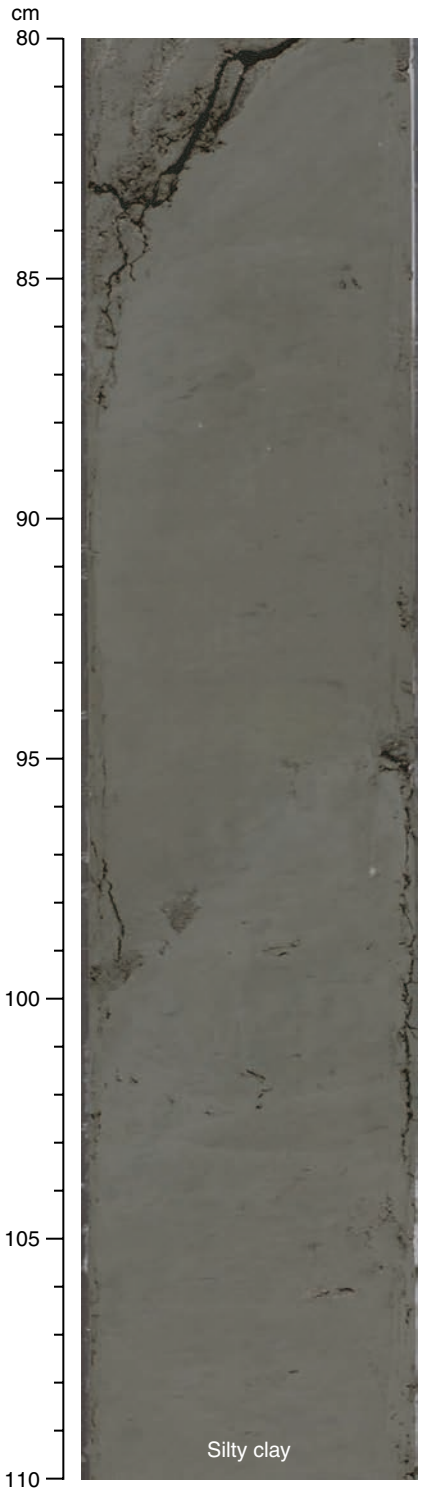

Figure F9. Dark gray silty clay with several evenly spaced, dipping dark gray sand layers and lenses in lithostratigraphic Unit I (interval 311-U1326C-2H-2, 0–32 cm).

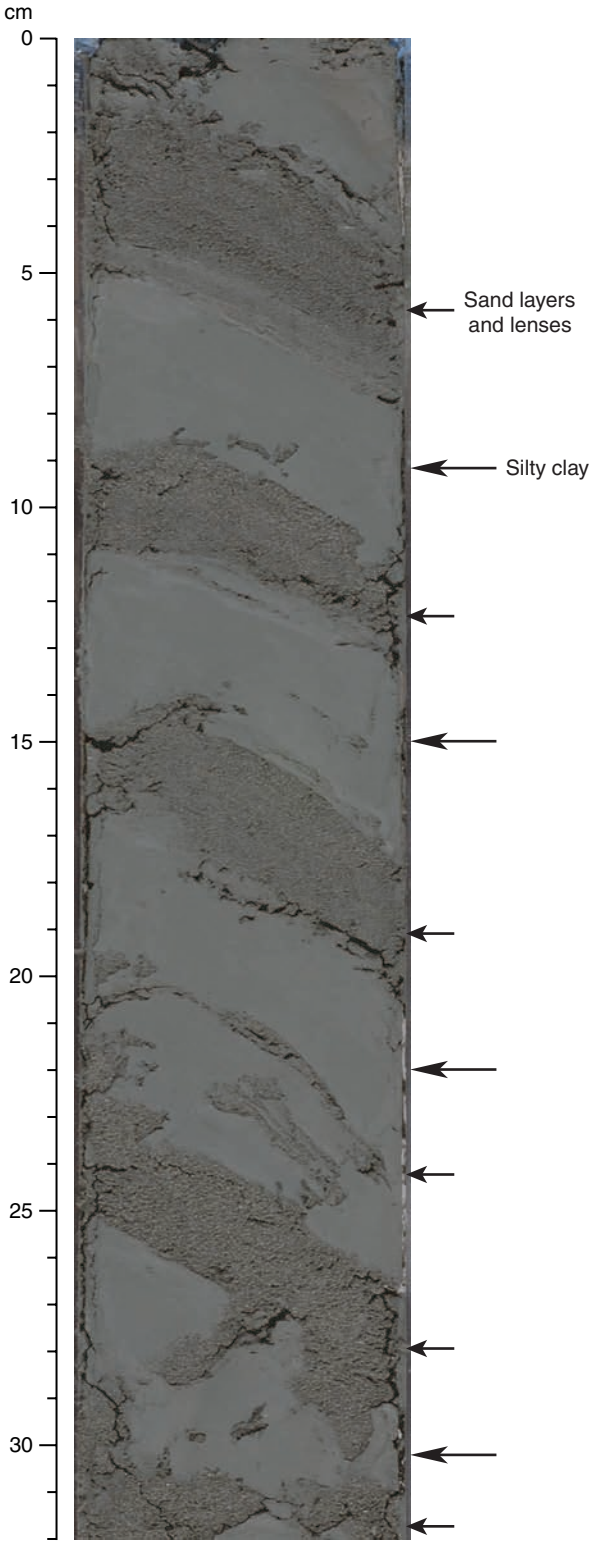

Figure F10. Bivalve shell fragments in lithostratigraphic Unit I (interval 311-U1326C-1H-2, 65–80 cm).

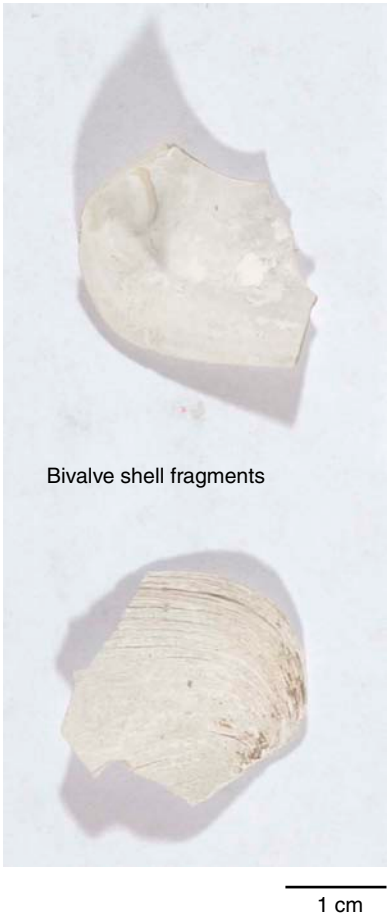

Figure F11. Unlithified carbonate cement and a lithified piece of carbonate composed of nonstoichiometric dolomite (46 mol% $MgCO_3$) within very dark gray sand and dark gray clay in lithostratigraphic Unit I (interval 311-U1326B-1H-1, 90–106 cm).

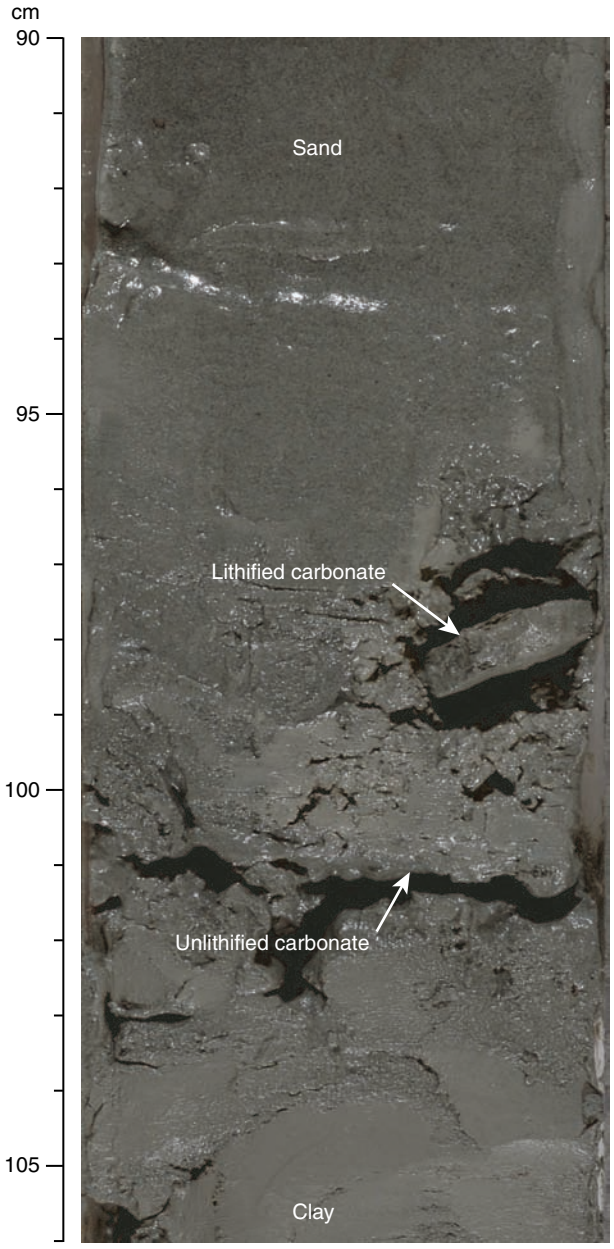

Figure F12. Unlithified microcrystalline carbonate cement in lithostratigraphic Unit I showing elongated crystals with lengths averaging 4–5 µm (Sample **311-U1326B-1H-1, 150 cm**).

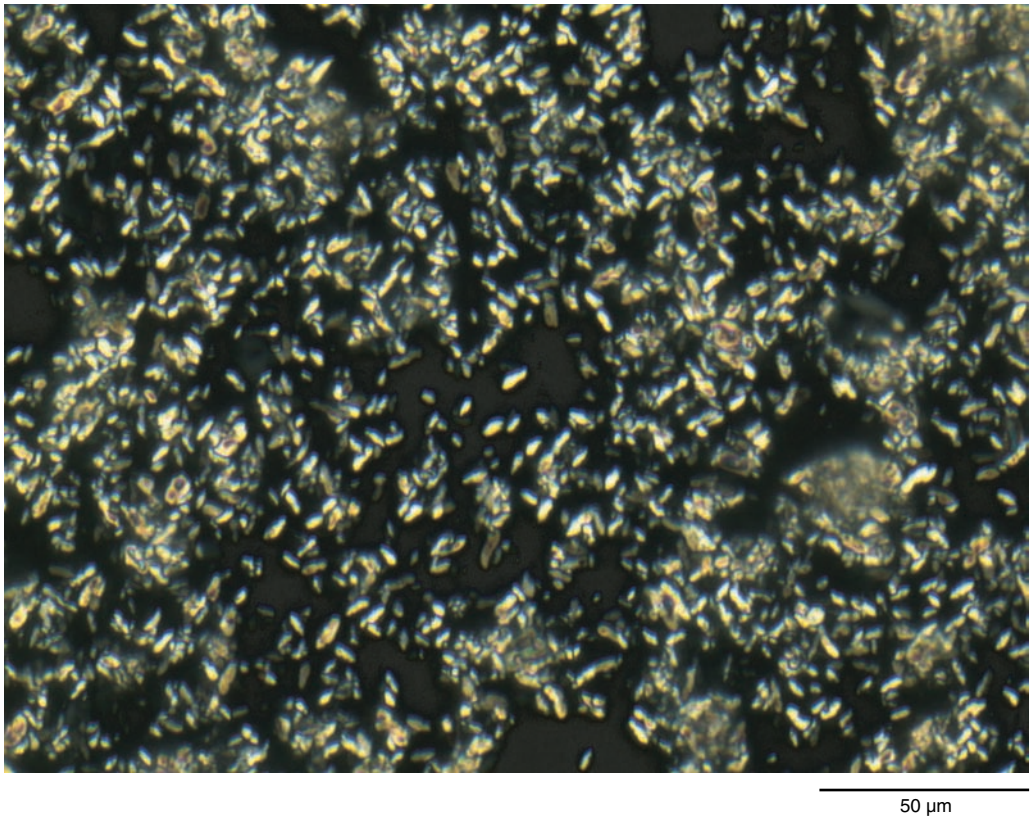

Figure F13. General occurrences of interbedded clay and silt (arrows) in lithostratigraphic Unit II (interval 311-U1326C-4H-3, 104–136 cm).

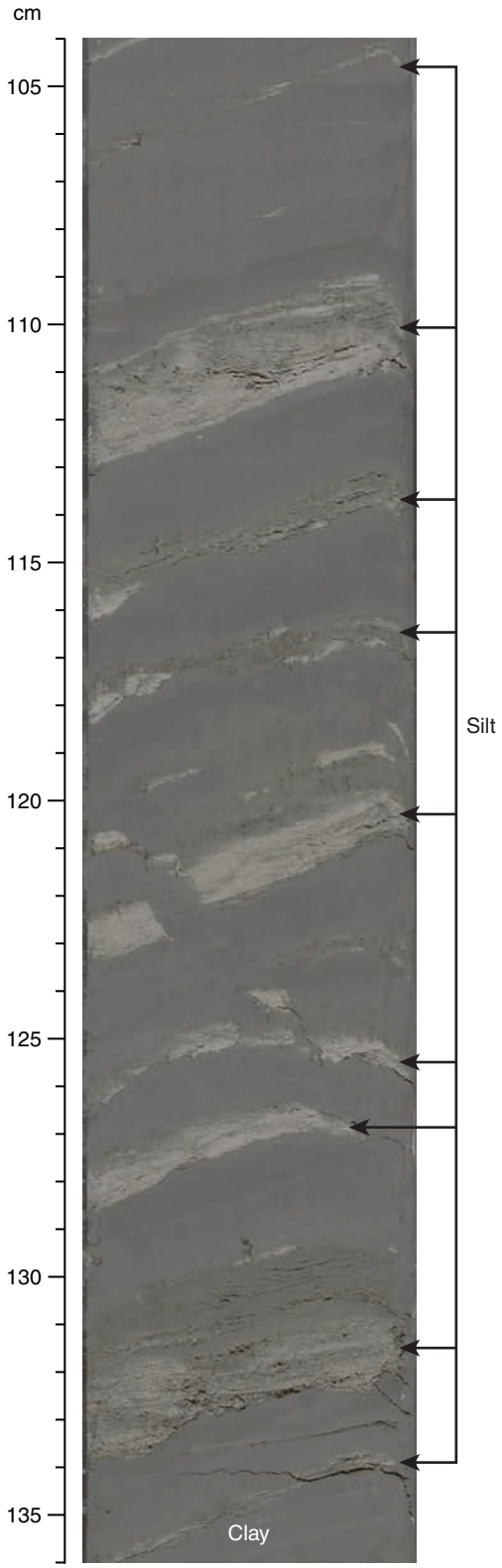

Figure F14. Dropstones and sand patches within dark gray clay in lithostratigraphic Unit II (interval 311-U1326D-4X-5, 22–46 cm).

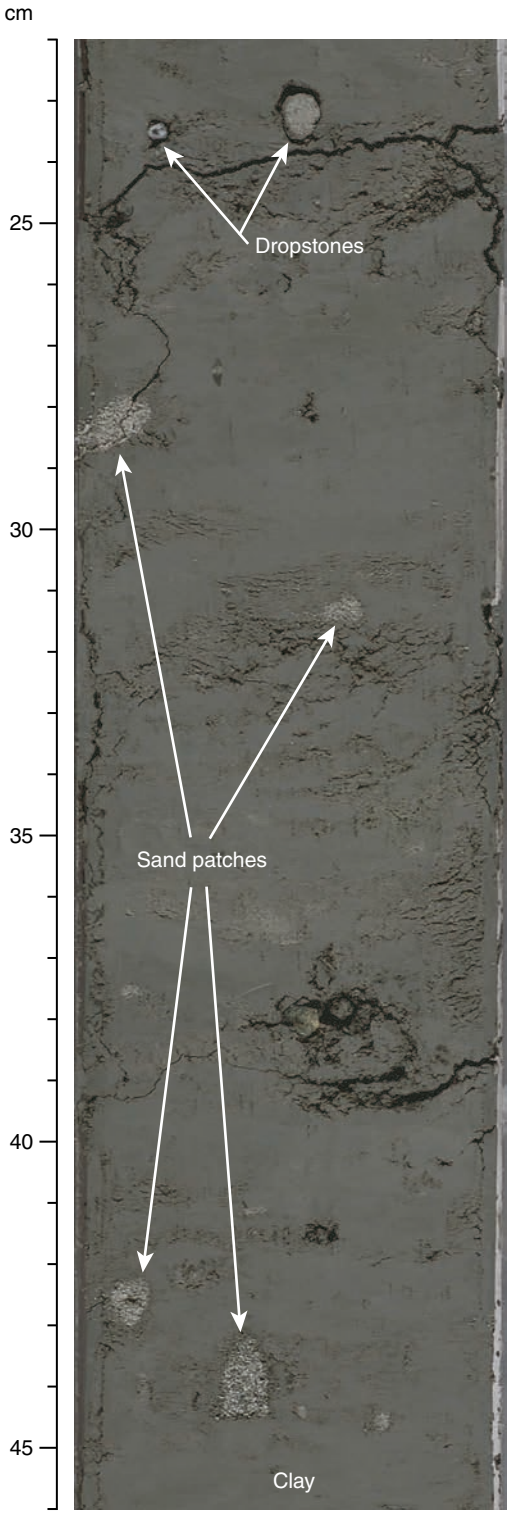

Figure F15. Unlithified carbonate cement within dark gray clay in lithostratigraphic Unit II (interval 311-U1326D-5X-2, 0–15 cm).

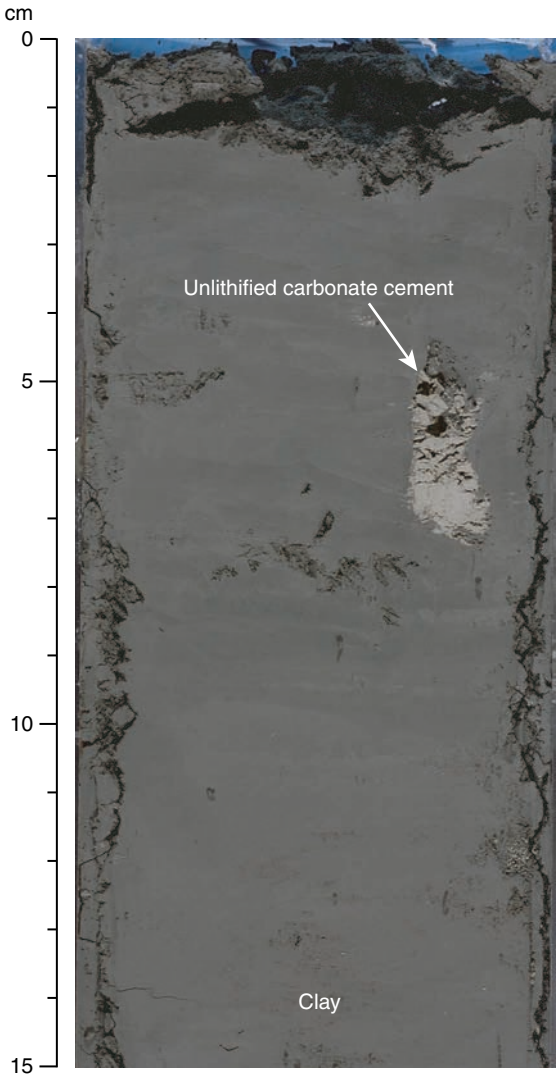

Figure F16. Soft-sediment deformation and a normal fault (arrows) cutting silt layers in lithostratigraphic Unit II (interval 311-U1326C-6X-5, 16–35 cm).

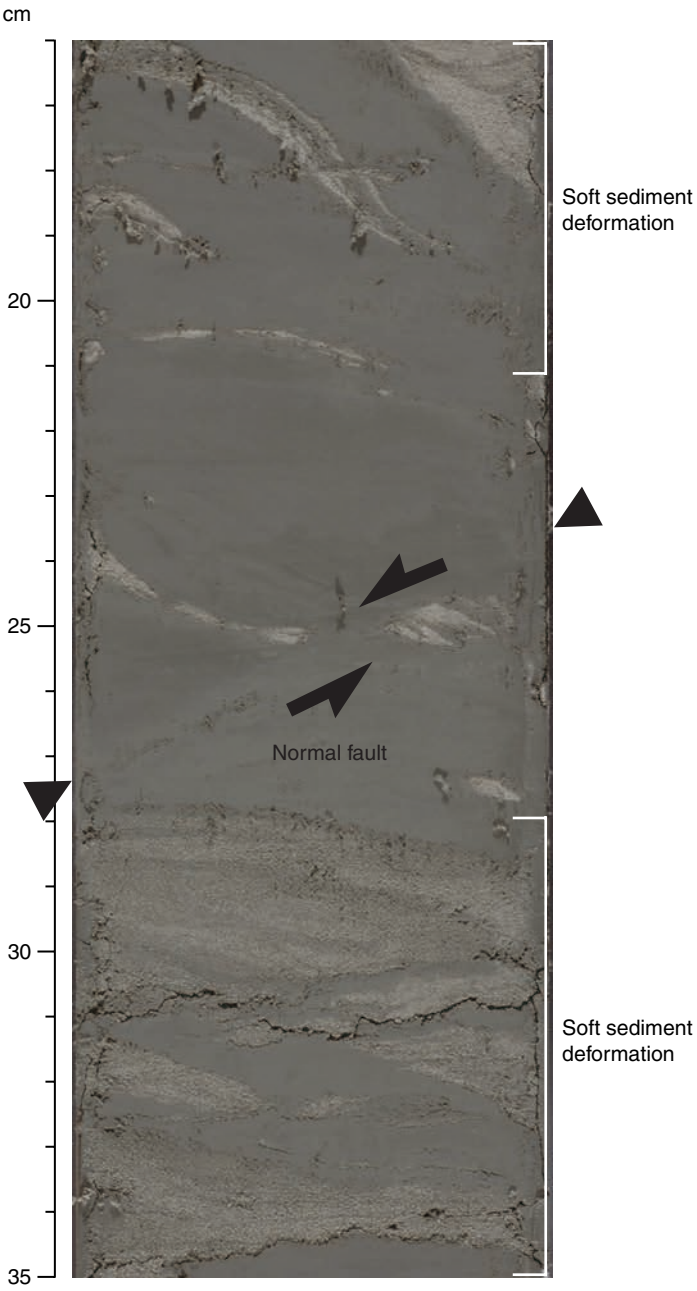

Figure F17. Thick, very dark gray sand layer within dark gray clay in lithostratigraphic Unit III (interval 311-U1326D-13X-3, 2–23 cm).

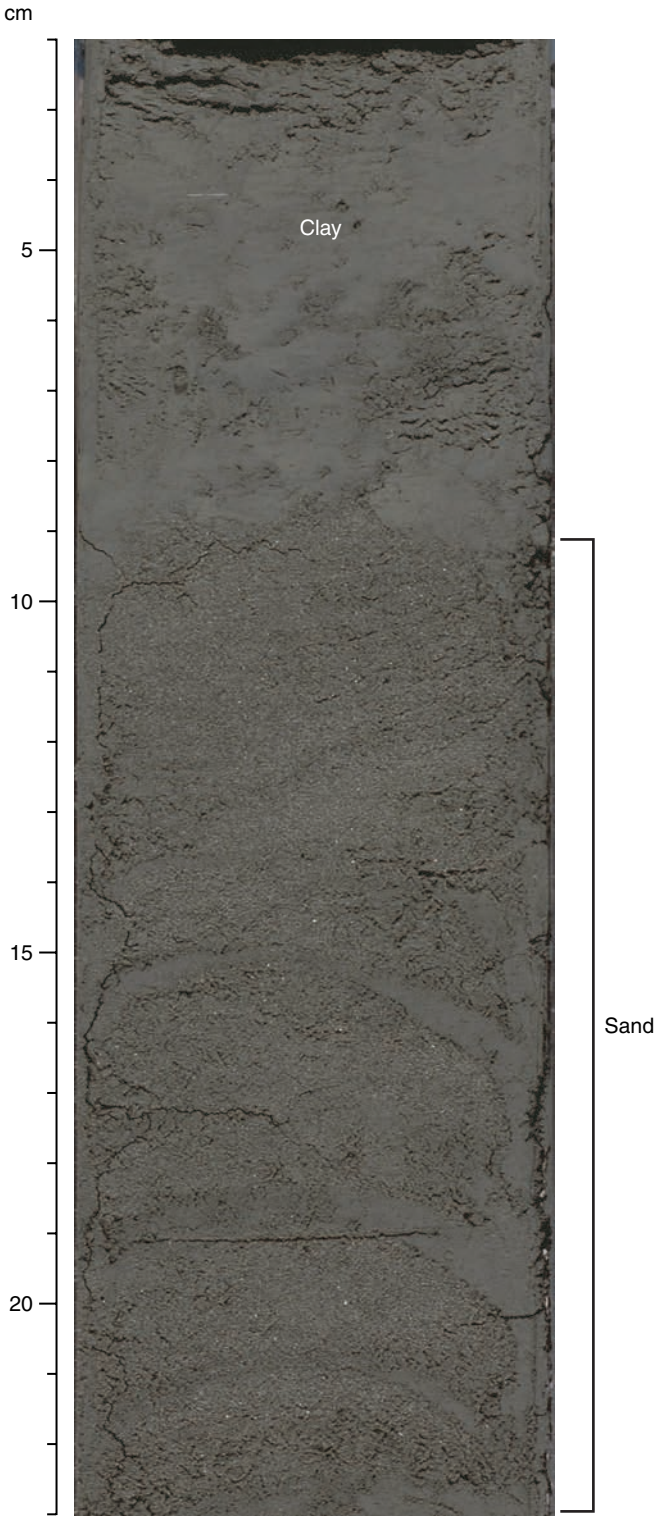

Figure F18. Partly lithified carbonates in silty clay with diatoms in lithostratigraphic Unit III (interval 311-U1326D-9X-1, 0–30 cm).

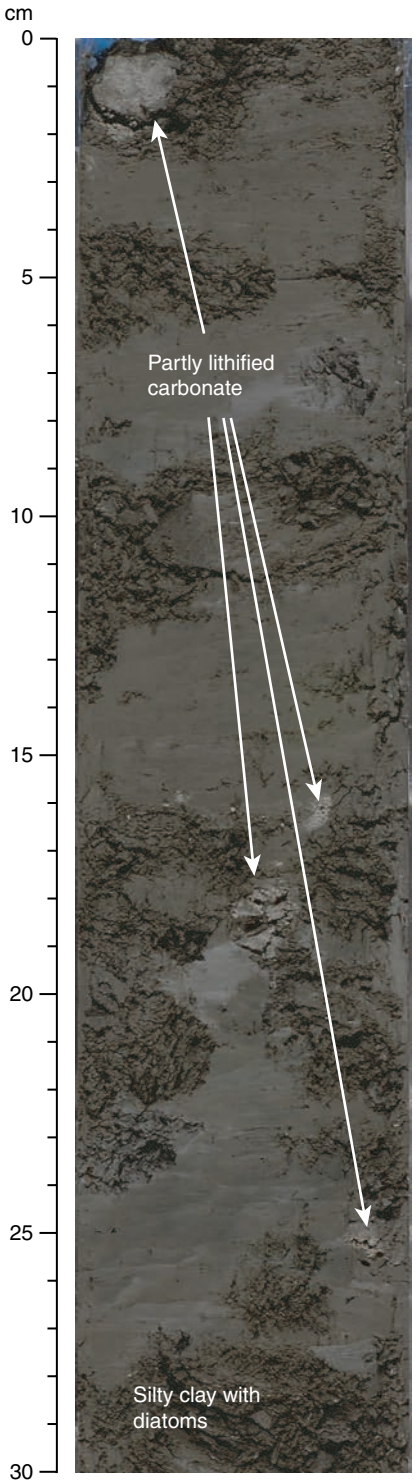

Figure F19. Soupy and mousselike sediment textures in lithostratigraphic Unit III (interval 311-U1326D-17X-1, 10–35 cm). Because the close-up photograph was taken one day after the core was split, the sediment has already dried significantly. The soupy texture between 18 and 26 cm is not clearly visible any more.

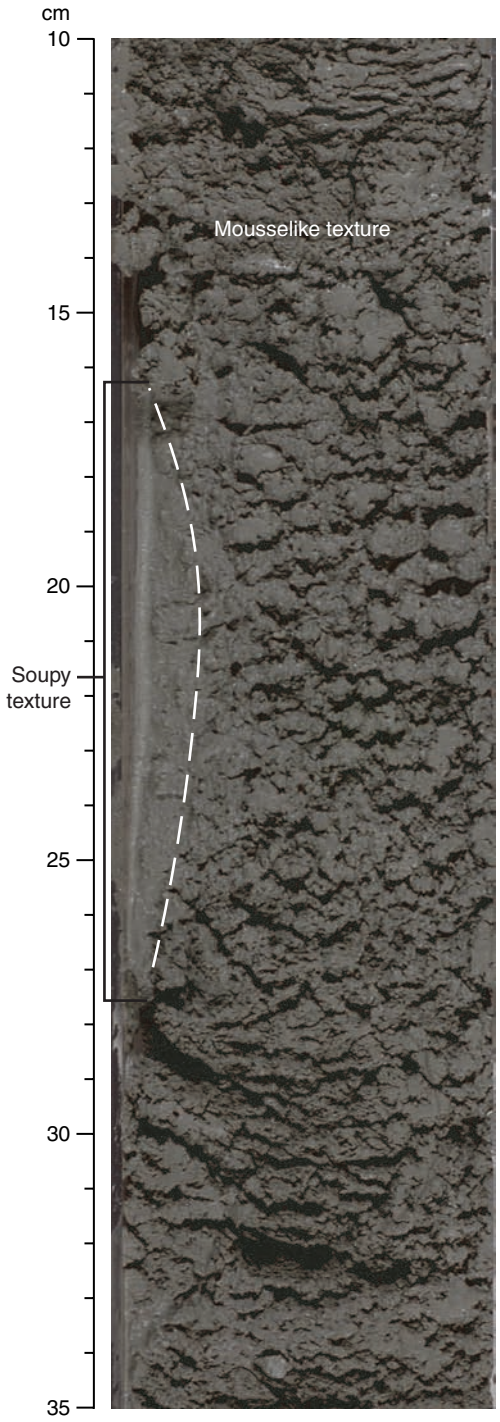

Figure F20. Mousselike sediment texture in lithostratigraphic Unit III (interval 311-U1326D-16X-3, 115–137 cm).

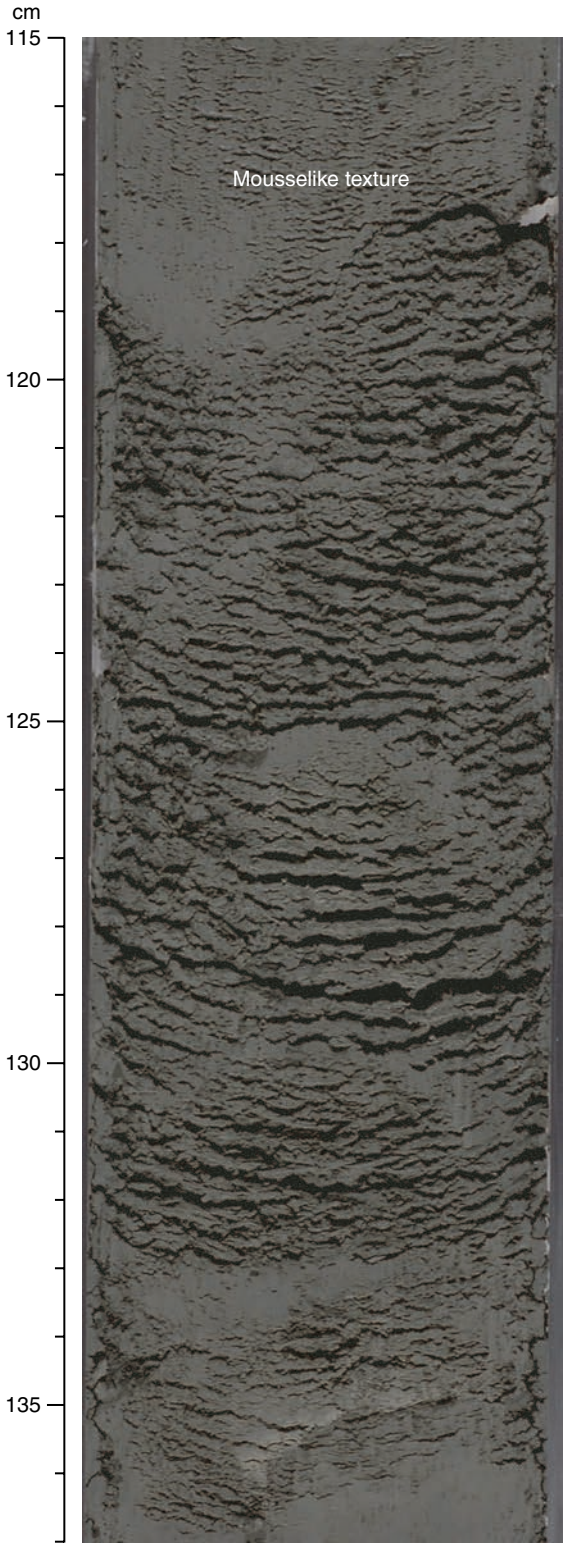

Figure F21. Concentration vs. depth profiles of salinity, chloride, sodium, and potassium in interstitial waters from Holes U1326C (red circles) and U1326D (green squares). SW = seawater, BSR = seismically inferred bottom-simulating reflector.

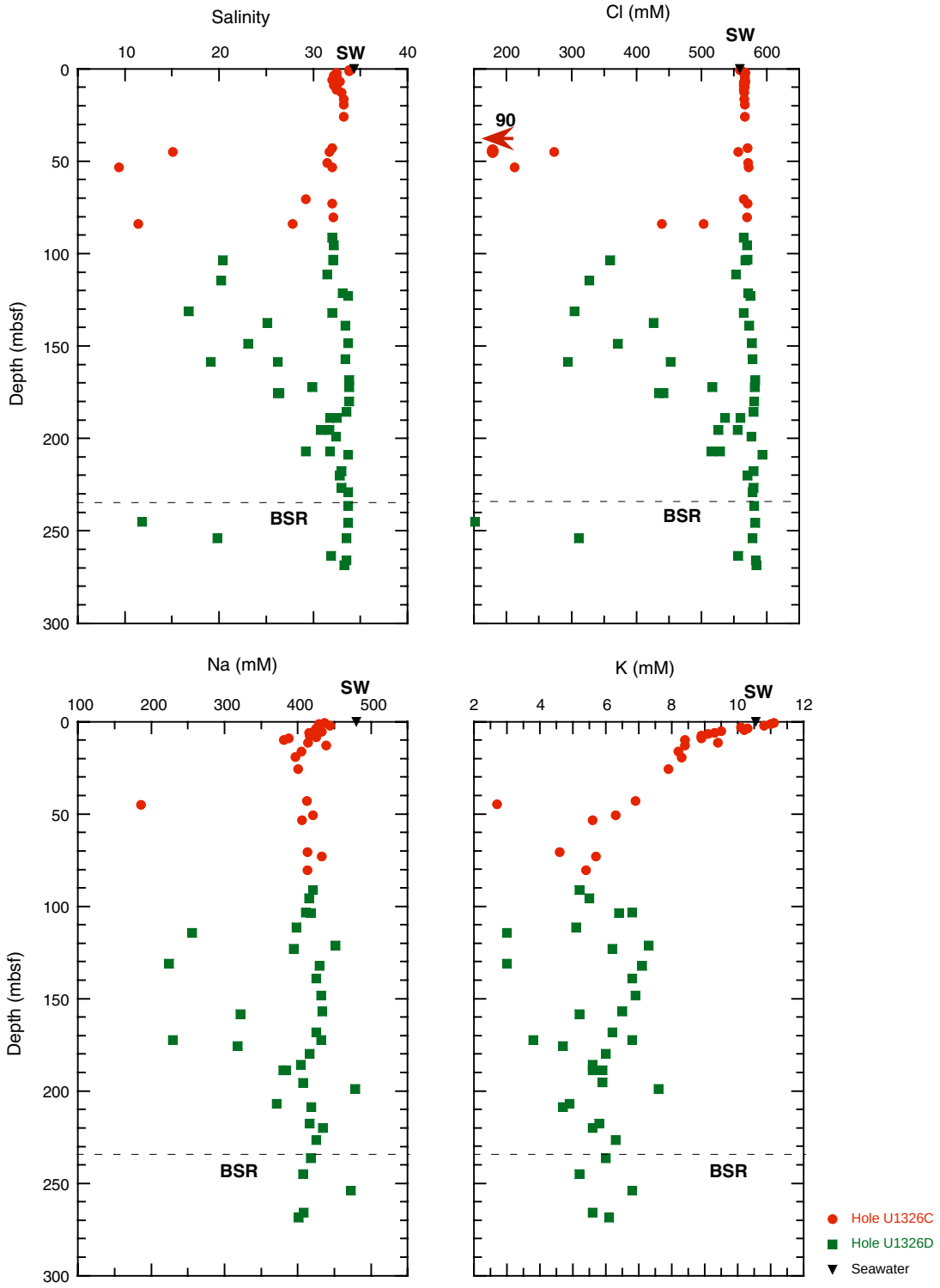

Figure F22. Concentration vs. depth profiles of alkalinity, sulfate, ammonium, and phosphate in interstitial waters from Holes U1326C (red circles) and U1326D (green squares). SW = seawater, BSR = seismically inferred bottom-simulating reflector.

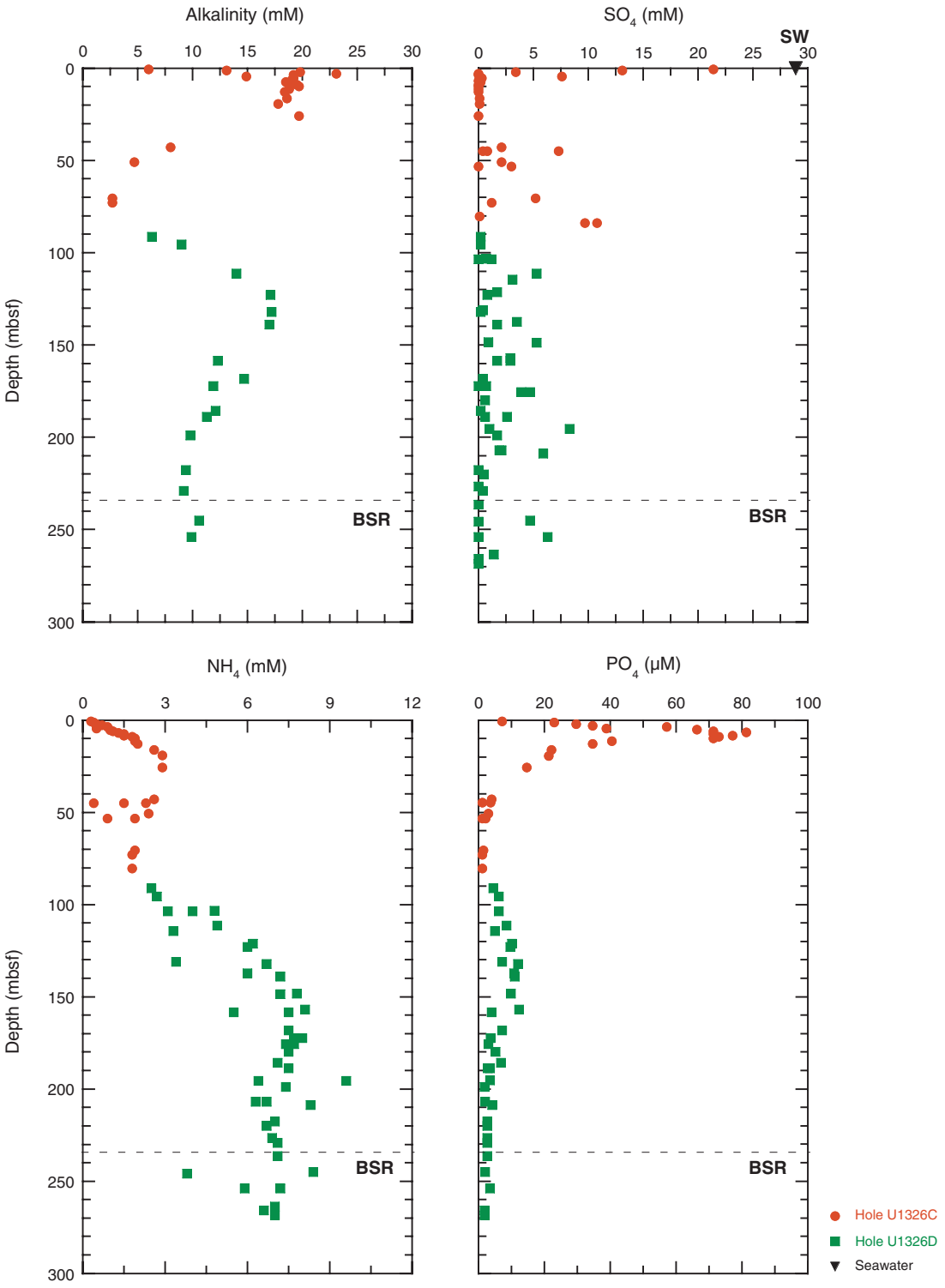

Figure F23. Concentration vs. depth profiles of calcium, magnesium, Mg/Ca ratios, and strontium in interstitial waters from Holes U1326C (red circles) and U1326D (green squares). SW = seawater, BSR = seismically inferred bottom-simulating reflector.

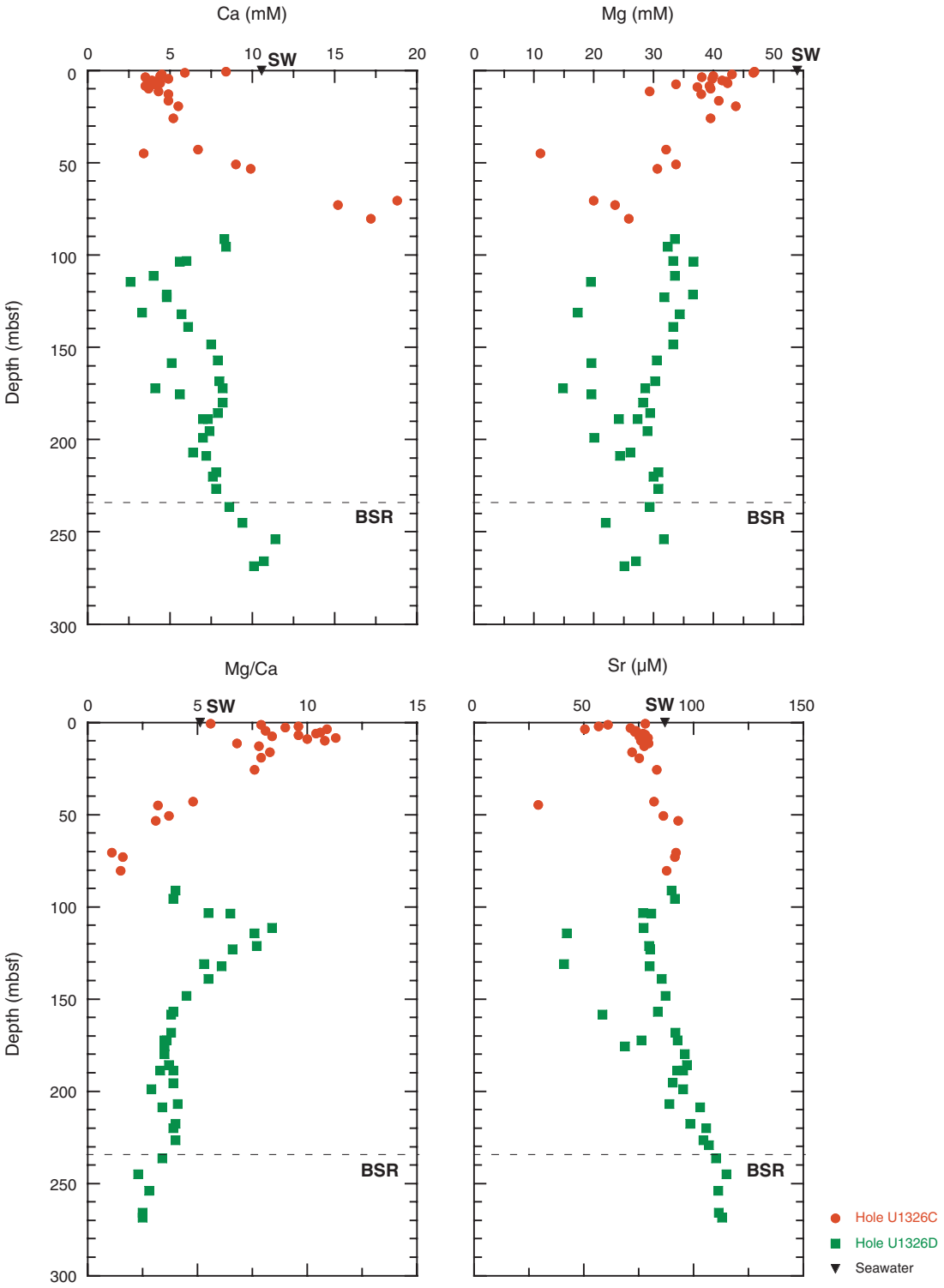

Figure F24. Concentration vs. depth profiles of lithium, boron, silica, and barium in interstitial waters from Holes U1326C (red circles) and U1326D (green squares). SW = seawater, BSR = seismically inferred bottom-simulating reflector.

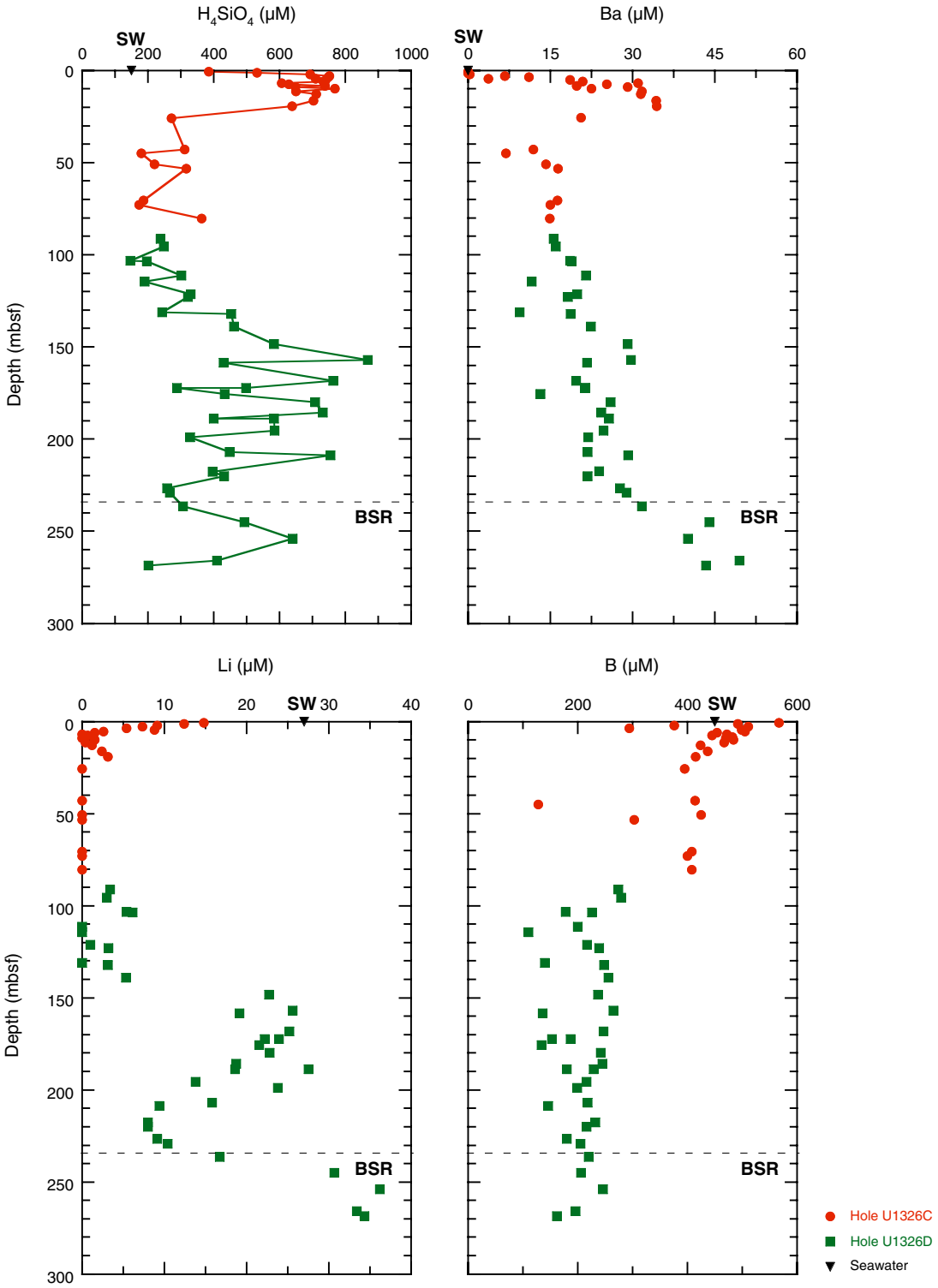

Figure F25. Concentrations of methane and ethane in headspace gas samples from Site U1326. BSR = bottom-simulating reflector.

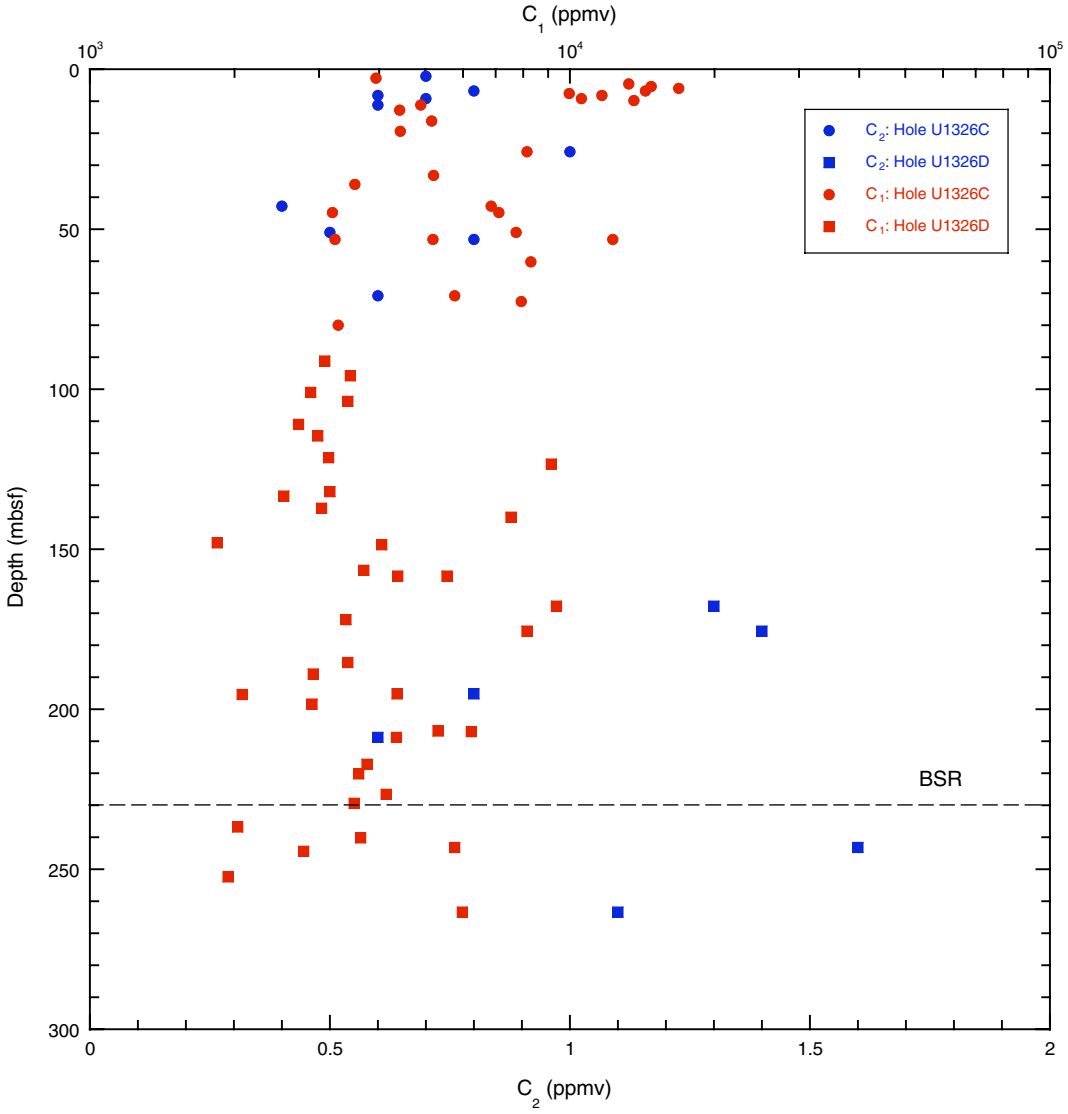

Figure F26. Concentrations of ethane, propane, *i*-butane, and *n*-butane in void gas samples from Site U1326. BSR = bottom-simulating reflector.

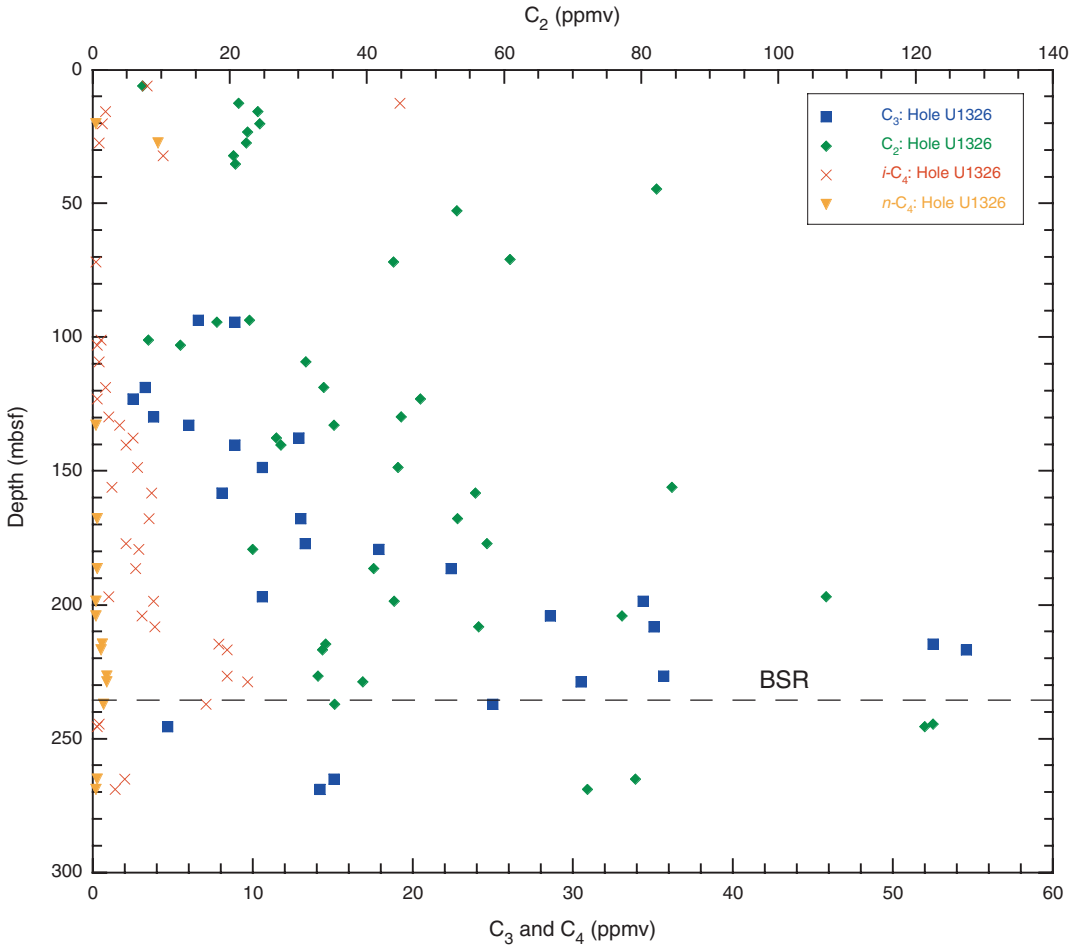

Figure F27. C_1/C_2 and *i*-C_4/*n*-C_4 ratios in void gas, gas hydrate (HYD), and PCS gas samples from Site U1326. BSR = bottom-simulating reflector, HYD = gas hydrate, PCS = Pressure Core Sampler.

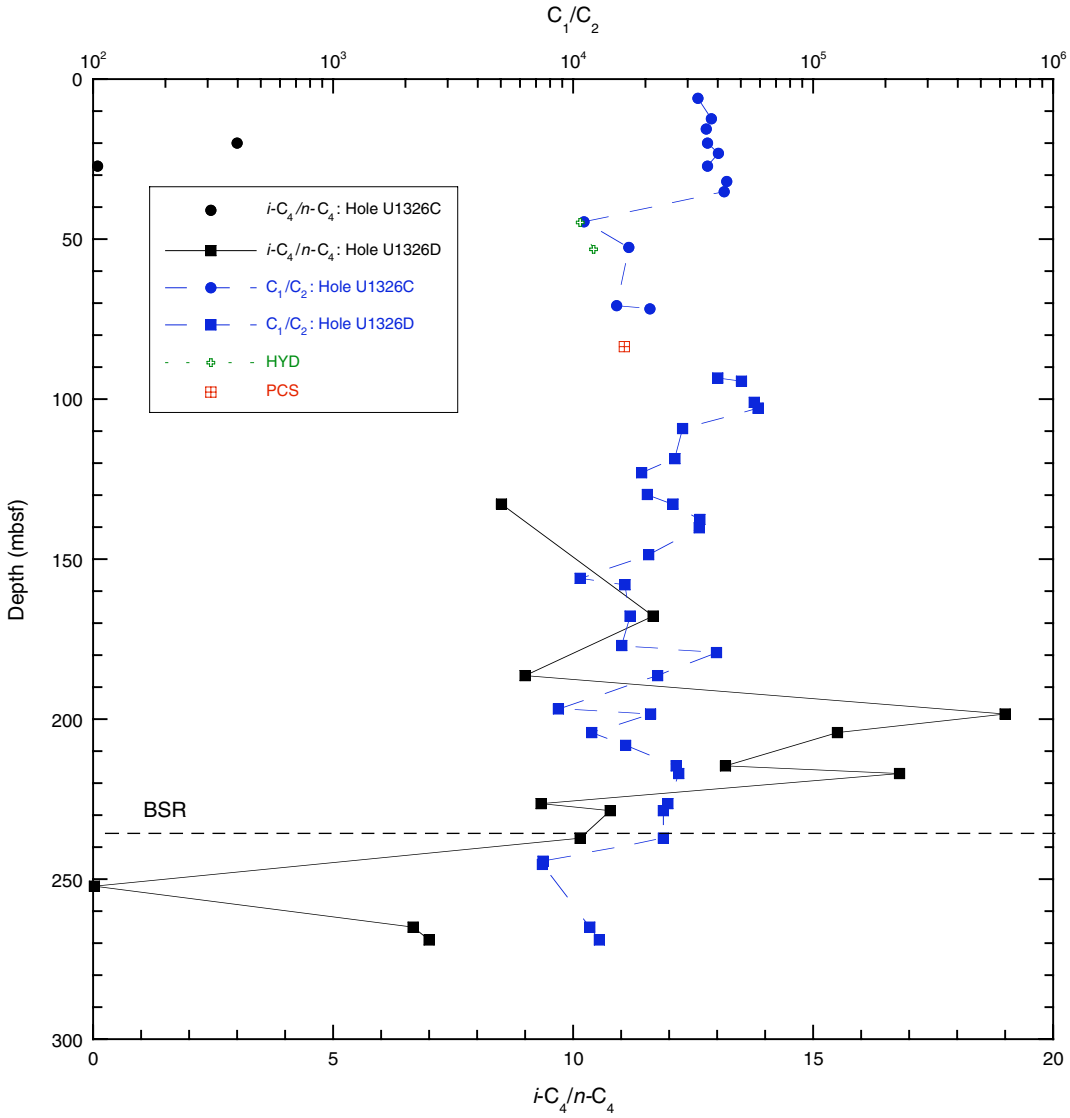

Figure F28. C_1/C_2 ratios vs. temperature at Site U1326. VAC = void gas, HS = headspace gas.

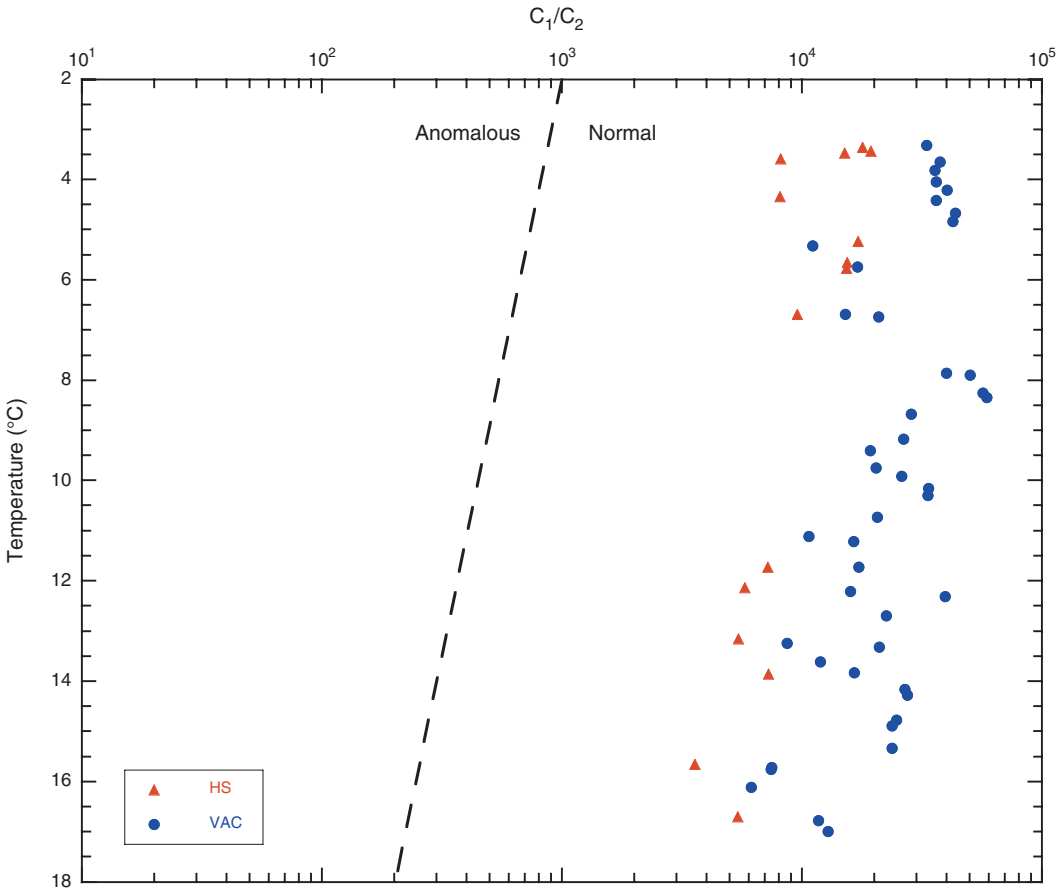

Figure F29. Dissolved sulfate and methane concentrations from Site U1326.

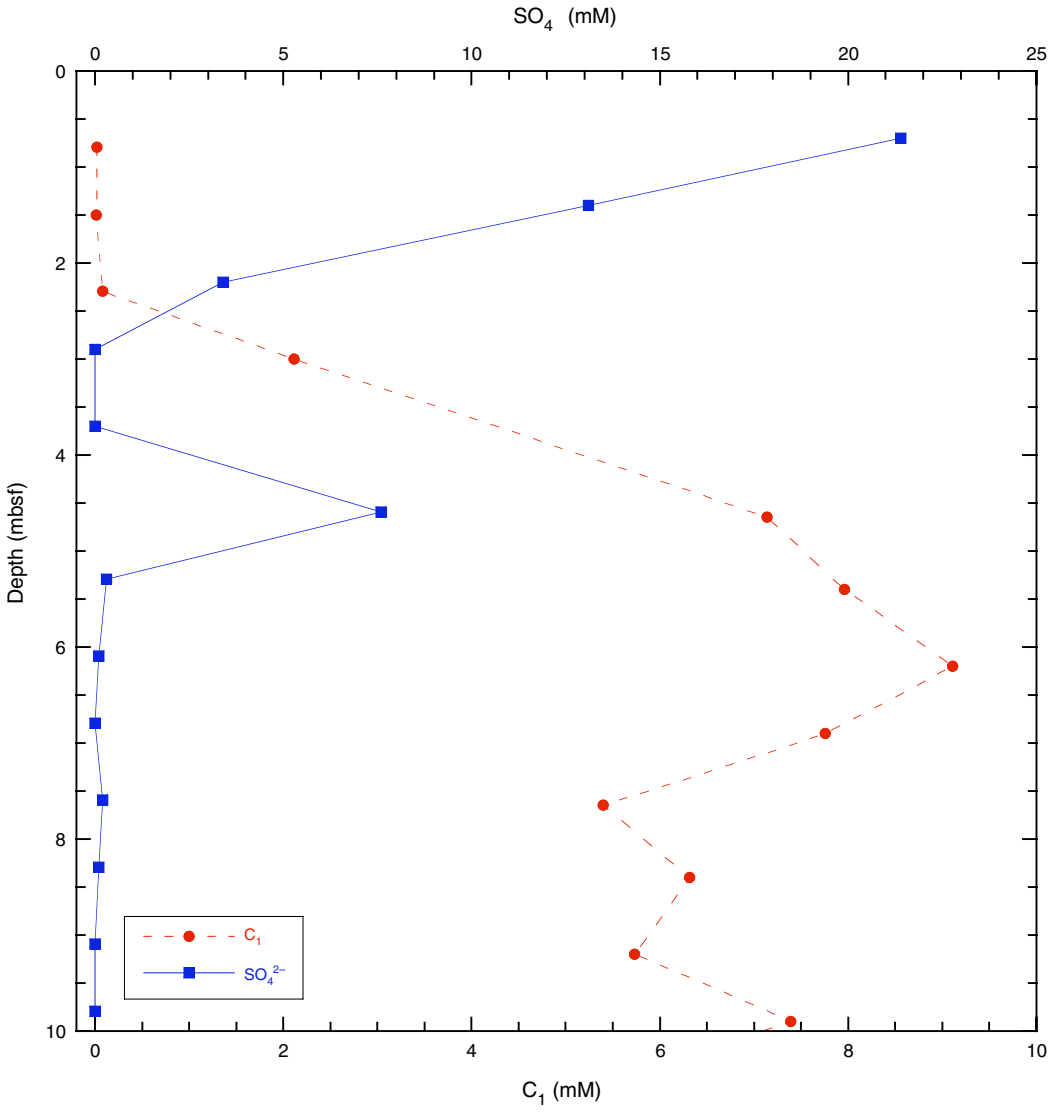

Figure F30. Concentrations of inorganic carbon (IC), calcium carbonate ($CaCO_3$), total organic carbon (TOC), total nitrogen (TN), and C/N ratios in sediments from Site U1326. Data are plotted on different depth scales to highlight the overall site (0–200 mbsf) and near-surface (0–13 mbsf) trends. Dashed lines = lithostratigraphic unit boundaries.

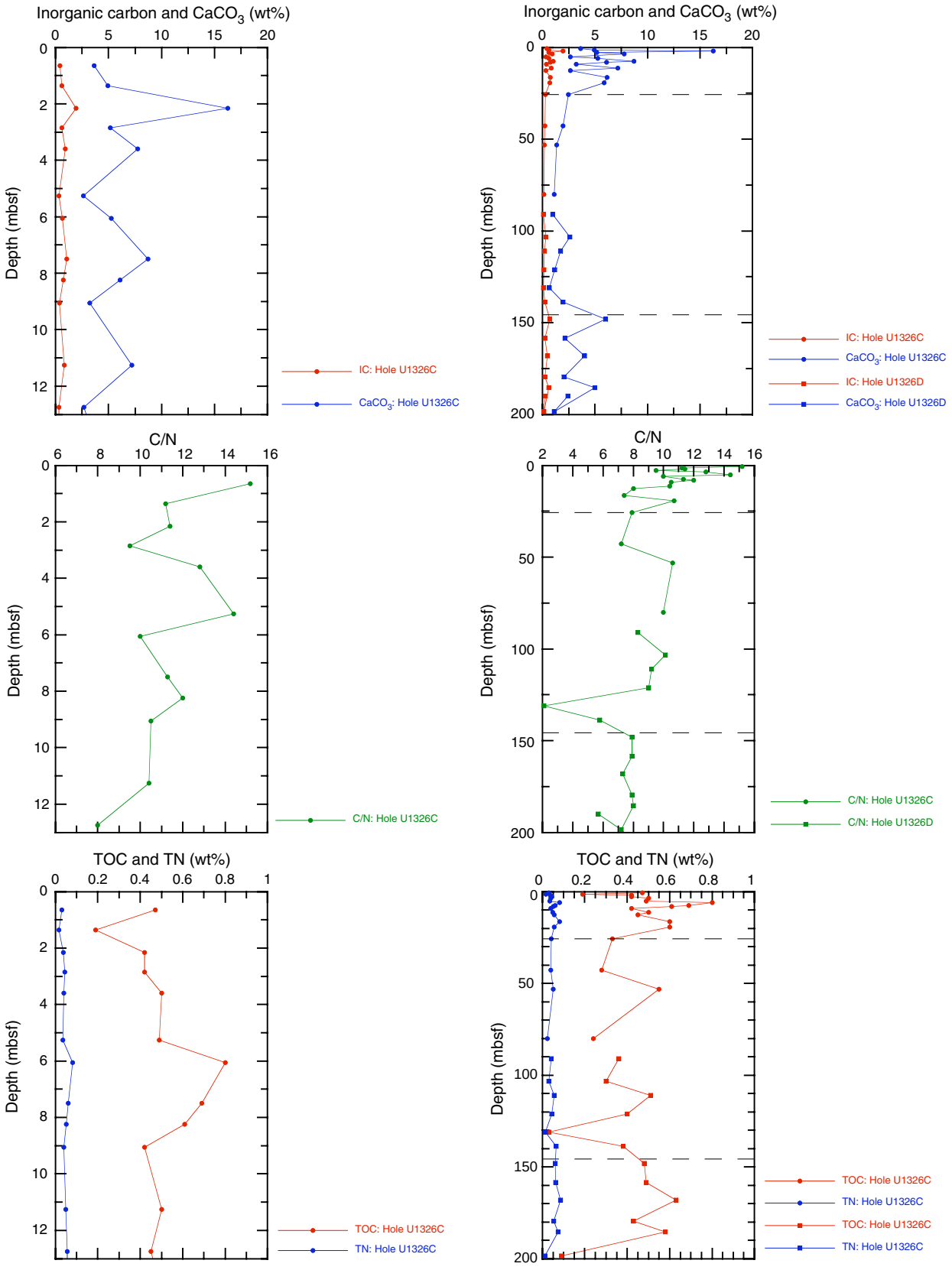

Figure F31. Overview of physical property data from Site U1326. Plotted from left to right are core recovery; logging-while-drilling (LWD) and moisture and density (MAD) porosity; LWD, multisensor track (MST), and MAD bulk density; MAD grain density; LWD, MST contact, and MST noncontact resistivity; MST magnetic susceptibility; thermal conductivity (line shows regional trend from Davis et al., 1990); Torvane and automated vane shear (AVS) strength; and lithostratigraphic units. BSR = bottom-simulating reflector.

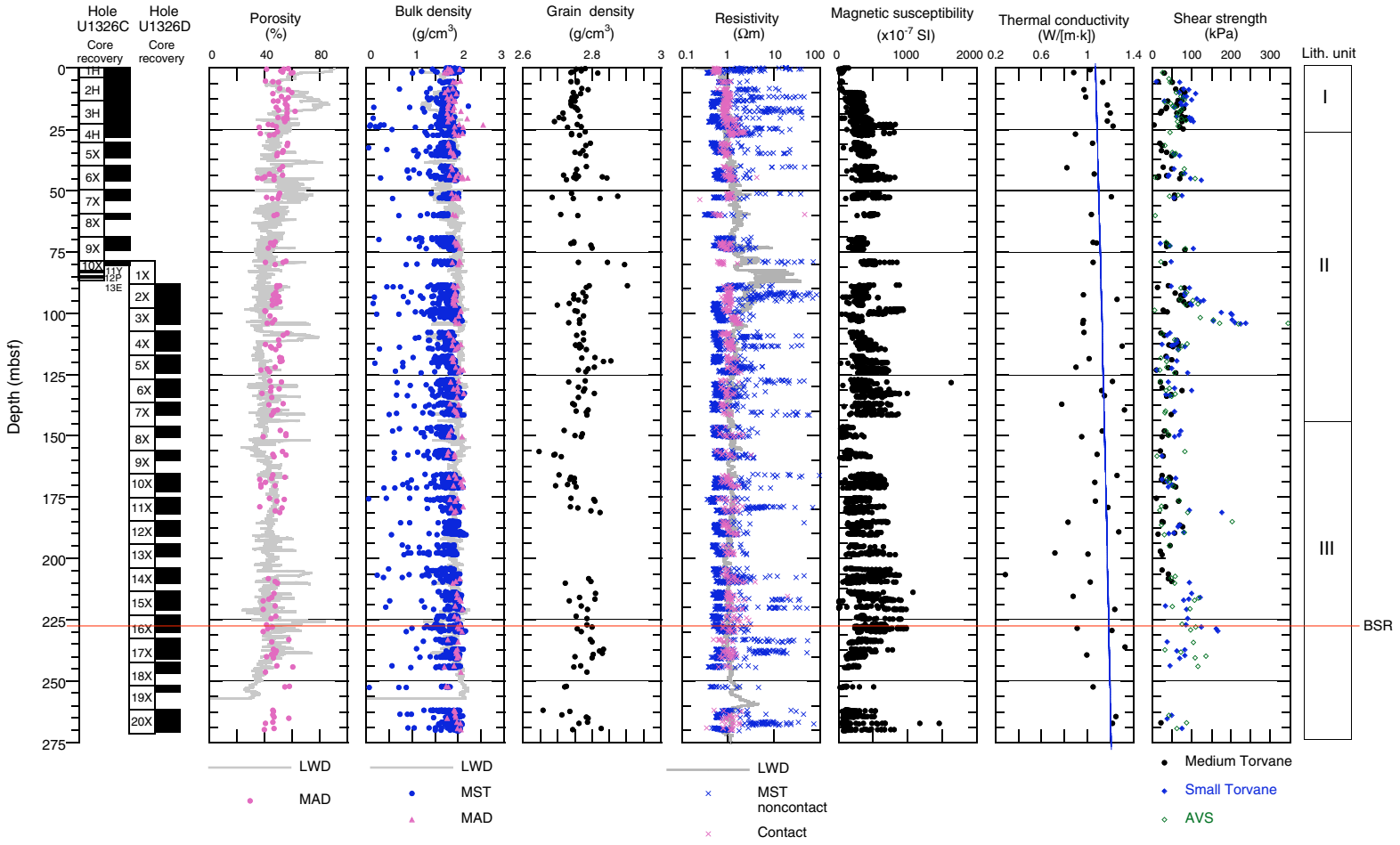

Figure F32. Combined infrared (IR) images of core liner temperature from Holes U1326C and U1326D compared to logging-while-drilling/measurement-while-drilling (LWD/MWD) resistivity and calculated pore water saturation from Hole U1326A. Core recovery and core handling time are also shown. BSR = bottom-simulating reflector. (This figure is also available in an **oversized format.**)

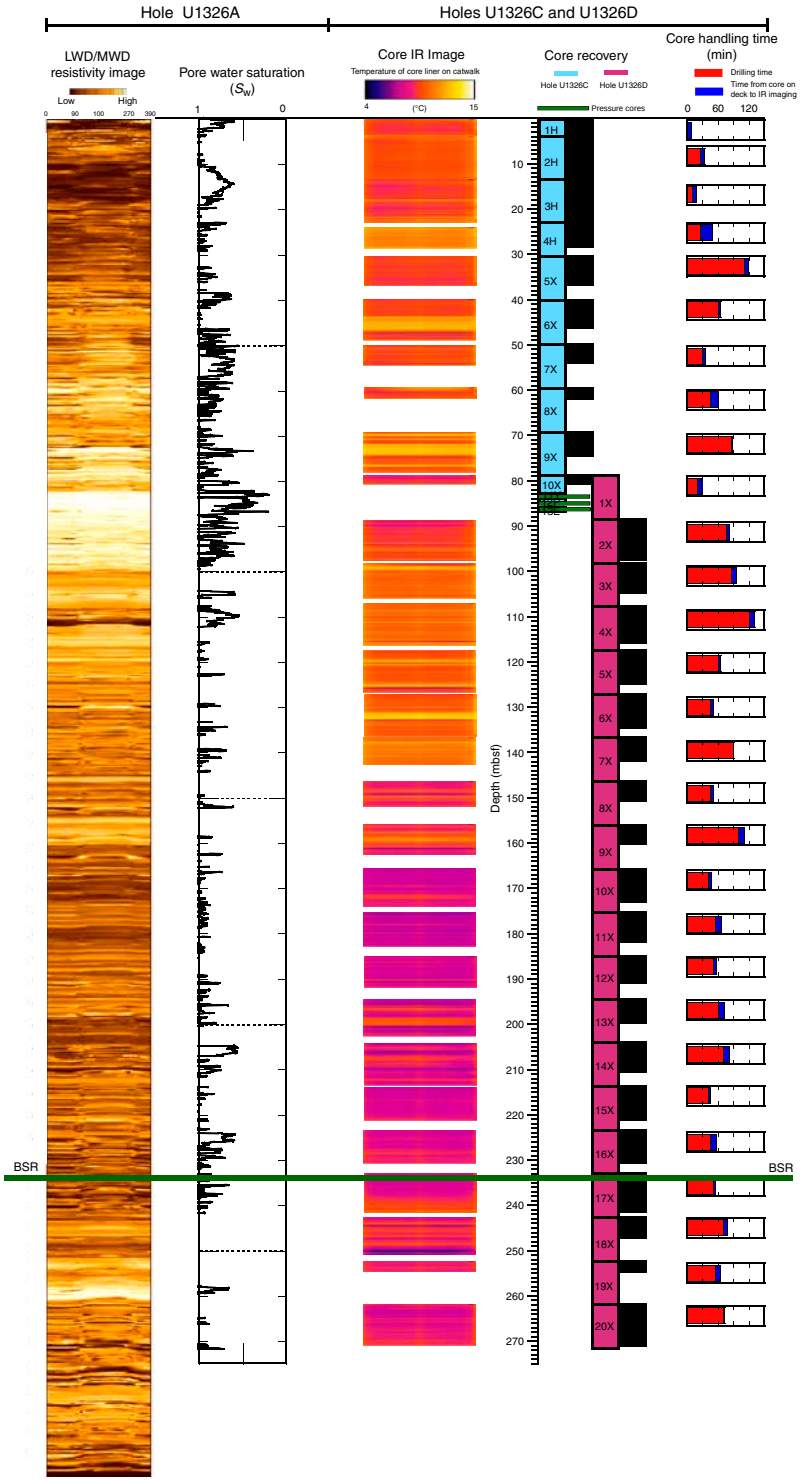

Figure F33. A. Downhole temperatures based on concatenation of core liner temperatures averaged across each pixel row (see text for details). **B.** Detail of the temperature profile for 240–255 mbsf. Note the numerous, strong cold temperature anomalies. **C.** Infrared (IR) image of Core 311-U1326D-18X. **D.** Section 311-U1326D-18X-4 showing "foamy" sediment. The liner was split to expose the whole-round core. Note the shrinkage of the core. This sediment was unusually dry and full of tiny gas bubbles.

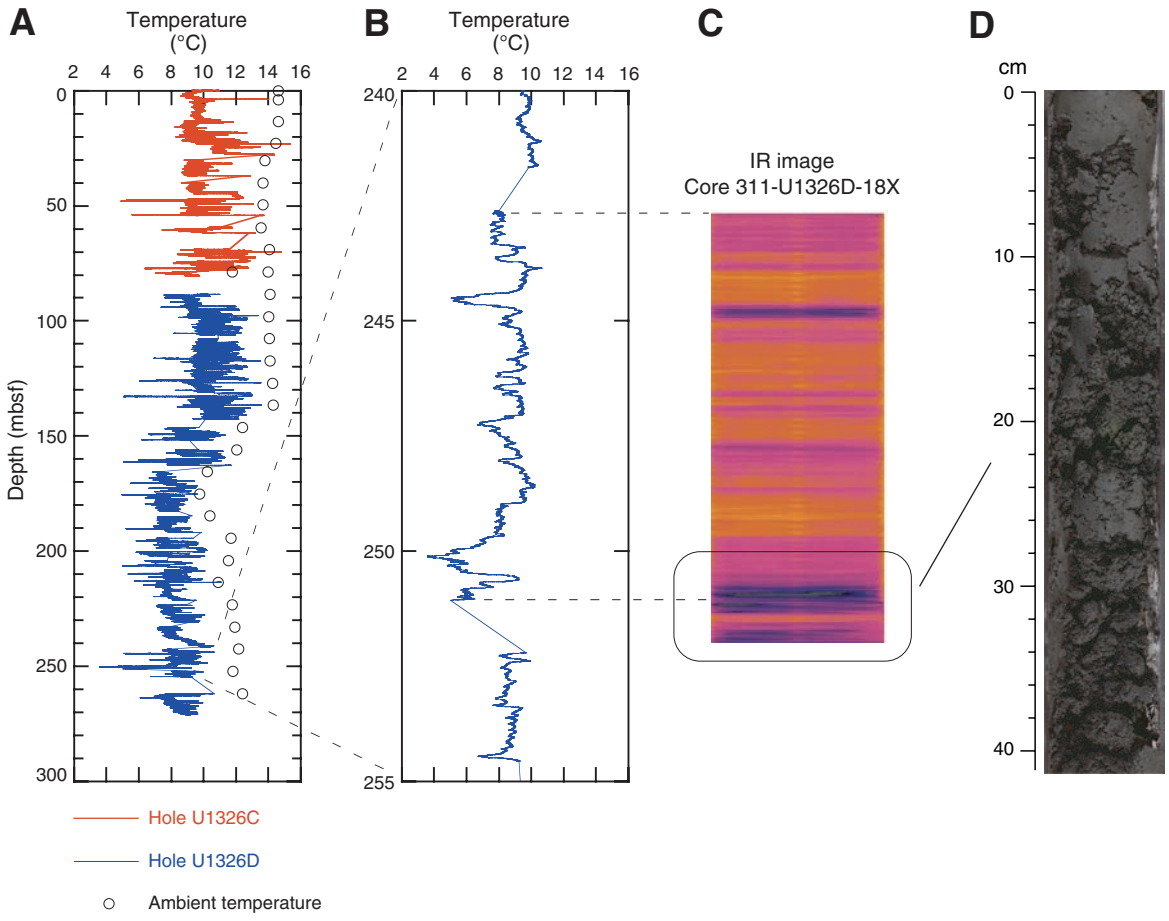

Figure F34. Catwalk temperature and light intensity recorded during Expedition 311. Measurements were made 2.35 m from the core 0 point (end of catwalk closest to rig floor). Diurnal temperature changes that were characteristic of the early days of the expedition, when days were bright and sunny, were muted during the latter part of the expedition. Note the large, abrupt change in temperature that occurred during coring at Site U1326. Times (open symbols) of collecting individual cores are shown at the top of the figure for all sites. Each symbol corresponds to a single core. GMT = Greenwich Mean Time.

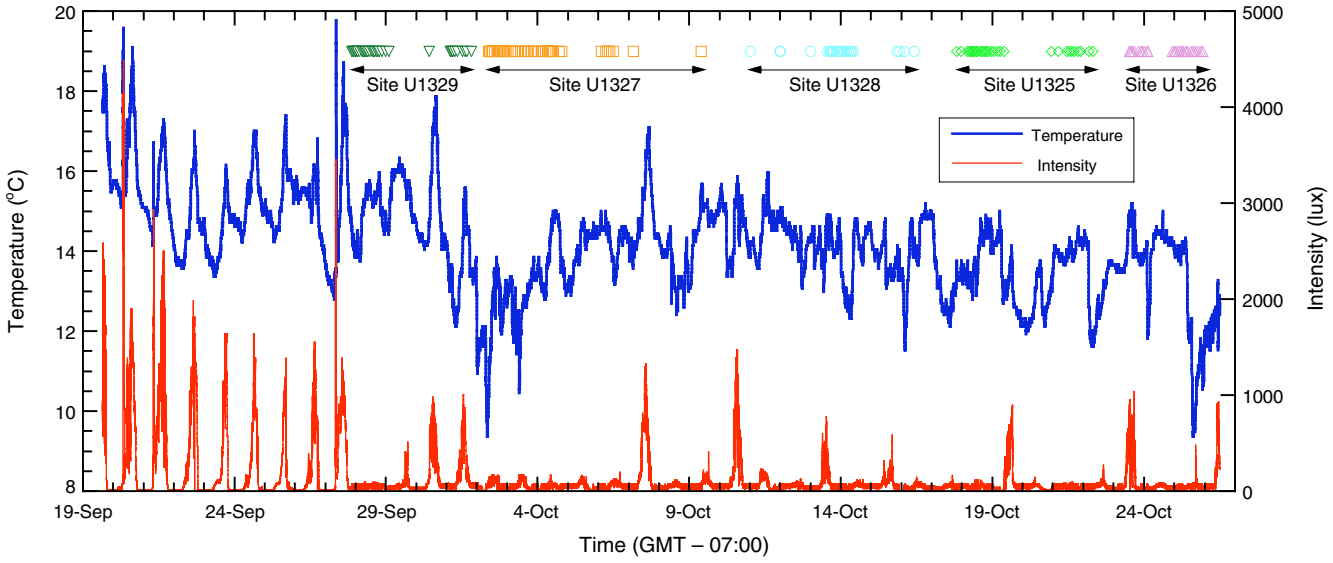

Figure F35. A. Sample of a sand layer containing gas hydrate in Sample 311-U1326C-6X-4, 83–96 cm. **B.** IR image of the same sample. **C.** Temperature profile along the IR image green line shown in B.

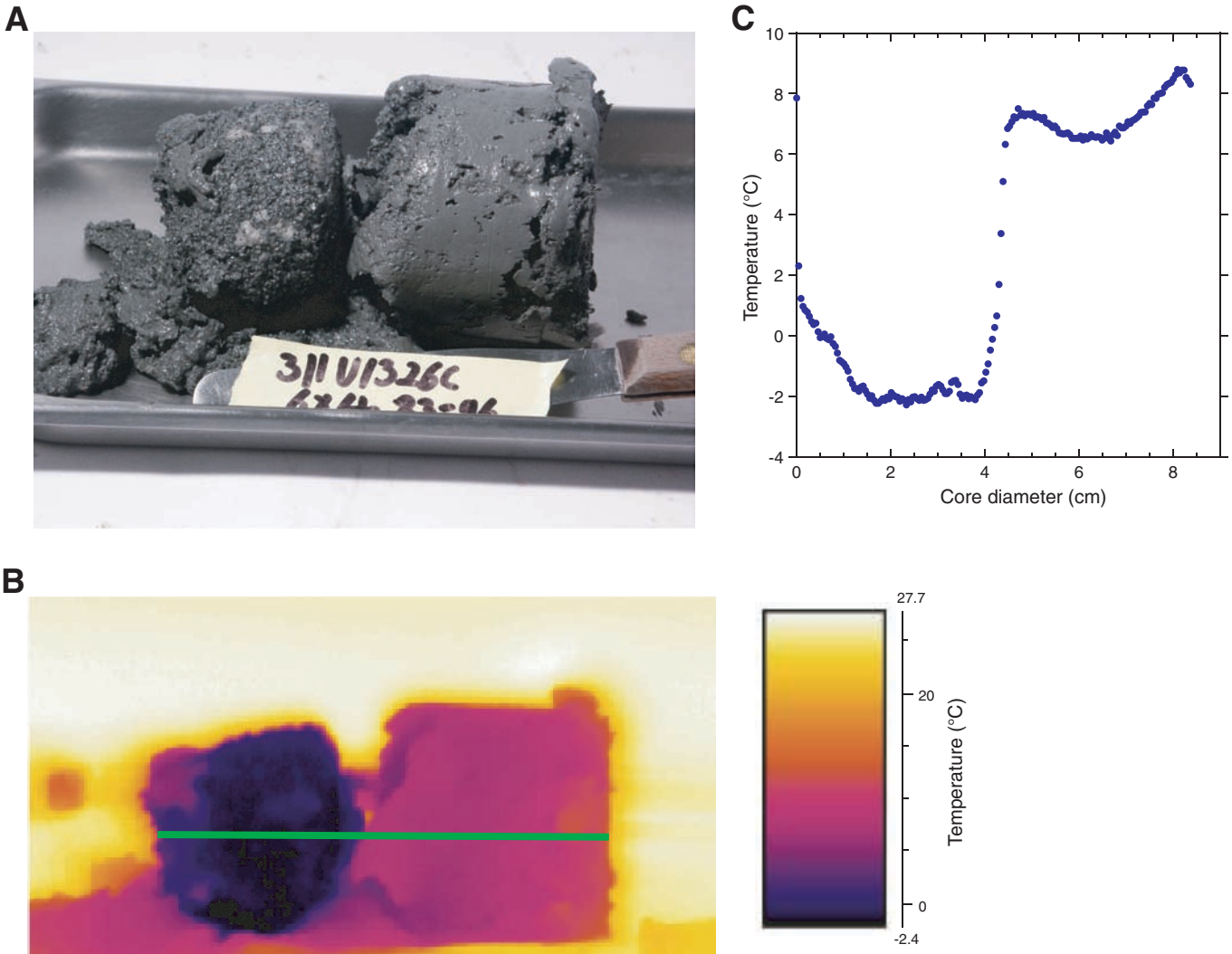

Figure F36. *P*-wave velocity measurements made using the multisensor track (MST) and Hamilton frame at Site U1326 compared to velocities from Site U1325. PWS = *P*-wave sensor.

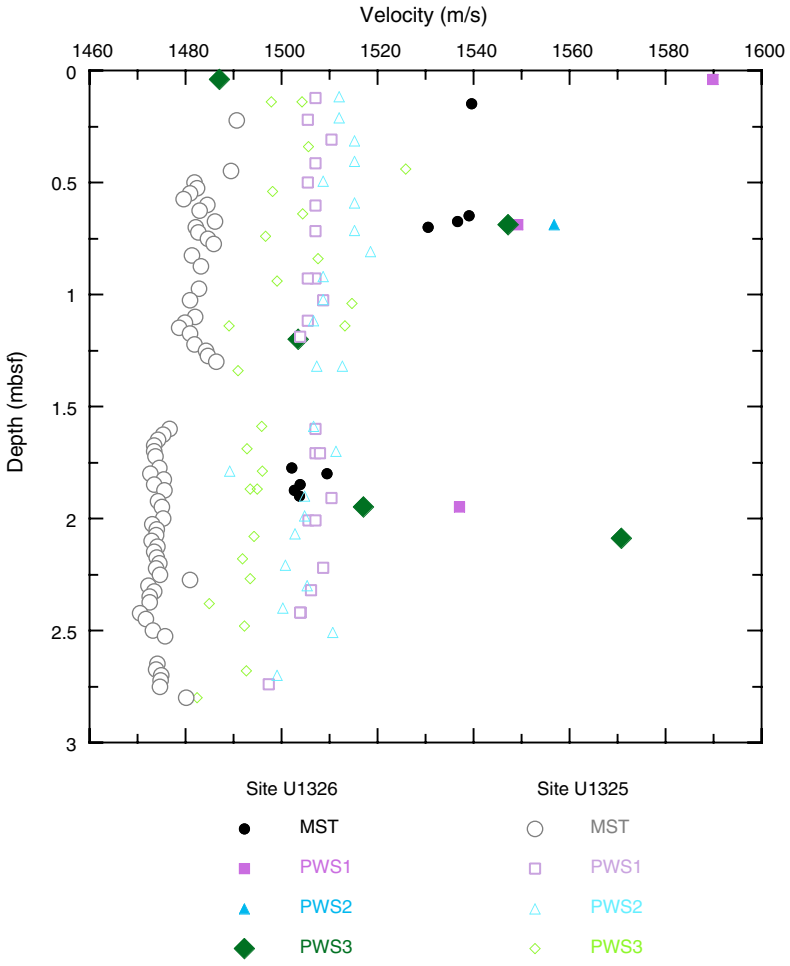

Figure F37. A. Comparison between automated vane shear (AVS) and handheld Torvane shear strength measurements from Site U1326. **B.** Overburden pressure calculated from MAD bulk density data. **C.** Ratio of shear strength to overburden pressure. This provides information on the degree of sediment underconsolidation or overconsolidation.

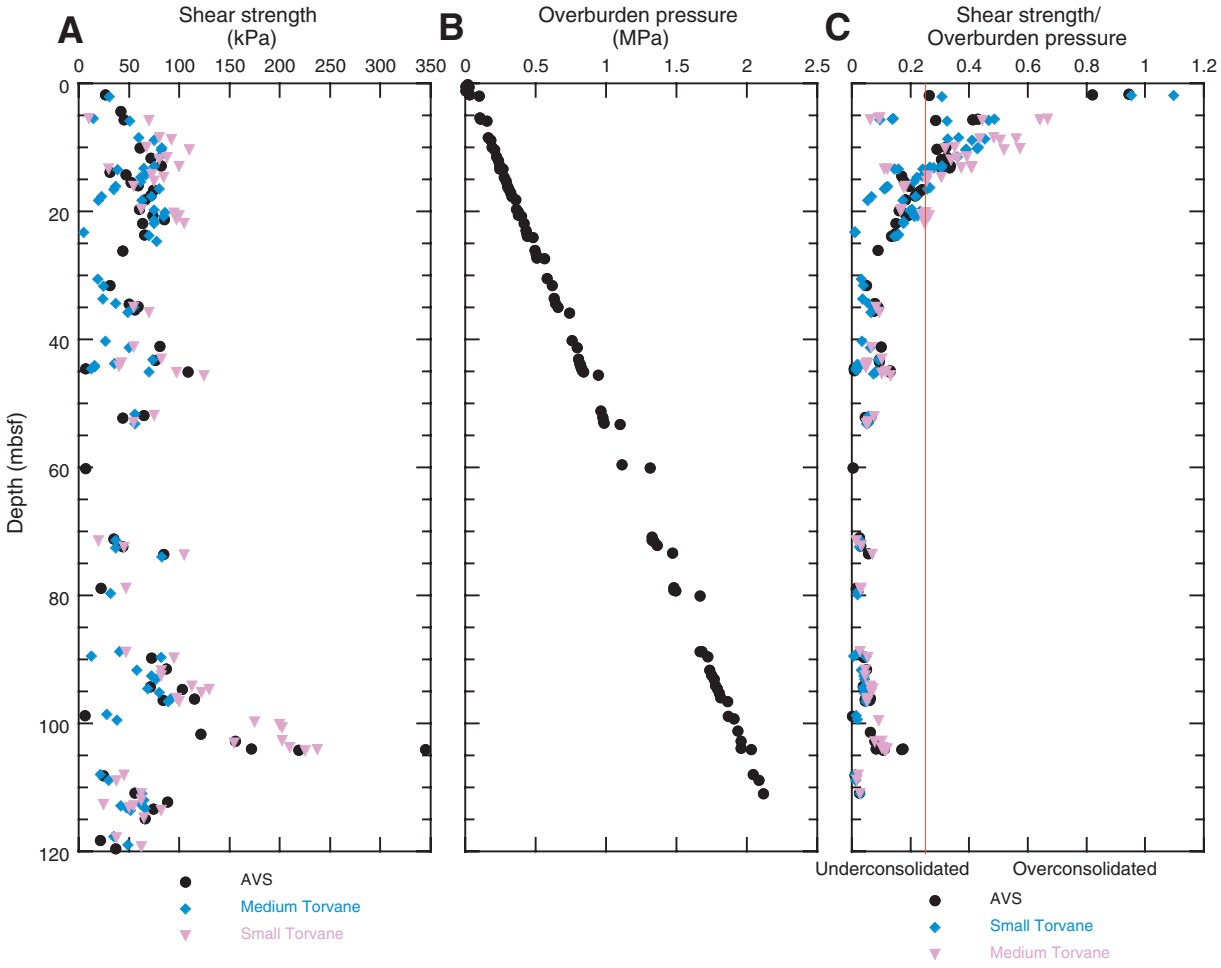

Figure F38. A. Comparison of pore water resistivity calculated from interstitial water salinity using equations developed by Fofonoff (1985) and bulk volume contact resistivity of sediments from Site U1326. Both sets of values have been corrected to 20°C. **B.** Formation factor (ratio of pore water resistivity to sediment resistivity). **C.** Comparison of porosity derived from moisture and density (MAD) measurements and Archie's equation. (Continued on next page).

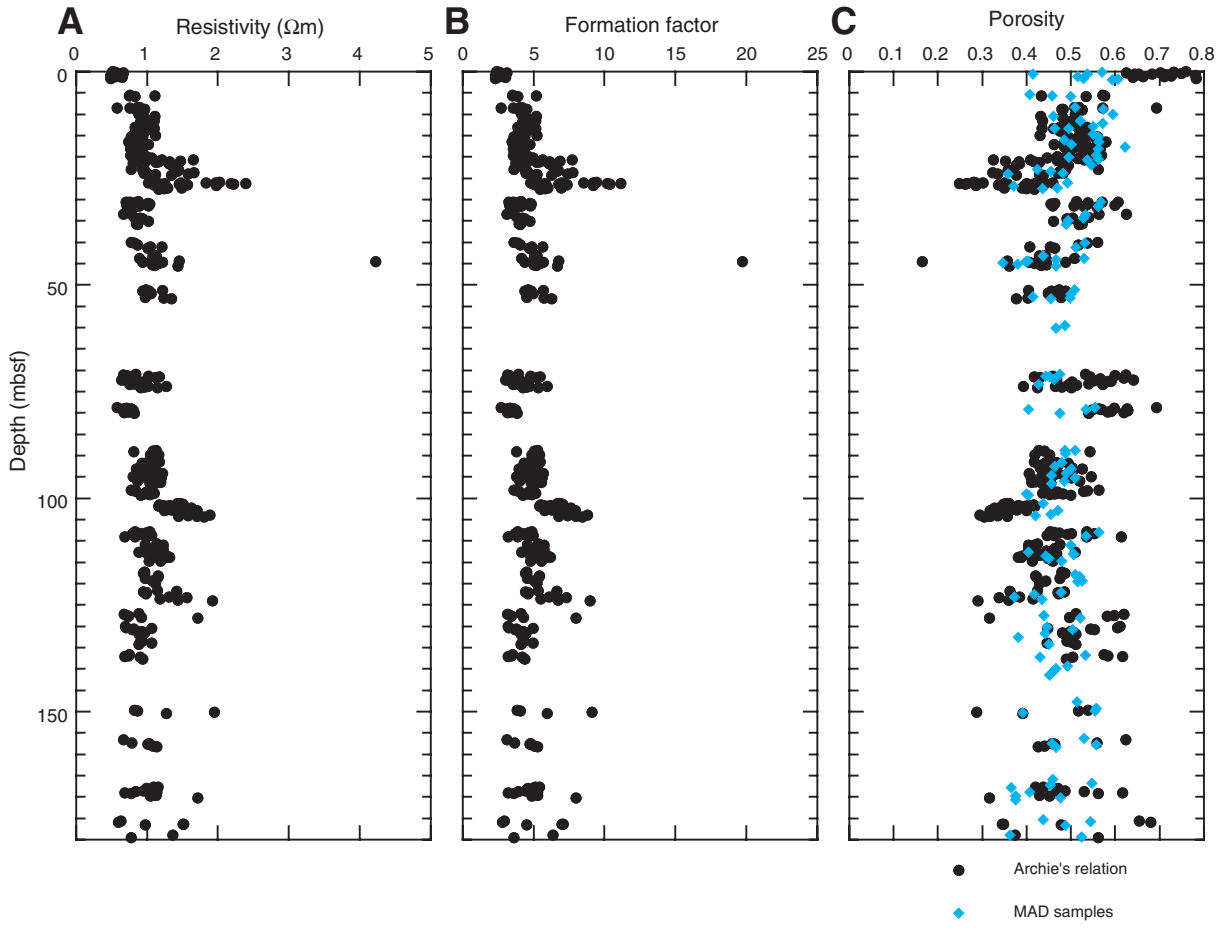

Figure F38 (continued). D. Formation factor vs. MAD porosity. Best-fit Archie's parameters were determined separately for porosities >0.45 (dark gray) and <0.45 (light blue).

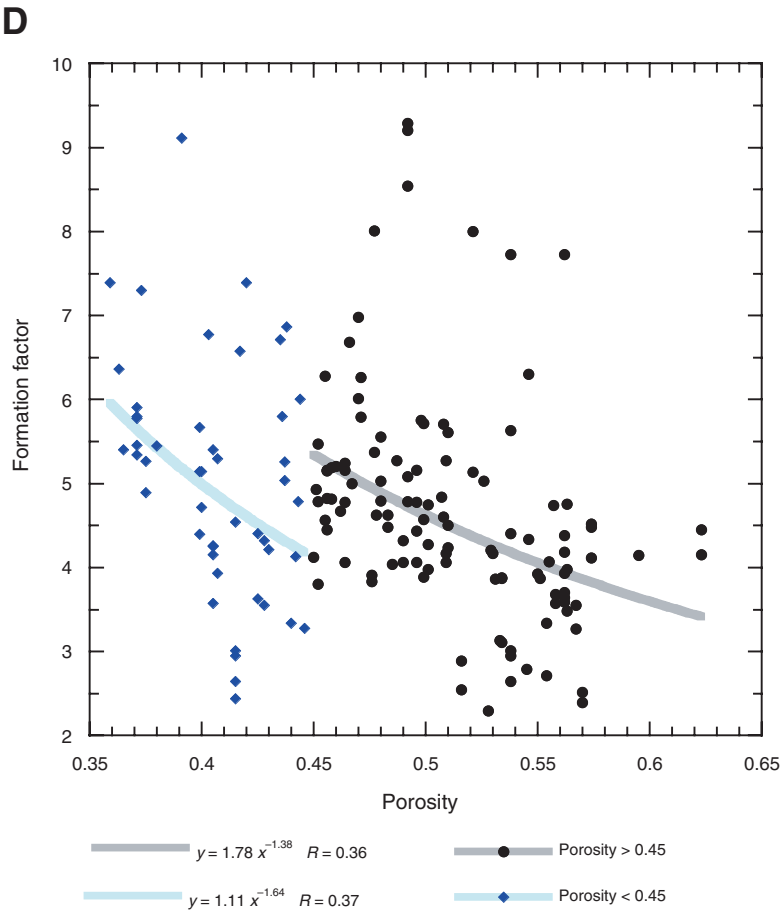

Figure F39. Third-generation advanced piston corer temperature (APCT-3; APC3 in figure) tool and Davis-Villinger Temperature Probe (DVTP) in situ temperature data from Site U1326. Both the upper (black) and lower (blue) thermistors are shown for DVTP data.

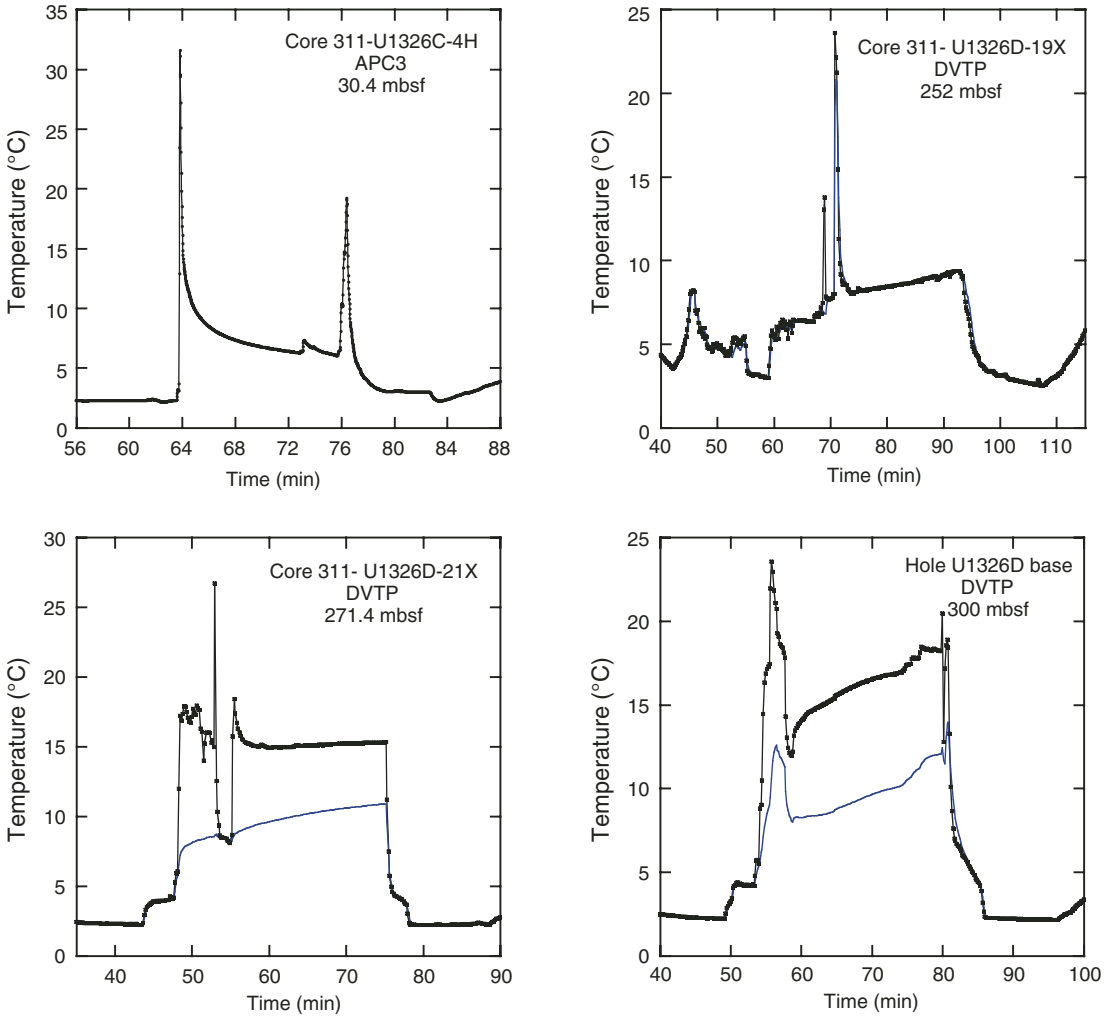

Figure F40. A. All reliable in situ temperature measurements obtained during Expedition 311. Data from ODP Leg 146 Site 889 are also included. **B.** Regional heat flow trend (dashed lines; Hyndman and Wang, 1993) compared to heat flow estimated at Sites U1325–U1329 assuming a thermal conductivity value of 1.1 W/(m·K). The depth to the base of the gas hydrate stability zone (GHSZ) implied by the temperature measurements is also shown. **C.** Seismic transect across the margin showing the structural setting of the Expedition 311 sites. BSR = bottom-simulating reflector.

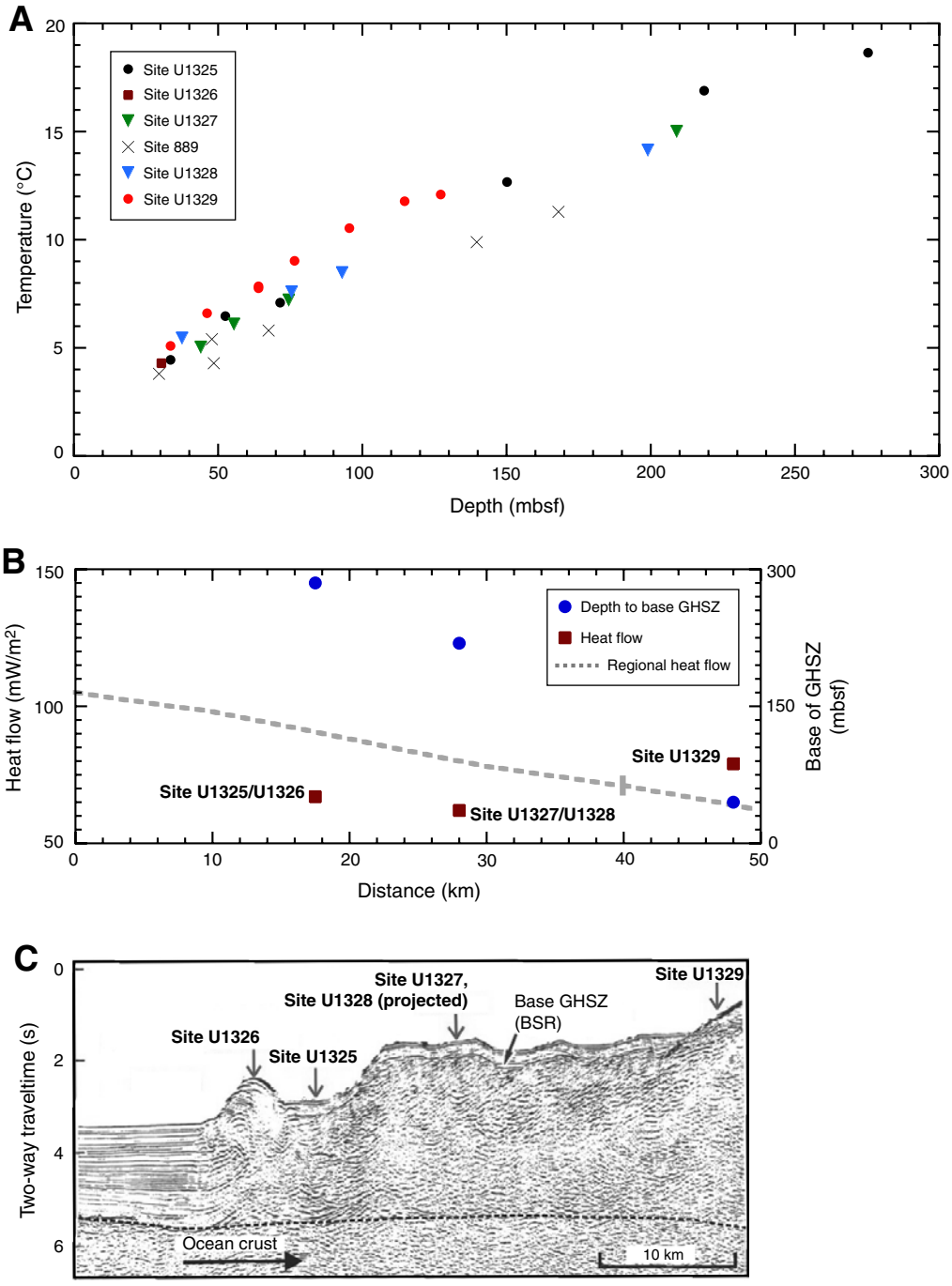

Figure F41. Paleomagnetic data after 20 mT alternating-field demagnetization from Holes U1326C and U1326D.

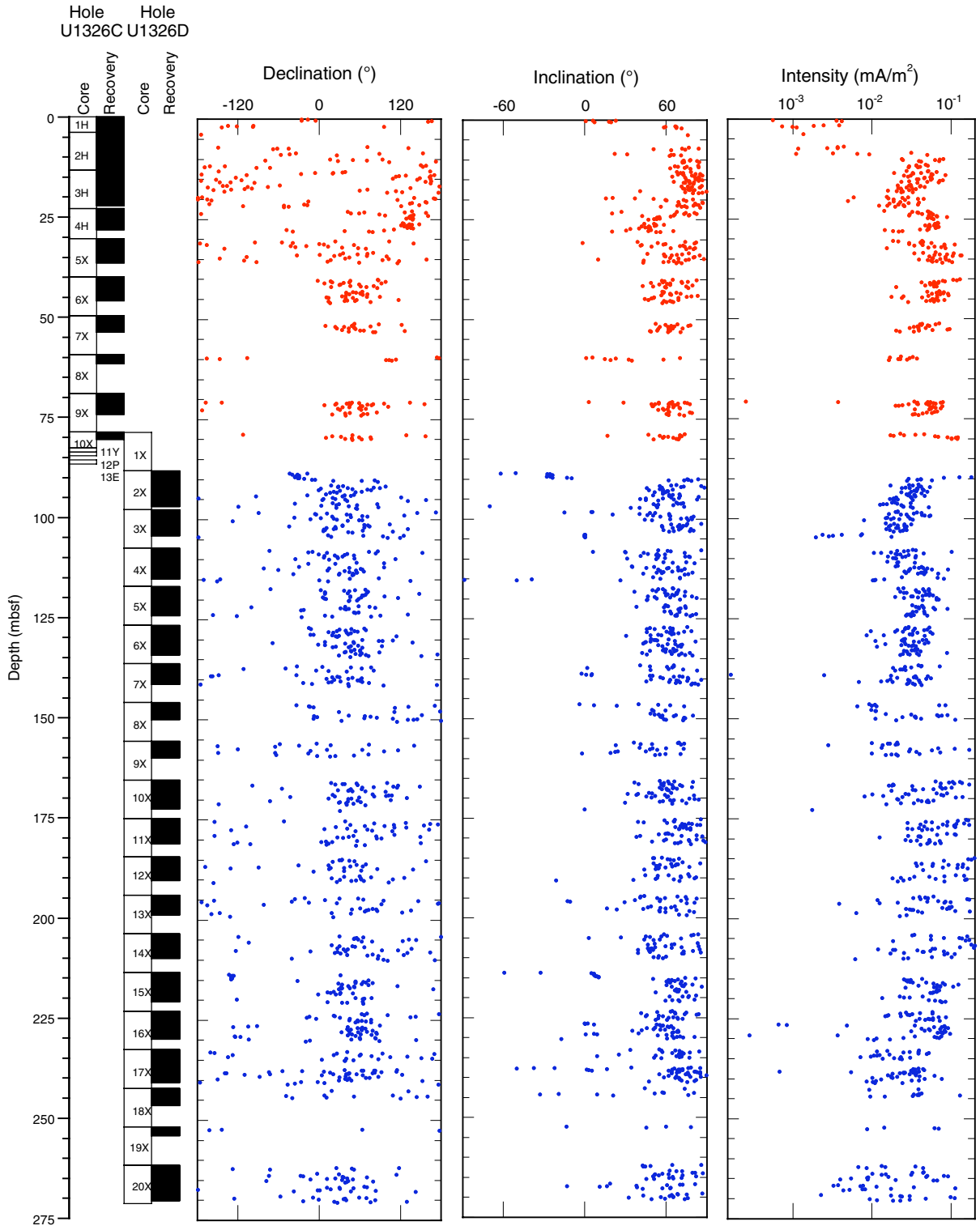

Figure F42. Temperature and pressure vs. elapsed time for each pressure core deployment as recorded by the corer's internal data logger. Deployment and recovery are shaded orange, operation at coring depth is shaded yellow, and autoclave immersion in the cold shuck is shaded blue. There are no data for Core 311-U1326C-13E.

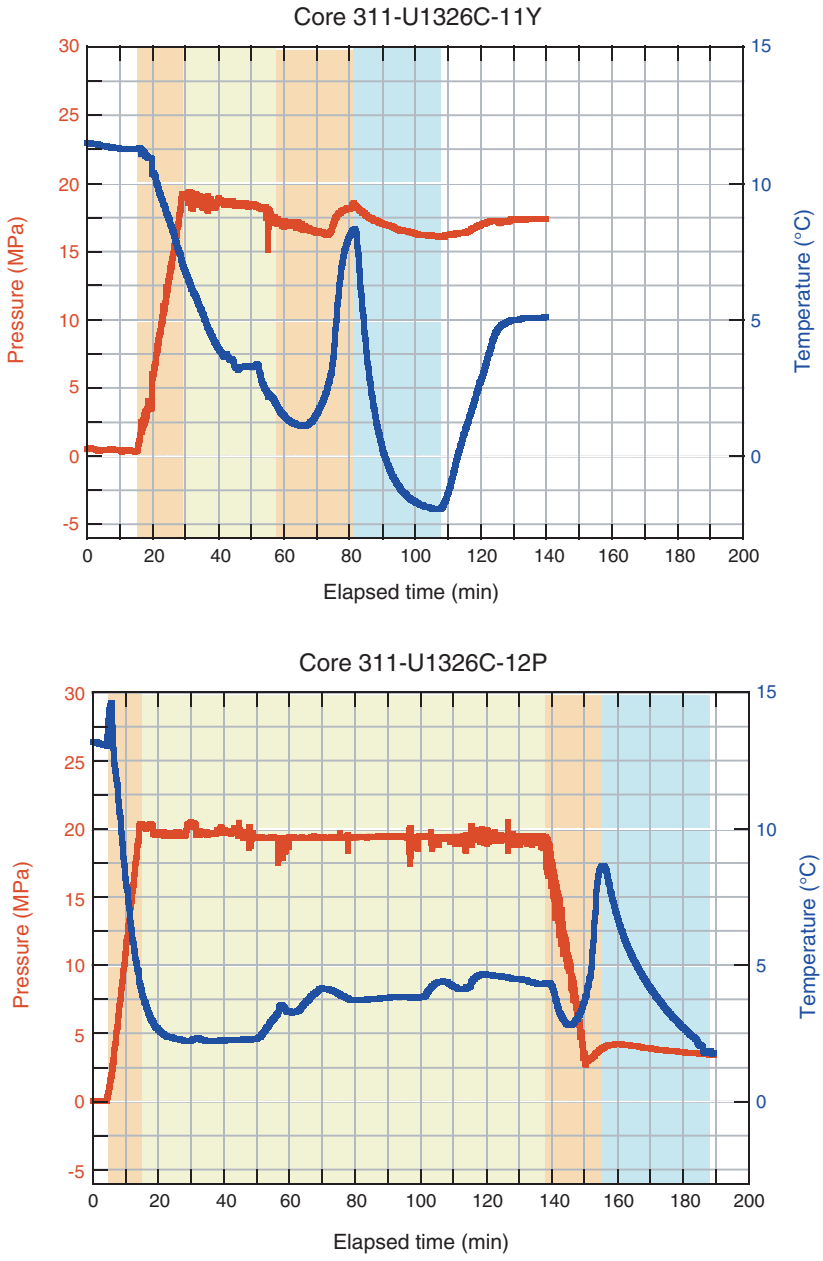

Figure F43. Temperature vs. pressure for all pressure core deployments, showing trajectories relative to gas hydrate stability at 30 and 40 ppt salinity (Xu, 2002, 2004). Circles = final temperature and pressure of autoclave prior to data logger removal, squares = pressure and temperature conditions in the cold laboratory van. There are no data for the deployment of Core 311-U1326C-13E.

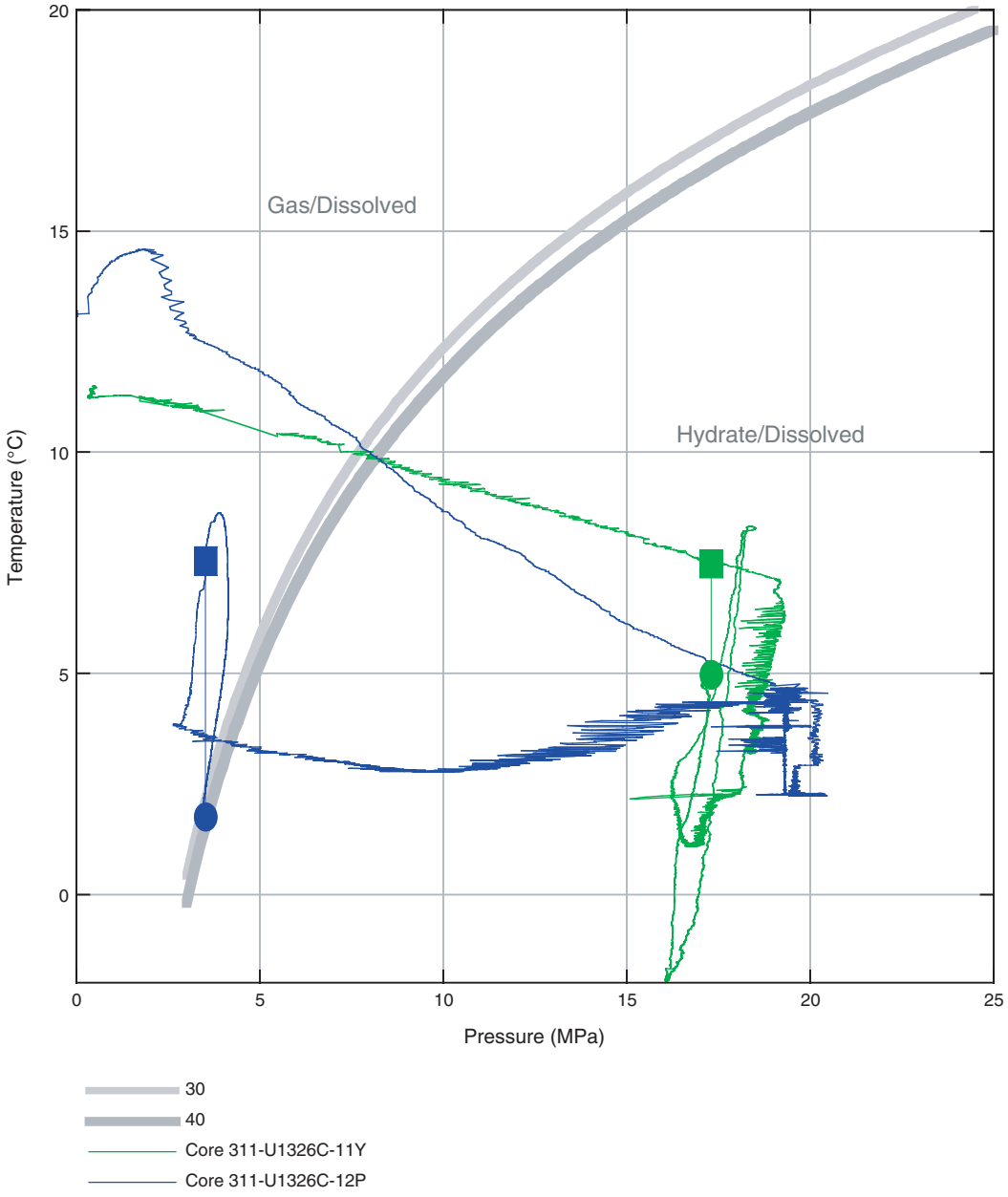

Figure F44. Methane phase diagram with total methane concentration measured from the single degassed PCS core at Site U1326. The seafloor temperature was estimated from previous sites, the salinity profile was taken from Table **T4**, and methane saturation was calculated according to Xu (2002, 2004). Methane phase boundaries for five different thermal gradients are plotted, as in situ temperature measurements were extremely difficult at this site (see **"In situ temperature profile"**). BSR = bottom-simulating reflector.

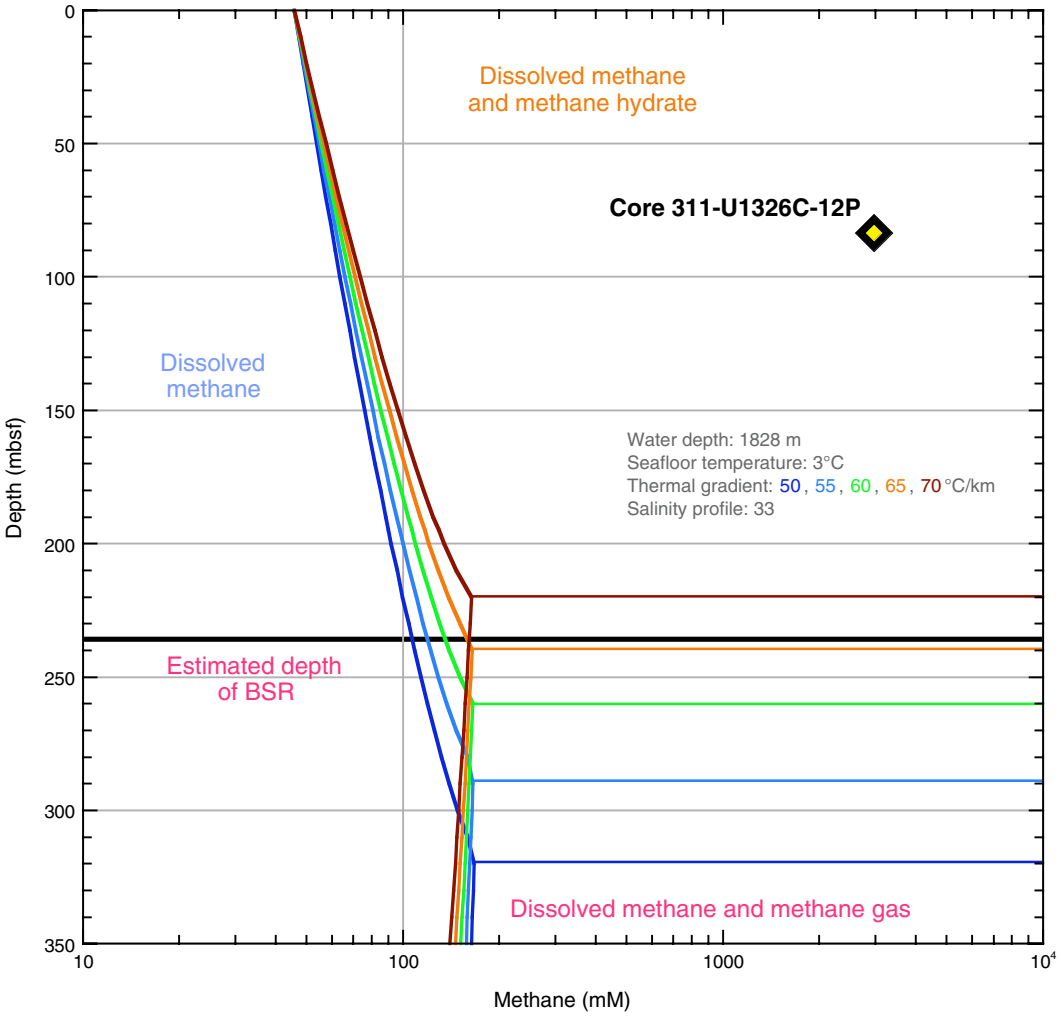

Figure F45. Pressure vs. released gas volume for PCS Core 311-U1326C-12P. Arrows = placement of gamma ray density scans.

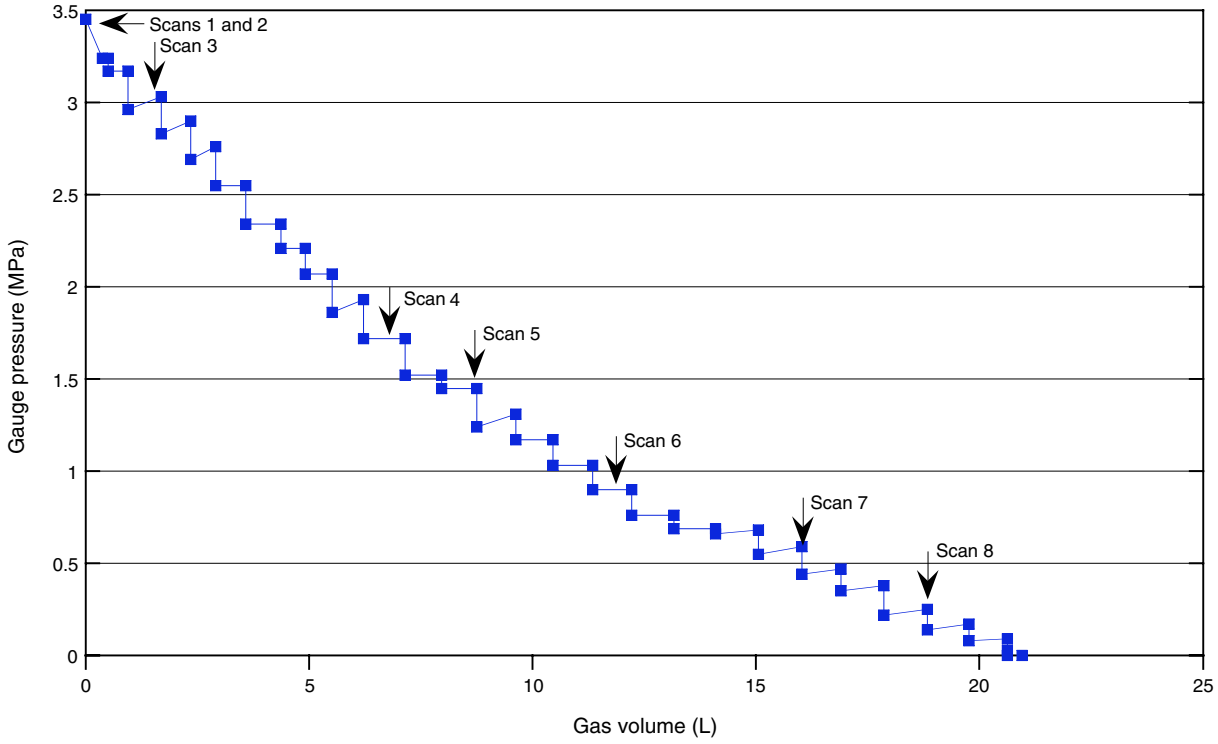

Figure F46. Summary of data collected from Core 311-U1326C-12P, including gamma ray density scans collected during degassing, X-ray images collected before degassing, and chlorinity data collected in selected zones after core extrusion. Gamma ray density scans were shown as differential density plots (i.e., as profiles from which the initial profile has been subtracted). The colored boxes indicate the initial state of the core before degassing (brown = sediment, blue = water, light green = gas).

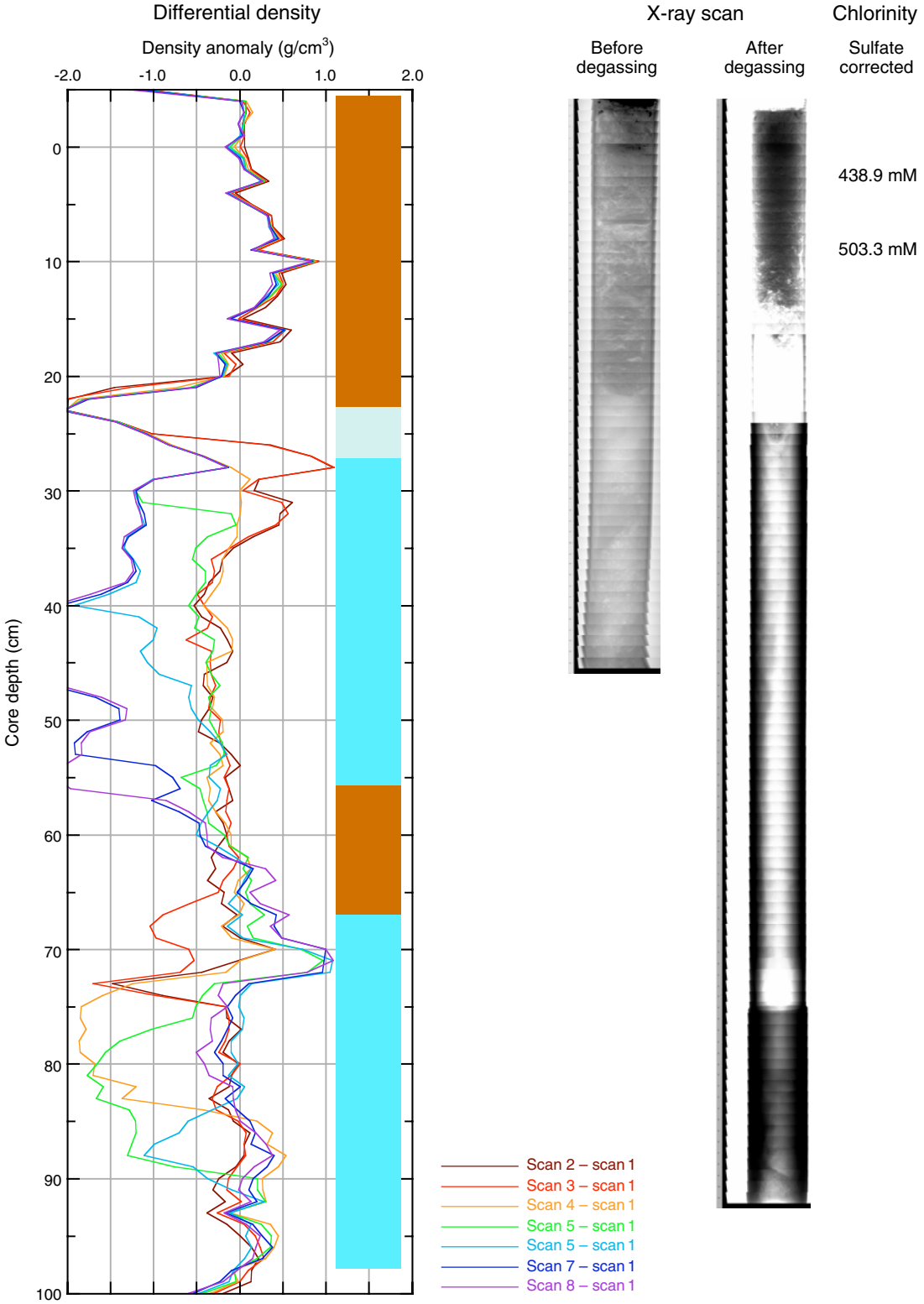

Figure F47. Pressure core data collected at 18 MPa and 7°C for Core 311-U1326C-11Y, including gamma ray density, *P*-wave velocity, and X-ray image. The X-ray image has been stretched 250% in the cross-core direction to show detail.

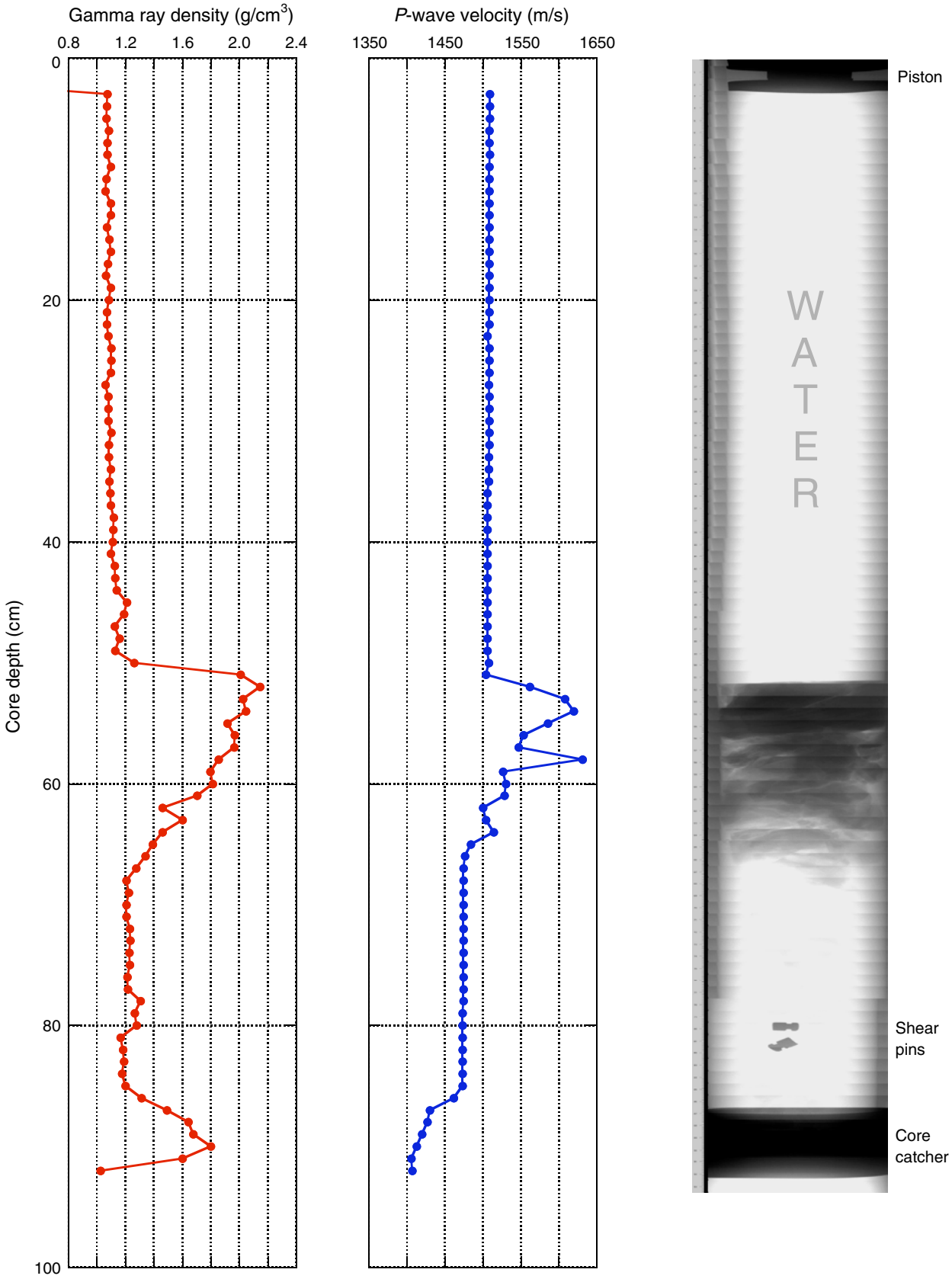

Figure F48. Gamma ray density vs. *P*-wave velocity for Core 311-U1326C-11Y. Data are also for Cores 311-U1327D-12E, 14E, and 311-U1329E-9E, with the two interpreted gas hydrate–containing intervals highlighted in pink and green. The best-fit line to points showing a "normal" positive correlation between density and *P*-wave velocity is shown in blue. The red box encompasses anomalous high-velocity points.

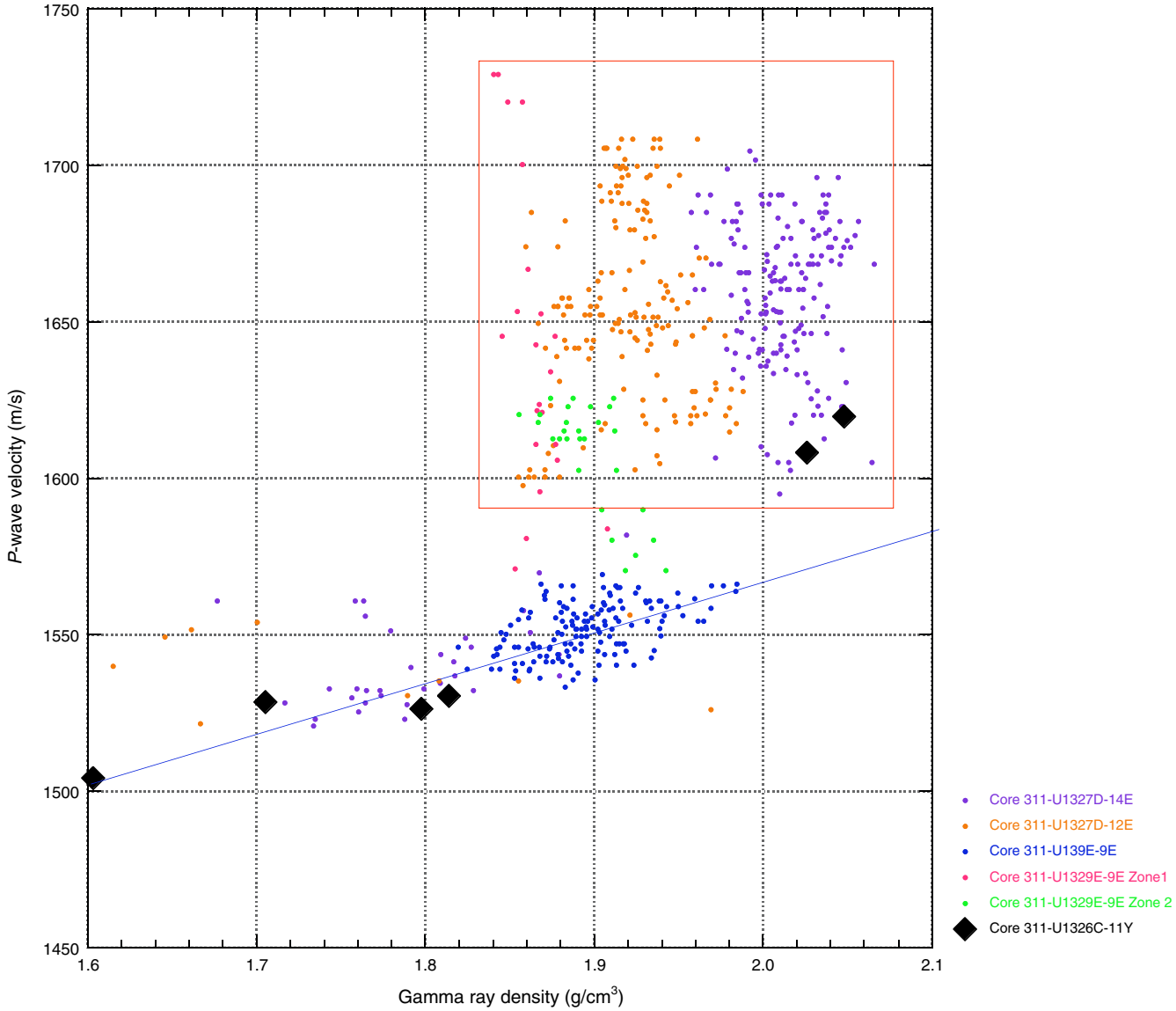

Figure F49. Monitoring and quality control LWD/MWD logs from Hole U1326A.

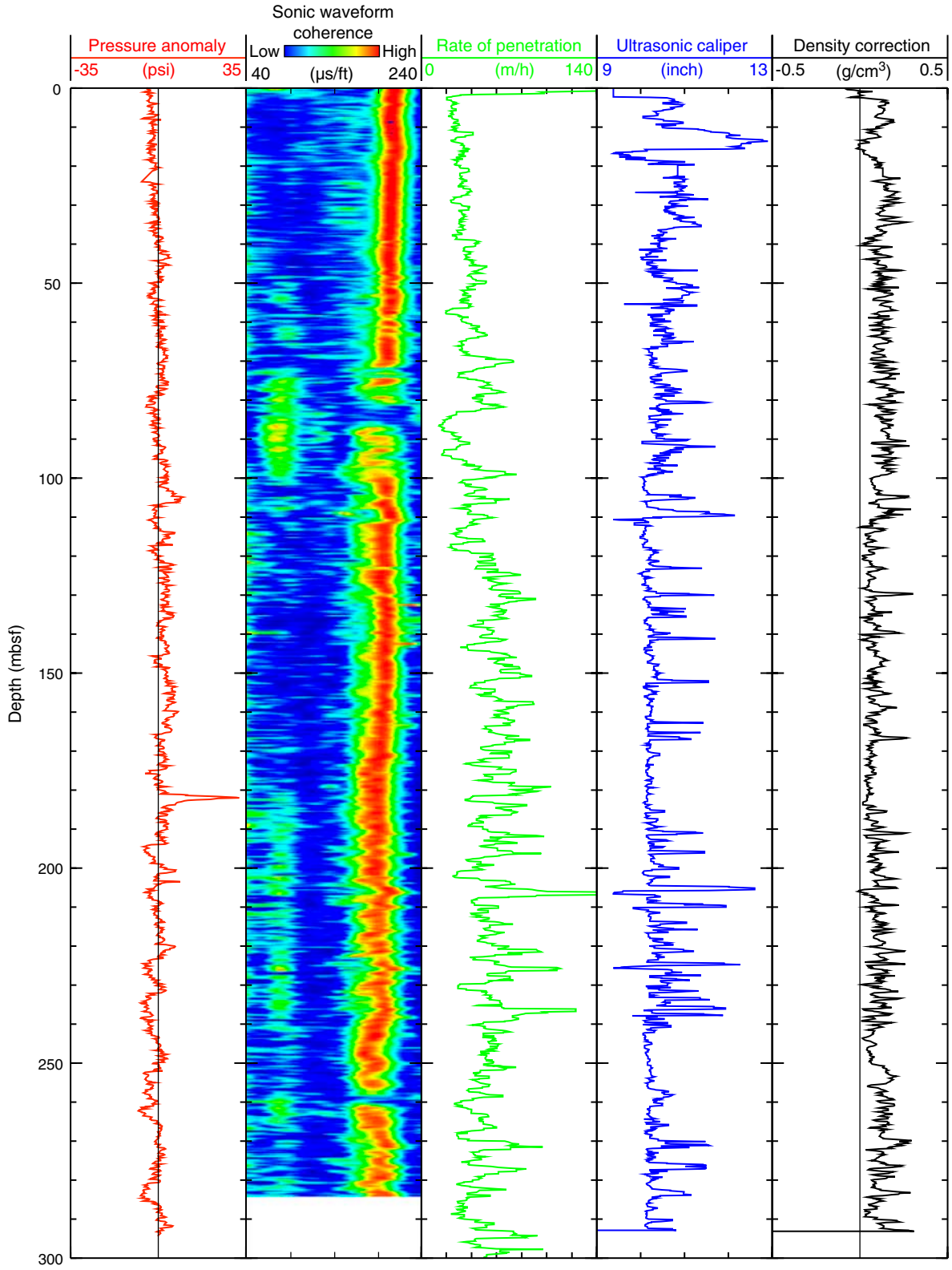

Figure F50. Summary of LWD data from Hole U1326A. Core recovery for Holes U1326C and U1326D are shown for reference. P16B = phase-shift resistivity measured by the EcoScope tool at a source-receiver spacing of 16 in (41 cm), A40B = attenuation resistivity measured by the EcoScope tool at a source-receiver spacing of 40 in (102 cm), RAB = resistivity-at-the-bit image obtained by the GeoVISION tool.

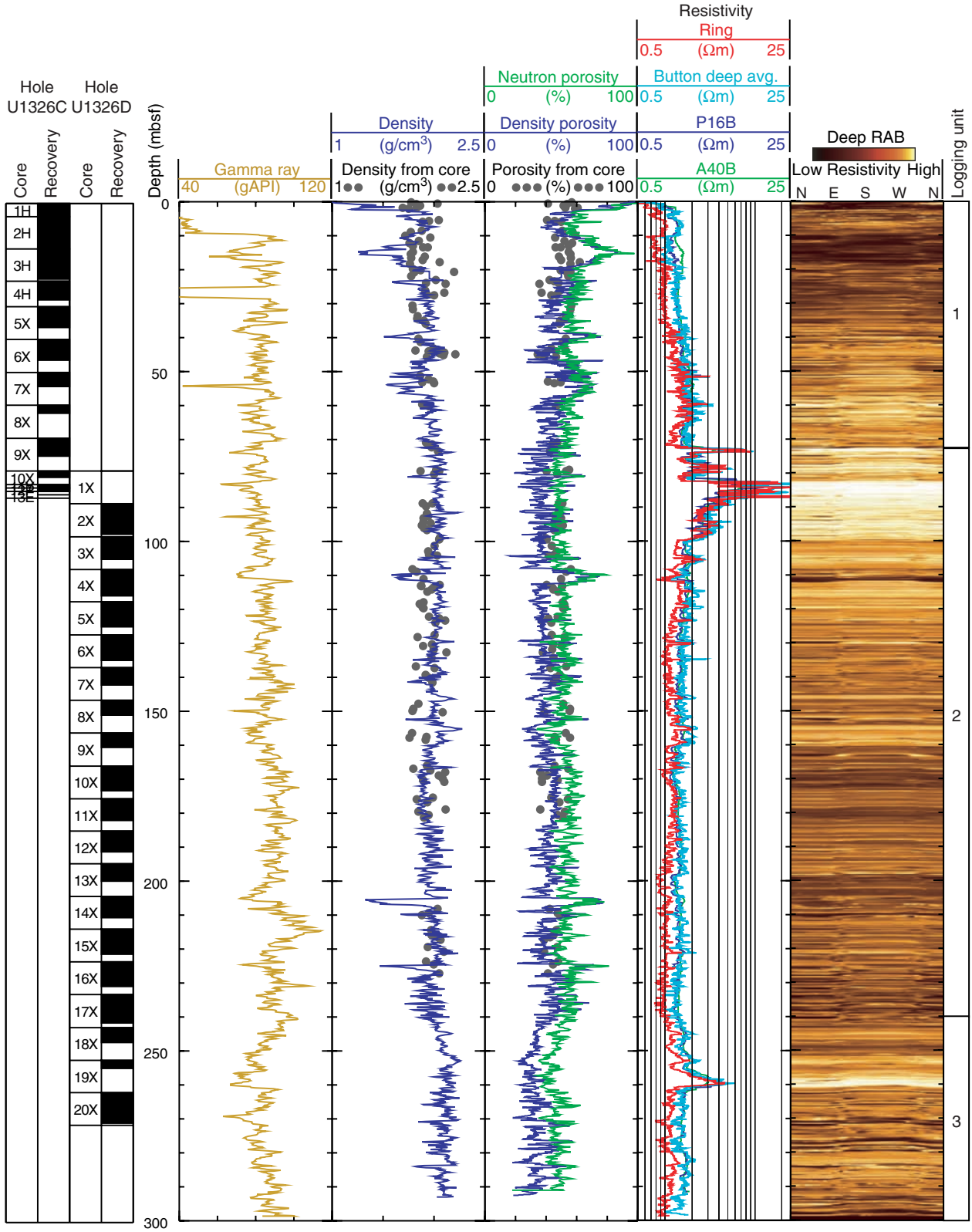

Figure F51. Summary of wireline logging data from Holes U1326C and U1326D. SFLU = spherically focused resistivity, V_P = *P*-wave velocity, V_S = *S*-wave velocity.

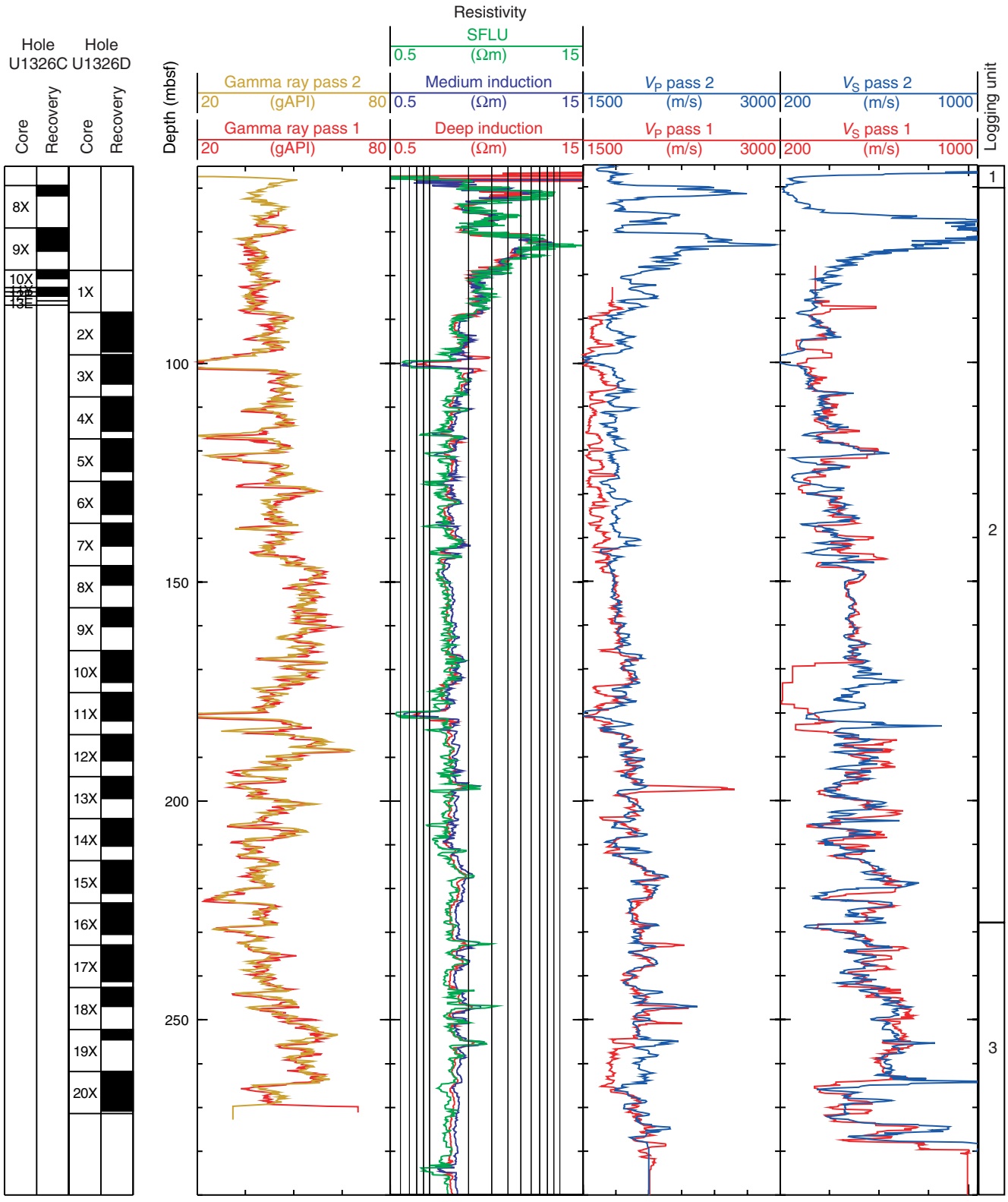

Figure F52. Sonic waveform data, *P*-wave velocity, and *S*-wave velocity obtained with the wireline Dipole Sonic Imager tool in Hole U1326D. V_P = *P*-wave velocity, V_S = *S*-wave velocity, UD = upper dipole, LD = lower dipole, mono. = monopole.

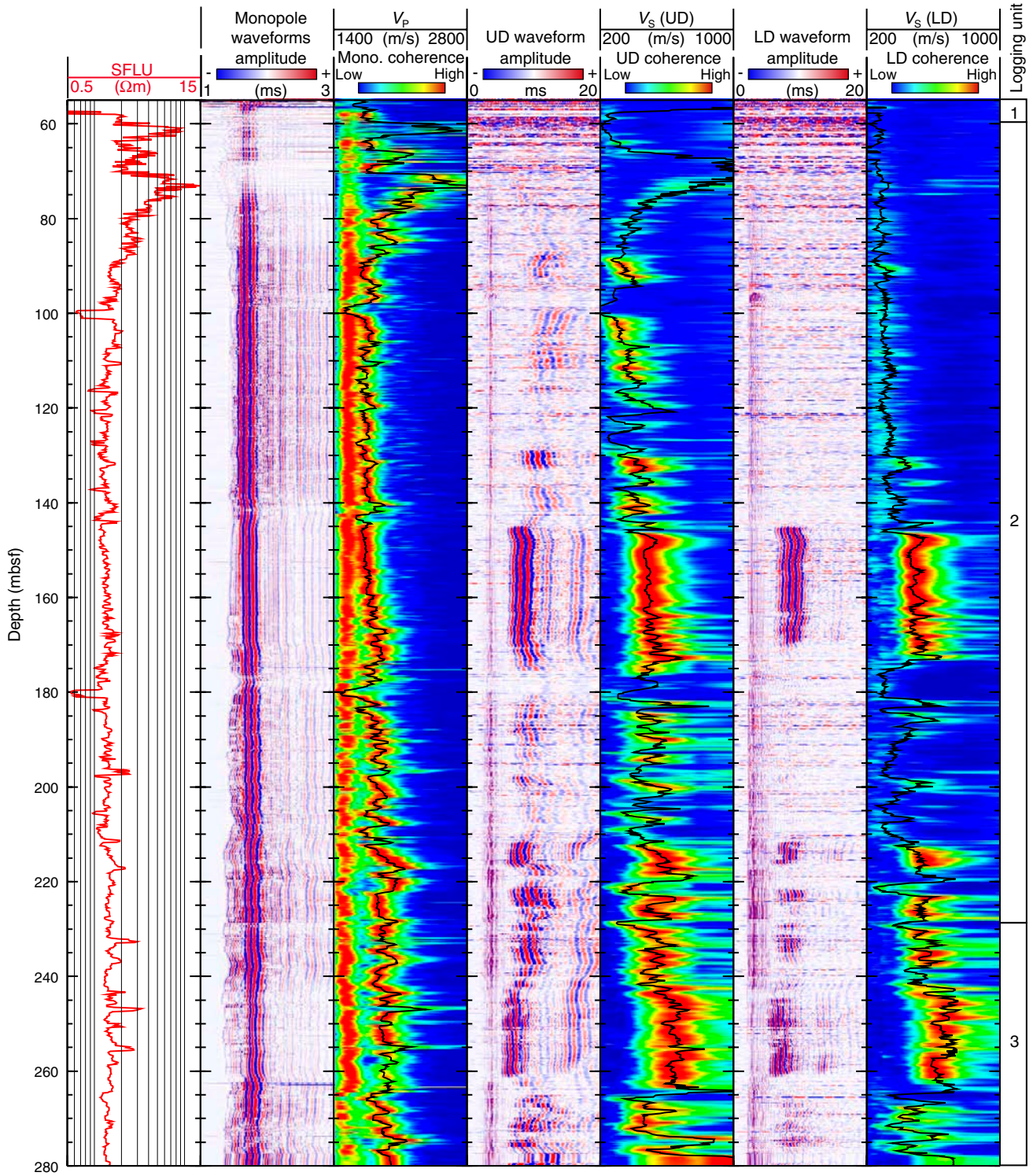

Figure F53. Comparison of logging-while-drilling (LWD; Hole U1326A) and wireline logging (WL; Hole U1326D) data. Core recovery for Holes U1326C and U1326D are shown for reference. P16B = phase-shift resistivity measured by the EcoScope tool at a source-receiver spacing of 16 in (41 cm), avg. = average.

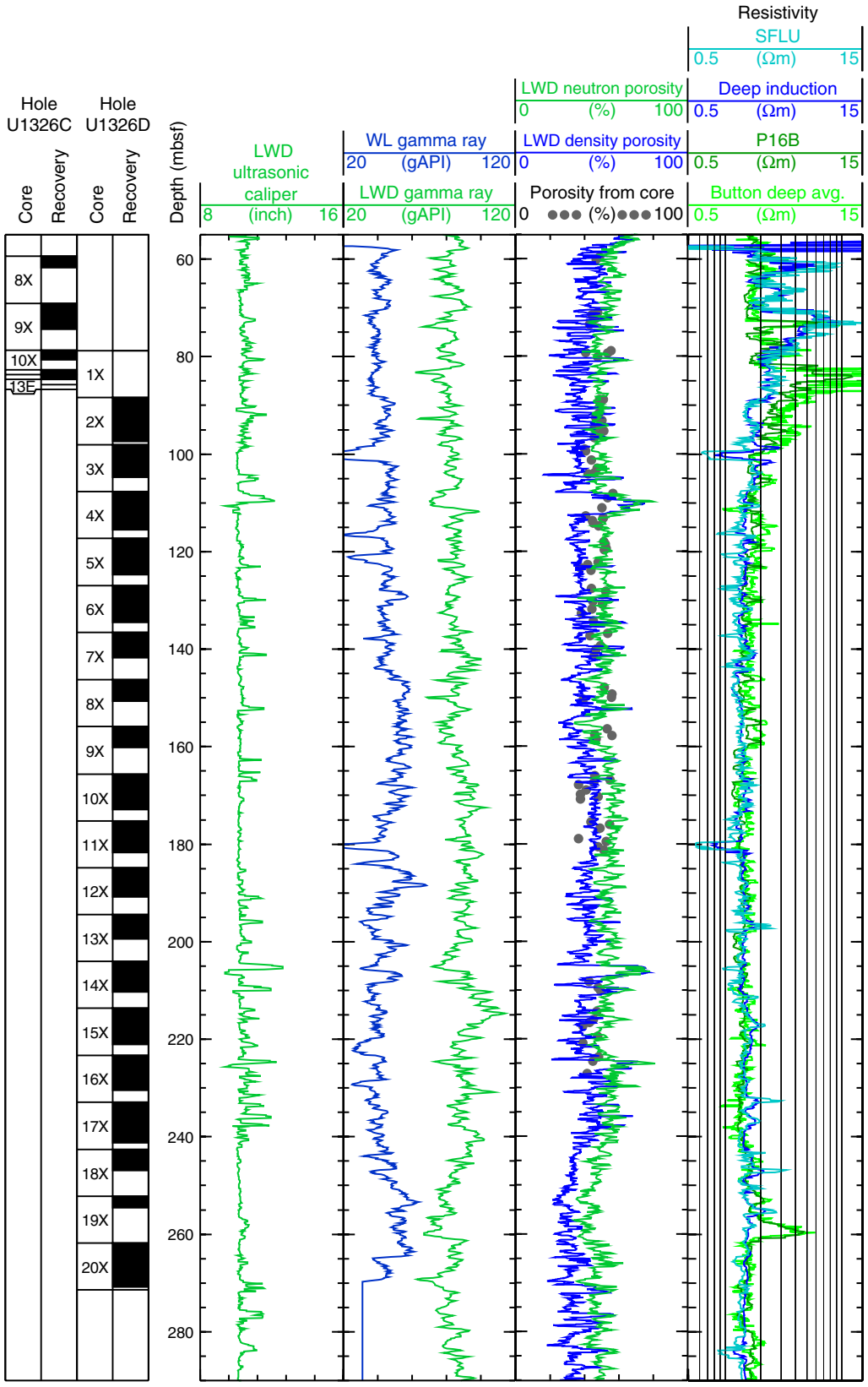

Figure F54. LWD image data from Hole U1326A. Core recovery for Holes U1326C and U1326D are shown for reference. RAB = resistivity-at-the-bit image obtained by the GeoVISION tool.

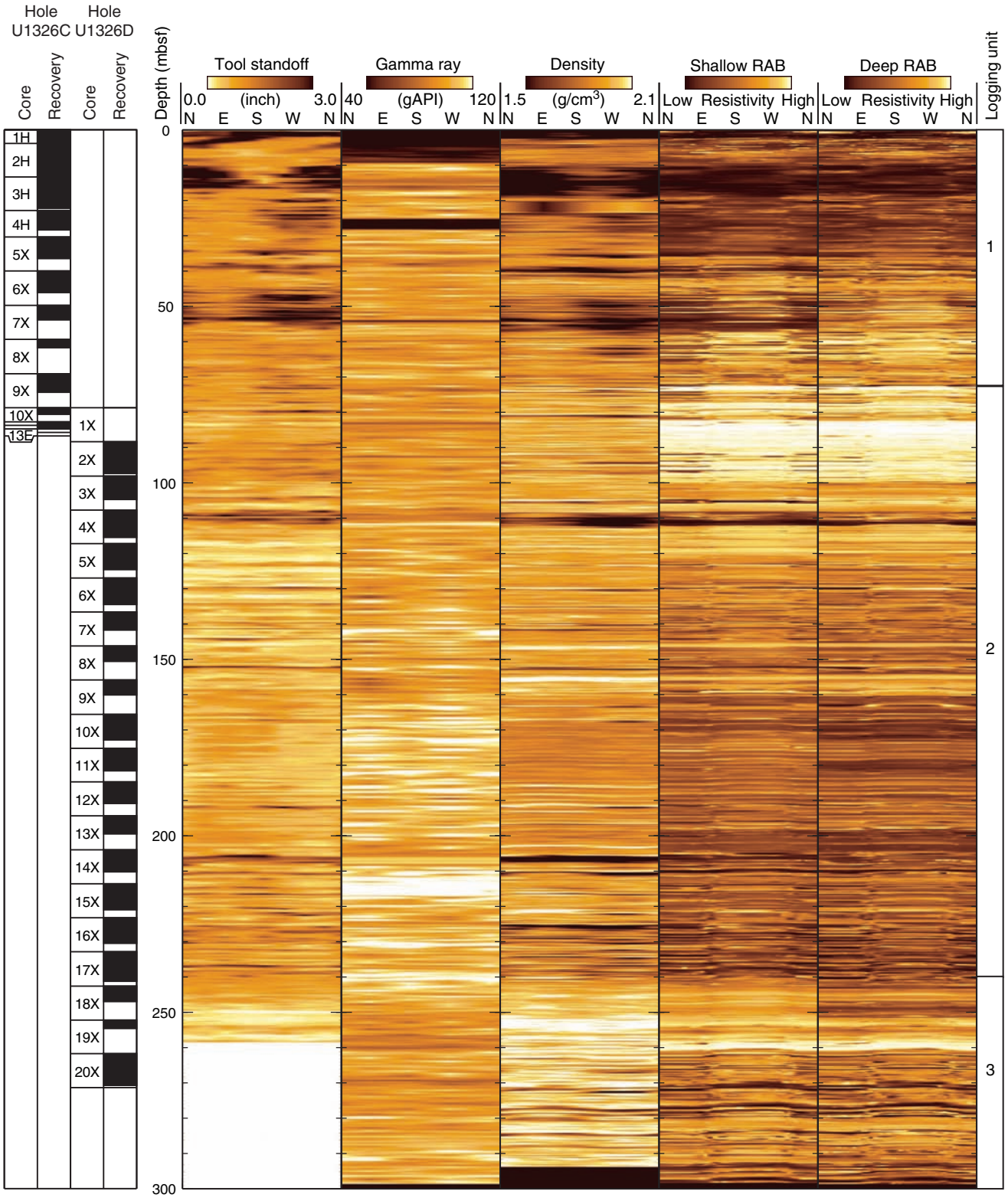

Figure F55. LWD resistivity images of layers in Hole U1326A. The "tadpoles" on the left show dip and azimuth of each layer, the fan plots show the azimuth of all layers in the intervals 95–145, 145–194, 194–243, and 243–293 mbsf. There is no systematic change of dip and azimuth with depth, and all layers dip to the north-northeast with dip angles of 45°–85°. RAB = resistivity-at-the-bit image obtained by the GeoVISION tool.

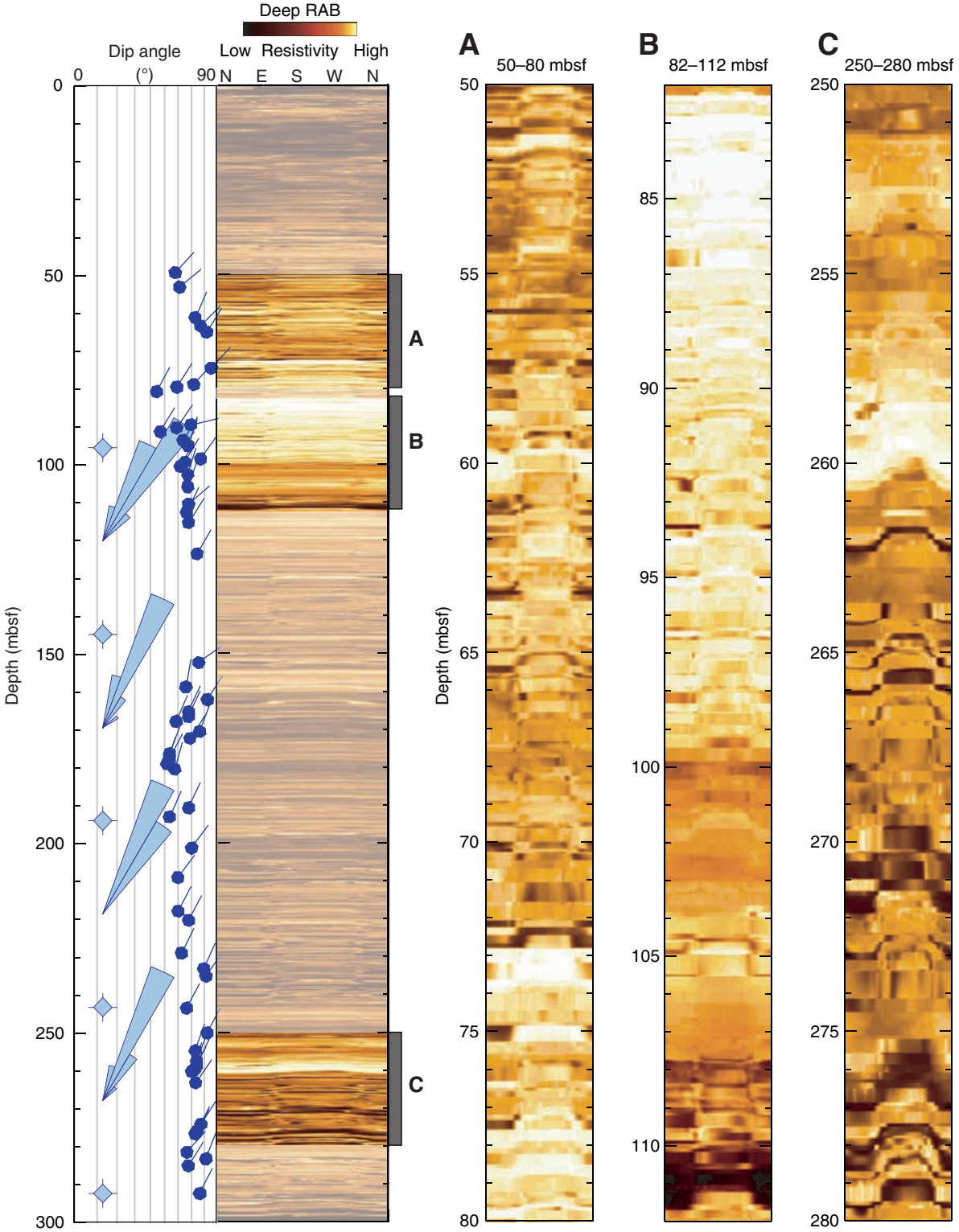

Figure F56. Comparison of LWD porosity logs with core-derived porosity data.

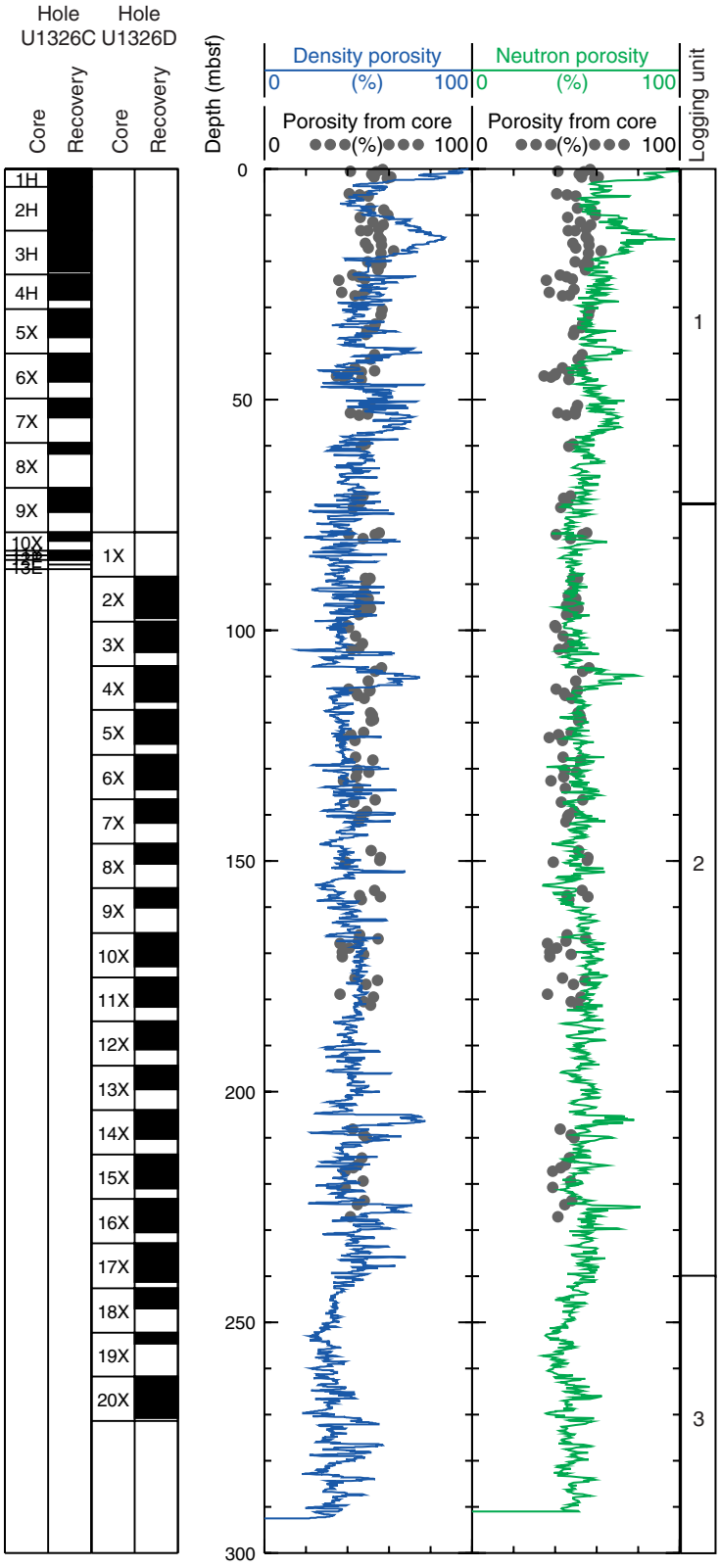

Figure F57. Water saturations from Archie's equation and LWD porosity and resistivity logs. The intervals marked in gray correspond to hole enlargements, where the measured density is erroneously low and the calculated water saturation is unreliable. R_w = formation water resistivity, m = cementation coefficient, R_0 = computed formation resistivity for 100% water saturation, R_t = measured resistivity, S_w = water saturation, RAB = resistivity-at-the-bit image from the GeoVISION tool.

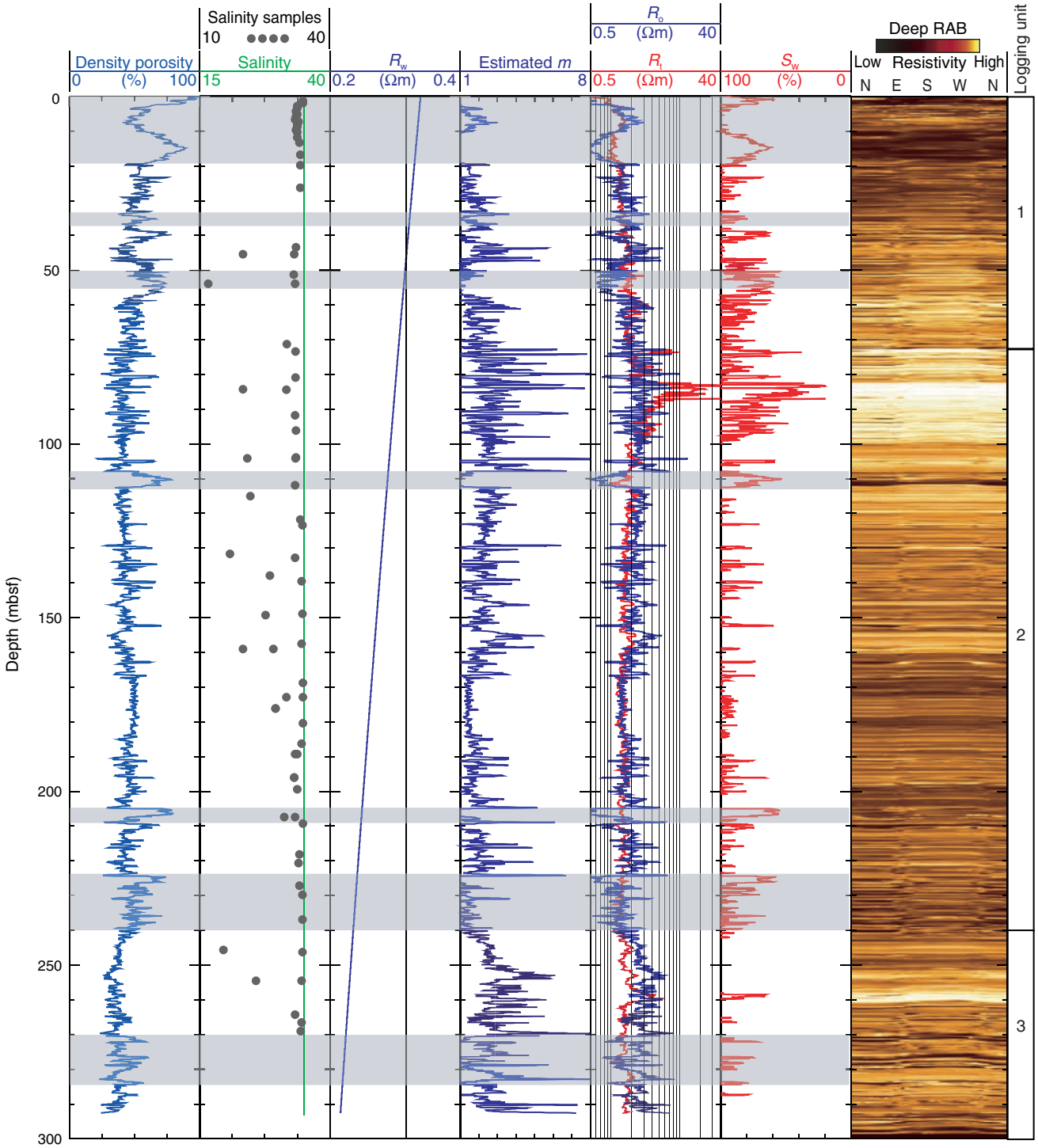

Figure F58. Comparison between LWD resistivity (Hole U1326A), wireline resistivity (Hole U1326D), and infrared (IR) images (Holes 1326C and 1326D). Note that the IR images from 0 to 88.4 mbsf are from Hole U1326C, and the IR images from 88.4 to 300 mbsf are from Hole U1326D. RAB = resistivity-at-the-bit image obtained by the GeoVISION tool, P16B = EcoScope phase-shift resistivity, avg. = average, SFLU = spherically focused resistivity, Med. = medium. White areas in the IR image indicate zones of no core recovery.

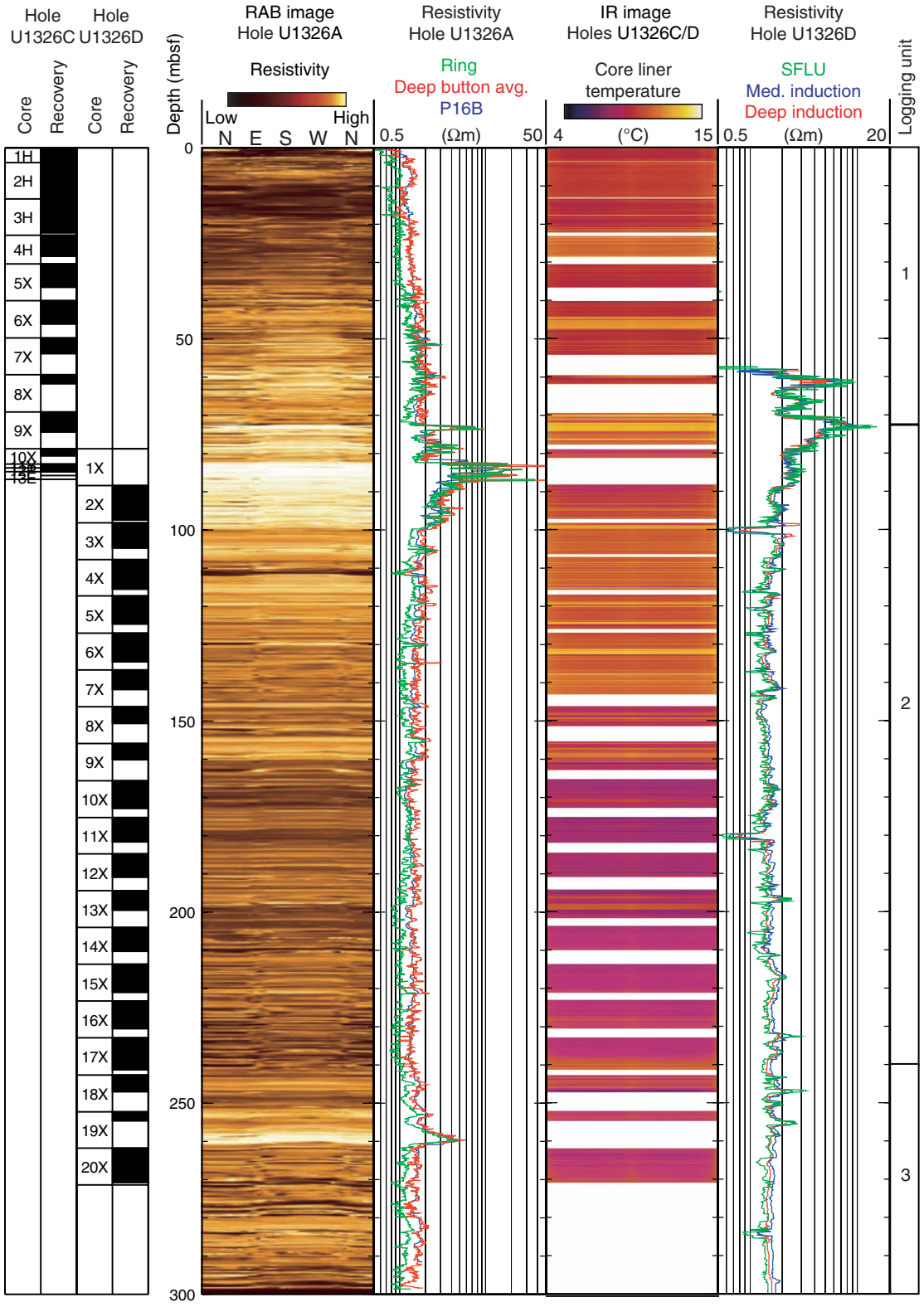

Table T1. Site U1326 coring summary. (See table note. Continued on next page.)

Hole U1326A
Latitude: 48°37.635′N
Longitude: 127°3.029′W
Seafloor (drill pipe measurement from rig floor, mbrf): 1839.0
Distance between rig floor and sea level (m): 10.9
Water depth (drill pipe measurement from sea level, m): 1828.1
Total penetration (mbsf): 300.0
Total drilled interval (m): 300.0; LWD/MWD

Hole U1326B
Latitude: 48°37.638′N
Longitude: 127°3.023′W
Seafloor (drill pipe measurement from rig floor, mbrf): 1840.0
Distance between rig floor and sea level (m): 11.6
Water depth (drill pipe measurement from sea level, m): 1828.4
Total penetration (mbsf): 1.5

Hole U1326C
Latitude: 48°37.638′N
Longitude: 127°3.023′W
Seafloor (drill pipe measurement from rig floor, mbrf): 1839.6
Distance between rig floor and sea level (m): 11.6
Water depth (drill pipe measurement from sea level, m): 1828.0
Total penetration (mbsf): 86.7
Total drilled interval (m): 1.0

Hole U1326D
Latitude: 48°37.628′N
Longitude: 127°3.043′W
Seafloor (drill pipe measurement from rig floor, mbrf): 1839.6
Distance between rig floor and sea level (m): 11.7
Water depth (drill pipe measurement from sea level, m): 1827.9
Total penetration (mbsf): 300.0
Total drilled interval (m): 107.4

Core, section	Date (Oct 2005)	Local time (h)	Top depth (mbsf)	Length (m) Cored	Length (m) Recovered	Recovery (%)	Comments
311-U1326A-							
		*****Drilled from 0.0 to 300.0 mbsf*****					LWD/MWD
311-U1326B-							
1H	23	1215	0	1.5	1.55	103.3	
		Core totals:		1.5	1.55	103.3	
311-U1326C-							
1H	23	1300	0	3.9	3.93	100.8	Fluorescent microspheres
2H	23	1405	3.9	9.5	9.77	102.8	Fluorescent microspheres
3H	23	1500	13.4	9.5	8.88	93.5	Fluorescent microspheres
4H	23	1615	22.9	7.5	5.42	72.3	APCT-3; fluorescent microspheres; imploded liner
5X	23	1935	30.4	9.6	6.15	64.1	Fluorescent microspheres
6X	23	2120	40	9.7	6.09	62.8	Fluorescent microspheres
7X	23	2245	49.7	9.7	4.17	43.0	Fluorescent microspheres
8X	23	2359	59.4	9.7	2.31	23.8	Fluorescent microspheres
9X	24	0215	69.1	9.6	5.31	55.3	Fluorescent microspheres
10X	24	0310	78.7	4	1.95	48.8	Fluorescent microspheres
11Y	24	0445	82.7	1	0.15	15.0	Fluorescent microspheres
12P	24	0730	83.7	1	0.26	26.0	Fluorescent microspheres
		*****Drilled from 83.7 to 85.7*****					Overdrill pressure core
13E	24	0905	85.7	1	0.00	0.0	Fluorescent microspheres
		Core totals:		85.7	54.39	63.5	
311-U1326D-							
1X	24	2010	78.8	9.6	0.00	0.0	Fluorescent microspheres
2X	24	2205	88.4	9.7	9.00	92.8	Fluorescent microspheres
3X	25	0010	98.1	9.6	6.62	69.0	Fluorescent microspheres
4X	25	0305	107.7	9.6	7.83	81.6	Fluorescent microspheres
5X	25	0500	117.3	9.7	7.37	76.0	Fluorescent microspheres
6X	25	0630	127.0	9.6	7.47	77.8	Fluorescent microspheres
7X	25	0900	136.6	9.7	5.20	53.6	Fluorescent microspheres
8X	25	1030	146.3	9.6	4.35	45.3	Fluorescent microspheres
9X	25	1300	155.9	9.7	4.28	44.1	Fluorescent microspheres
10X	25	1425	165.6	9.6	7.32	76.2	Fluorescent microspheres

Table T1 (continued).

Core, section	Date (Oct 2005)	Local time (h)	Top depth (mbsf)	Length (m) Cored	Length (m) Recovered	Recovery (%)	Comments
11X	25	1555	175.2	9.6	6.46	67.3	Fluorescent microspheres
12X	25	1730	184.8	9.6	6.04	62.9	Fluorescent microspheres
13X	25	1910	194.4	9.6	5.04	52.5	Fluorescent microspheres
14X	25	2100	204.0	9.6	6.29	65.5	Fluorescent microspheres
15X	25	2225	213.6	9.7	7.46	76.9	Fluorescent microspheres
16X	25	2355	223.3	9.6	7.14	74.4	Fluorescent microspheres
17X	26	0130	232.9	9.7	8.35	86.1	Fluorescent microspheres
18X	26	0320	242.6	9.6	4.36	45.4	DVTP at 252.2 mbsf; fluorescent microspheres
19X	26	0645	252.2	9.6	2.39	24.9	Fluorescent microspheres
20X	26	0900	261.8	9.6	8.99	93.6	DVTP at 271.4 mbsf; fluorescent microspheres
*****Drilled from 261.8 to 300.0 mbsf*****							DVTP at 300.0 mbsf
			Core totals:	192.6	121.96	63.3	

Note: LWD/MWD = logging while drilling/measurement while drilling, APCT-3 = third-generation advanced piston corer temperature tool, DVTP = Davis-Villinger Temperature Probe.

Table T2. Occurrence of diatoms, Holes U1326B, U1326C, and U1326D. (**See table notes.** Continued on next page.)

Age	Diatom zone	Core, section	Depth (mbsf)	Abundance	Number of diatom valves/row × 100	Preservation	Marine diatoms: *Actinocyclus curvatulus* Janisch	*Actinoptychus senarius* (Ehrenberg) Ehrenberg	*Coscinodiscus* spp.	*Neodenticula seminae* (Simonsen and Kanaya) Akiba and Yanagisawa	*Paralia sulcata* (Ehrenberg) Cleve	*Proboscia curvirostris* (Jousé) Jordan and Priddle	*Stephanopyxis dimorpha* Schrader	*Stephanopyxis* spp.	*Thalassionema nitzschioides* H. and M. Peragallo	*Thalassiosira jouseae* Akiba	*Thalassiosira* spp.	Miscellaneous	Nonmarine diatoms: *Aulacoseira granulata* (Ehrenberg) Simonsen s.l.	*Cyclotella* spp.	*Stephanodiscus* spp.	Miscellaneous	Total number of valves	Resting spores of *Chaetoceros* spp.	Marine and nonmarine diatoms ratio
		311-U1326B-																							
		1H-CC	1.50	B																			0		
		311-U1326C-																							
	NPD12	1H-CC	3.88	VR	0.4	M			+				3	5	2		2	2	20			1	35	12	
		2H-CC	13.62	C	13.7	M	1	1	1	5	+		8	28	37		3	11	4	1		+	100	49	
		3H-CC	22.13	A	32.0	M	+	+	+	3			12	32	21		14	5	11		1	1	100	304	
		4H-CC	28.27	B																			0		
Holocene–Pleistocene		5X-CC	36.40	VR	0.3	P	+		+					5	+		1		20	3	+	+	29	3	
		6X-CC	45.99	B																			0		
	Not zoned	7XCC	53.69	B																			0		
		8X-CC	61.66	B																			0		
		9X-CC	74.36	VR	+	P							+										+	–	
		10X-CC	80.50	B																			0		
		311-U1326D-																							
		2X-CC	97.35	B																			0		
		3X-CC	104.67	B																			0		
	Not zoned	4X-CC	115.48	B																			0		
		5X-CC	124.62	B																			0		
Pleistocene		6X-CC	134.32	VR	+	P			+					2			1					+	3	–	
		7X-CC	141.65	VR	0.1	P	+		+					1			2		2			+	5	1	
		8X-CC	150.50	C	6.0	P			+	3		1	7	19	34	4	25	2	2	+	1	2	100	149	
	NPD11	9X-CC	160.00	C	9.6	P	+		+			1	20	54	3	3	9	2	7		+	1	100	113	
		10X-CC	172.87	VR	0.5	VP		1	1	2		1	2	18	5		4	5	9		1	2	51	80	
		11X-CC	181.61	VR	+	VP			+					4			+						4	4	

Table T2 (continued).

Age	Diatom zone	Core, section	Depth (mbsf)	Abundance	Number of diatom valves/row × 100	Preservation	Marine diatoms: *Actinocyclus curvatulus* Janisch	*Actinoptychus senarius* (Ehrenberg) Ehrenberg	*Coscinodiscus* spp.	*Neodenticula seminae* (Simonsen and Kanaya) Akiba and Yanagisawa	*Paralia sulcata* (Ehrenberg) Cleve	*Proboscia curvirostris* (Jousé) Jordan and Priddle	*Stephanopyxis dimorpha* Schrader	*Stephanopyxis* spp.	*Thalassionema nitzschioides* H. and M. Peragallo	*Thalassiosira jouseae* Akiba	*Thalassiosira* spp.	Miscellaneous	Nonmarine diatoms: *Aulacoseira granulata* (Ehrenberg) Simonsen s.l.	*Cyclotella* spp.	*Stephanodiscus* spp.	Miscellaneous	Total number of valves	Resting spores of *Chaetoceros* spp.	Marine and nonmarine diatoms ratio
Pleistocene	NPD11	12X-CC	190.79	VR	0.1	VP			+		1		1	2	1		1		4		+	1	11	31	
		13X-CC	199.39	VR	0.2	P	2		+					2			3	2	11	1	1	+	22	–	
		14X-CC	210.24	B																			0		
		15X-CC	220.91	B																			0		
		16X-CC	230.39	B																			0		
		17X-CC	241.20	B																			0		
		18X-CC	246.91	VR	0.1	VP			+		1		1	3	1			1	4	1			12	16	
		19X-CC	254.44	C	3.6	P	+	4	+	3	1	4	11	26	12		15	1	16	+	3	4	100	98	
	Not zoned	20X-CC	270.69	B																			0		

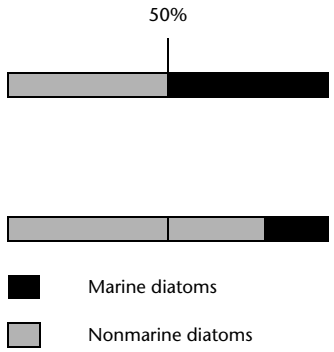

Notes: Abundance: A = abundant, C = common, VR = very rare, B = barren. Preservation: M = moderate, P = poor, VP = very poor. + = <1% and/or valve fragments, – = *Chaetoceros* spp. resting spores not present.

Table T3. Concentrations of solutes in interstitial waters, Site U1326. (See table notes. Continued on next page.)

Core, section, interval (cm)	Depth (mbsf)	Volume (mL)	pH	Alkalinity (mM)	Salinity	Cl (mM)	SO_4 (mM)	PO_4 (µM)	NH_4 (mM)	H_4SiO_4 (µM)	Cations (mM)					Trace elements (µM)			
											Na	K	Mg	Ca	Mg/Ca	Sr	Li	B	Ba
311-U1326C-																			
1H-1, 65–80	0.7	60.0	7.98	6.0	33.8	559.0	21.4	7.2	0.3	385.3	436.8	11.1	46.8	8.4	5.6	77.9	14.8	567.1	0.0
1H-1, 135–150	1.4	62.0	8.19	13.1	33.8	562.5	13.1	23.0	0.4	531.2	428.9	11.0	46.6	5.9	7.9	61.1	12.4	492.0	0.0
1H-2, 65–80	2.2	53.0	8.19	19.8	32.5	567.4	3.4	29.7	0.5	693.6	444.5	10.8	43.1	4.5	9.6	56.6	9.1	376.3	0.3
1H-2, 135–150	2.9	67.0	8.11	23.1	32.5	566.9	0.0	34.7	0.7	751.5	428.4	10.1	40.0	4.4	9.0	71.3	7.3	511.1	6.7
1H-3, 60–72	3.7	44.0	8.21	19.2	32.2	566.4	0.0	57.2	0.9	748.8	425.3	10.3	38.0	3.5	10.9	50.4	5.4	294.4	11.1
2H-1, 60–75	4.6	36.0	8.17	14.9	32.5	566.4	7.6	38.8	0.5	709.6	423.8	10.2	39.8	4.9	8.1	73.7	8.8	499.3	3.7
2H-1, 135–150	5.3	50.0	8.05	19.2	32.2	566.9	0.3	66.3	1.0	739.4	433.1	9.5	41.4	3.9	10.6	73.3	2.6	504.6	18.6
2H-2, 65–80	6.1	54.0	8.02	19.1	32.0	566.9	0.1	71.3	1.1	732.6	415.9	9.3	42.2	4.0	10.4	77.0	1.5	453.8	20.9
2H-2, 135–150	6.8	50.0	7.97	19.0	32.8	567.9	0.0	81.3	1.3	606.2	422.9	9.1	42.3	4.4	9.6	78.1	0.0	471.7	31.0
2H-3, 60–75	7.6	54.0	7.97	18.5	32.5	564.9	0.2	71.3	1.5	628.0	416.5	8.9	33.7	4.0	8.4	75.2	0.7	444.8	25.3
2H-3, 135–150	8.3	53.0	7.99	19.1	32.5	566.4	0.1	77.2	1.5	738.3	425.2	8.9	39.3	3.5	11.3	79.2	0.3	481.9	19.8
2H-4, 65–80	9.1	58.0	8.11	19.5	32.2	564.9	0.0	73.0	1.8	647.7	388.0	8.9	37.3	3.7	10.0	76.0	0.0	470.1	29.1
2H-4, 135–150	9.8	44.0	8.00	19.7	32.5	566.9	0.0	71.3	1.9	768.8	381.1	8.4	39.5	3.7	10.8	75.9	1.5	483.5	22.5
2H-5, 135–150	11.3	46.0	7.98	18.8	32.5	564.9	0.0	40.5	1.9	649.4	414.3	9.4	29.3	4.3	6.8	79.4	0.4	466.6	31.7
2H-6, 135–150	12.8	48.0	7.84	18.4	33.0	565.4	0.0	34.7	2.0	710.9	439.1	8.4	37.9	4.9	7.8	77.5	1.2	423.9	31.5
3H-2, 135–150	16.3	44.0	7.75	18.6	33.2	565.9	0.1	22.2	2.6	703.5	404.8	8.2	40.9	4.9	8.3	71.9	2.4	436.7	34.3
3H-4, 135–150	19.3	50.0	7.80	17.8	33.2	566.9	0.1	21.3	2.9	638.6	396.9	8.3	43.7	5.5	7.9	75.2	3.1	414.5	34.4
4H-2, 130–150	25.8	38.0	8.03	19.7	33.2	566.9	0.0	14.7	2.9	271.4	401.0	7.9	39.5	5.2	7.6	83.2	0.0	395.1	20.6
5X-2, 117–142*	33.2	—	—	—	—	—	—	—	—	—	—	—	—	—	—	—	—	—	—
5X-5, 0–35*	36.2	—	—	—	—	—	—	—	—	—	—	—	—	—	—	—	—	—	—
6X-2, 125–150	42.9	18.0	8.02	7.6	32.2	569.9	2.1	3.7	2.4	299.8	417.8	7.2	33.7	7.0	4.8	82.3	0.0	416.7	11.0
6X-4, 83–96	44.9	2.0	—	—	5.0	96.4	0.4	3.7	0.3	—	—	—	—	—	—	—	—	—	—
6X-4, 83–96	44.9	3.0	—	—	31.8	556.5	0.8	1.2	2.2	—	—	—	—	—	—	—	—	—	—
6X-4, 83–96	44.9	7.0	—	—	20.0	345.4	7.3	—	1.1	172.3	260.4	4.6	22.0	5.2	4.2	43.8	4.3	209.7	5.1
7X-1, 93–133	50.8	9.0	7.99	4.6	31.7	570.7	2.1	2.8	2.2	214.8	425.0	6.6	35.2	9.1	3.9	86.3	1.6	427.0	13.2
7X-3, 74–101	53.4	7.0	—	—	12.0	570.9	3.0	2.0	0.8	298.8	413.6	6.1	33.0	10.0	3.3	92.4	1.5	317.9	14.7
7X-3, 74–101	53.4	8.5	—	—	32.0	212.1	0.0	1.2	1.9	—	—	—	—	—	—	—	—	—	—
9X-2, 0–25	70.7	34.0	8.24	2.6	30.1	563.9	5.2	1.2	1.5	180.4	425.7	5.7	26.1	17.3	1.5	91.2	0.0	415.8	13.4
9X-3, 66–91	72.9	23.0	8.17	2.7	32.1	570.0	1.2	1.2	1.7	172.9	434.7	5.9	24.8	15.0	1.7	91.3	0.0	401.4	14.4
10X-2, 0–30	80.4	7.0	—	—	32.1	570.0	0.1	1.2	1.8	363.9	413.4	5.4	25.8	17.2	1.5	87.8	0.0	407.6	14.9
12P-1, 3–14	83.8	16.0	—	—	20.0	522.0	10.8	—	—	—	—	—	—	—	—	—	—	—	—
12P-1, 14–24	83.9	8.0	—	—	30.0	522.0	9.7	—	—	—	—	—	—	—	—	—	—	—	—
311-U1326D-																			
2X-2, 128–150	91.3	23.0	8.10	6.3	32.0	564.9	0.2	4.5	2.5	238.2	421.0	5.2	33.5	8.3	4.0	89.9	3.4	274.3	15.6
2X-5, 104–144	95.6	30.0	7.94	9.0	32.2	569.9	0.2	6.2	2.7	248.0	416.1	5.5	32.4	8.4	3.9	91.5	3.0	279.1	16.0
3X-4, 61–90	103.4	4.5	—	—	32.2	570.7	0.7	—	4.7	146.3	412.8	6.9	33.9	6.1	5.5	77.3	5.9	184.5	18.2
3X-4, 90–119	103.6	2.0	—	—	21.0	367.6	1.2	—	2.9	—	—	—	—	—	—	—	—	—	—
3X-4, 90–119	103.6	17.0	—	—	32.1	567.9	0.0	6.2	4.0	196.4	418.1	6.4	36.7	5.6	6.5	80.8	6.1	226.4	18.9
4X-3, 40–106	111.4	29.0	8.23	11.8	32.0	554.1	5.3	7.0	4.0	273.4	413.1	6.1	37.3	5.2	7.2	79.0	4.2	245.7	17.6
4X-5, 126–146	114.5	14.0	—	—	21.7	352.3	3.1	4.5	3.0	186.2	280.3	3.8	23.2	3.4	6.8	47.0	0.0	146.7	10.3
5X-3, 102–150	121.3	9.0	—	—	33.2	570.6	1.7	9.5	5.8	318.7	453.3	7.5	37.6	5.1	7.4	80.2	2.6	230.9	18.7
5X-4, 115–150	122.9	17.0	7.97	16.7	33.7	574.3	0.8	9.5	5.8	316.8	396.8	6.3	32.4	4.9	6.5	80.5	3.8	243.9	17.8
6X-3, 100–113	131.1	8.0	—	—	17.0	307.7	0.4	7.0	3.3	241.3	227.8	3.1	17.8	3.4	5.3	41.5	0.0	144.3	9.3
6X-4, 90–132	132.2	23.0	8.14	17.2	32.0	564.9	0.2	12.0	6.7	452.6	429.8	7.1	34.4	5.7	6.1	80.0	3.1	248.0	18.7
7X-1, 73–96	137.4	5.0	—	—	26.2	442.2	3.5	9.5	5.2	—	—	—	—	—	—	—	—	—	—
7X-3, 0–50	139.0	28.0	8.04	16.1	33.5	572.7	1.7	10.3	6.8	443.5	428.6	7.1	34.6	6.4	5.4	85.6	6.6	267.4	21.1
8X-2, 36–86	148.4	25.0	—	—	33.7	576.9	0.9	9.5	7.6	569.1	433.8	7.0	33.9	7.6	4.5	87.3	22.8	243.9	28.1
8X-2, 86–96	148.7	3.0	—	—	25.2	405.5	5.3	—	5.8	—	—	—	—	—	—	—	—	—	—
9X-1, 84–134	157.0	31.0	—	—	33.5	576.6	2.9	11.2	7.3	796.2	438.5	6.9	32.9	8.2	4.0	84.1	25.7	283.0	26.8

Table T3 (continued).

Core, section, interval (cm)	Depth (mbsf)	Volume (mL)	pH	Alkalinity (mM)	Salinity	Cl (mM)	SO_4 (mM)	PO_4 (µM)	NH_4 (mM)	H_4SiO_4 (µM)	Cations (mM)					Trace elements (µM)			
											Na	K	Mg	Ca	Mg/Ca	Sr	Li	B	Ba
9X-4, 35–48	158.5	2.0	—	—	20.0	458.8	1.7	—	5.1	412.9	331.7	5.5	21.7	5.4	4.0	60.2	19.5	155.1	20.4
9X-4, 35–48	158.5	12.0	8.21	11.3	27.0	320.6	2.9	3.7	6.8	—	—	—	—	—	—	—	—	—	—
10X-2, 97–142	168.3	37.0	7.79	14.5	33.8	582.1	0.4	7.0	7.4	755.6	426.1	6.3	30.5	8.1	3.8	91.7	25.2	249.4	19.4
10X-6, 0–66	172.4	34.0	8.05	11.9	33.8	516.4	0.0	3.7	7.7	498.1	432.2	6.8	28.6	8.2	3.5	92.8	23.9	187.4	21.3
10X-6, 0–66	172.4	12.5	—	—	30.0	581.3	0.7	—	7.8	284.4	235.0	3.9	15.7	4.2	3.7	76.4	22.4	159.8	20.9
11X-1, 38–49	175.6	2.5	—	—	27.5	457.2	3.9	2.6	6.4	—	—	—	—	—	—	—	—	—	—
11X-1, 38–49	175.6	15.0	—	—	27.5	454.8	4.7	2.6	6.4	387.1	344.8	5.6	25.2	6.4	3.9	71.7	22.4	185.8	11.0
11X-4, 100–150	179.9	18.5	—	—	33.8	580.3	0.6	5.1	7.4	696.1	417.9	6.1	28.8	8.2	3.5	95.8	22.9	246.3	25.4
12X-1, 75–125	185.8	25.0	7.85	12.1	33.5	579.7	0.2	6.8	7.1	731.9	404.2	5.6	29.4	7.9	3.7	97.1	18.7	245.1	24.3
12X-3, 100–150	188.8	15.0	—	—	32.0	538.4	2.6	2.6	6.8	377.3	389.5	6.0	29.7	7.4	4.0	92.0	27.4	204.2	23.4
12X-3, 100–150	188.8	42.0	7.97	11.1	32.5	560.0	0.6	3.4	7.3	574.6	386.5	6.0	24.8	7.4	3.4	95.1	18.8	233.6	25.2
13X-1, 100–110	195.5	9.0	—	—	31.8	555.5	1.0	3.4	6.2	569.5	409.7	6.1	29.8	7.5	4.0	90.4	14.2	223.7	23.8
13X-1, 100–110	195.5	2.0	—	—	31.8	535.2	8.3	—	6.9	—	—	—	—	—	—	—	—	—	—
13X-4, 60–112	198.9	46.0	8.07	9.3	32.5	575.8	1.7	1.8	7.0	318.2	479.1	7.8	22.2	7.2	3.1	94.7	24.0	213.6	20.6
14X-3, 58–73	206.9	3.5	—	—	29.5	517.9	1.9	—	5.9	—	—	—	—	—	—	—	—	—	—
14X-3, 58–73	206.9	18.0	—	—	32.0	530.3	2.1	1.8	6.2	426.8	379.3	5.3	28.1	6.7	4.2	88.9	16.6	234.8	20.3
14X-5, 0–50	208.8	16.0	—	—	33.8	586.3	5.9	3.4	6.6	631.3	431.2	5.8	30.5	7.9	3.9	99.7	13.0	208.1	23.3
15X-3, 100–150	217.6	22.5	8.06	9.4	33.0	580.2	0.0	2.6	7.0	395.9	416.4	5.8	30.8	7.8	4.0	98.6	8.0	231.7	23.9
15X-5, 50–100	220.1	23.0	—	—	32.8	570.8	0.5	2.6	6.6	426.1	434.9	5.7	30.4	7.7	4.0	105.5	8.3	219.3	21.5
16X-3, 0–50	226.6	8.0	—	—	33.0	579.7	0.0	2.6	6.9	258.7	425.2	6.3	30.8	7.8	4.0	104.4	9.1	180.3	27.7
16X-5, 0–52	229.2	26.0	7.95	9.1	33.7	578.4	0.4	2.6	7.0	264.7	27.5	1.0	—	—	—	106.8	10.6	207.9	28.5
17X-3, 0–100	236.4	21.0	—	—	33.7	580.7	0.0	2.6	7.1	306.9	417.8	6.0	29.3	8.6	3.4	110.2	16.7	219.7	31.7
18X-3, 0–90	245.1	1.5	7.85	9.3	15.5	218.2	4.7	1.8	7.0	436.8	419.3	6.1	27.2	9.6	2.8	110.4	30.1	246.1	36.8
18X-3, 109–120	245.8	22.0	—	—	33.7	582.2	0.0	—	3.8	—	—	—	—	—	—	—	—	—	—
19X-2, 0–83	254.0	4.0	—	—	23.0	365.6	6.3	—	4.6	—	—	—	—	—	—	—	—	—	—
19X-2, 0–83	254.0	24.0	7.82	9.9	33.5	578.7	0.0	3.4	7.2	639.5	473.0	6.8	31.7	11.4	2.8	111.3	36.2	245.5	40.1
20X-2, 33–45	263.7	15.0	—	—	32.0	556.4	1.4	—	6.6	—	—	—	—	—	—	—	—	—	—
20X-4, 50–150	266.0	22.0	—	—	33.5	583.6	0.0	1.8	6.6	409.3	408.3	5.6	27.0	10.7	2.5	111.4	33.4	195.4	49.5
20X-6, 0–100	268.5	30.0	—	—	33.3	584.6	0.0	1.8	7.0	201.1	401.4	6.1	25.2	10.1	2.5	113.0	34.3	162.3	43.4

Notes: * = no interstitial water squeezed because of poor quality of sample. — = no data.

Table T4. Concentrations of solutes corrected for drill-fluid contamination in interstitial waters, Site U1326. (See table notes. Continued on next page.)

Core, section, interval (cm)	Depth (mbsf)	Volume (mL)	pH	Alkalinity (mM)	Salinity	Cl (mM)	SO_4 (mM)	PO_4 (µM)	NH_4 (mM)	H_4SiO_4 (µM)	Cations (mM)				Mg/Ca	Trace elements (µM)			
											Na	K	Mg	Ca		Sr	Li	B	Ba
311-U1326C-																			
1H-1, 65–80	0.7	60	7.98	6.0	33.8	559.0	21.4	7.2	0.3	385.3	436.8	11.1	46.8	8.4	5.6	77.9	14.8	567.1	0.0
1H-1, 135–150	1.4	62	8.19	13.1	33.8	562.5	13.1	23.0	0.4	531.2	428.9	11.0	46.6	5.9	7.9	61.1	12.4	492.0	0.0
1H-2, 65–80	2.2	53	8.19	19.8	32.5	567.4	3.4	29.7	0.5	693.6	444.5	10.8	43.1	4.5	9.6	56.6	9.1	376.3	0.3
1H-2, 135–150	2.9	67	8.11	23.1	32.5	566.9	0.0	34.7	0.7	751.5	428.4	10.1	40.0	4.4	9.0	71.3	7.3	511.1	6.7
1H-3, 60–72	3.7	44	8.21	19.2	32.2	566.4	0.0	57.2	0.9	748.8	425.3	10.3	38.0	3.5	10.9	50.4	5.4	294.4	11.1
2H-1, 60–75	4.6	36	8.17	14.9	32.5	566.4	7.6	38.8	0.5	709.6	423.8	10.2	39.8	4.9	8.1	73.7	8.8	499.3	3.7
2H-1, 135–150	5.3	50	8.05	19.2	32.2	566.9	0.3	66.3	1.0	739.4	433.1	9.5	41.4	3.9	10.6	73.3	2.6	504.6	18.6
2H-2, 65–80	6.1	54	8.02	19.1	32.0	566.9	0.1	71.3	1.1	732.6	415.9	9.3	42.2	4.0	10.4	77.0	1.5	453.8	20.9
2H-2, 135–150	6.8	50	7.97	19.0	32.8	567.9	0.0	81.3	1.3	606.2	422.9	9.1	42.3	4.4	9.6	78.1	0.0	471.7	31.0
2H-3, 60–75	7.6	54	7.97	18.5	32.5	564.9	0.0	71.3	1.5	628.0	416.5	8.9	33.7	4.0	8.4	75.2	0.7	444.8	25.3
2H-3, 135–150	8.3	53	7.99	19.1	32.5	566.4	0.0	77.2	1.5	738.3	425.2	8.9	39.3	3.5	11.3	79.2	0.3	481.9	19.8
2H-4, 65–80	9.1	58	8.11	19.5	32.2	564.9	0.0	73.0	1.8	647.7	388.0	8.9	37.3	3.7	10.0	76.0	0.0	470.1	29.1
2H-4, 135–150	9.8	44	8.00	19.7	32.5	566.9	0.0	71.3	1.9	768.8	381.1	8.4	39.5	3.7	10.8	75.9	1.5	483.5	22.5
2H-5, 135–150	11.3	46	7.98	18.8	32.5	564.9	0.0	40.5	1.9	649.4	414.3	9.4	29.3	4.3	6.8	79.4	0.4	466.6	31.7
2H-6, 135–150	12.8	48	7.84	18.4	33.0	565.4	0.0	34.7	2.0	710.9	439.1	8.4	37.9	4.9	7.8	77.5	1.2	423.9	31.5
3H-2, 135–150	16.3	44	7.75	18.6	33.2	565.9	0.0	22.2	2.6	703.5	404.8	8.2	40.9	4.9	8.3	71.9	2.4	436.7	34.3
3H-4, 135–150	19.3	50	7.80	17.8	33.2	566.9	0.0	21.3	2.9	638.6	396.9	8.3	43.7	5.5	7.9	75.2	3.1	414.5	34.4
4H-2, 130–150	25.8	38	8.03	19.7	33.2	566.9	0.0	14.7	2.9	271.4	401.0	7.9	39.5	5.2	7.6	83.2	0.0	395.1	20.6
5X-2, 117–142*	33.2	—	—	—	—	—	—	—	—	—	—	—	—	—	—	—	—	—	—
5X-5, 0–35*	36.2	—	—	—	—	—	—	—	—	—	—	—	—	—	—	—	—	—	—
6X-2, 125–150	42.9	18	8.02	8.0	32.0	570.7	0.0	3.9	2.6	311.5	412.9	6.9	32.1	6.7	4.8	82.0	0.0	414.2	11.9
6X-4, 83–96	44.9	2	—	—	4.6	90.1	0.0	3.7	0.4	—	—	—	—	—	—	—	—	—	—
6X-4, 83–96	44.9	3	—	—	31.7	556.5	0.0	1.2	2.3	—	—	—	—	—	—	—	—	—	—
6X-4, 83–96	44.9	7	—	—	15.1	273.1	0.0	—	1.5	179.9	186.1	2.7	11.1	3.4	3.2	29.2	0.0	128.3	6.9
7X-1, 93–133	50.8	9	7.99	4.7	31.5	571.6	0.0	3.0	2.4	219.9	420.7	6.3	33.7	9.0	3.7	86.2	0.0	425.2	14.2
7X-3, 74–101	53.4	7	—	—	9.4	572.3	0.0	2.2	0.9	316.1	405.9	5.6	30.6	9.9	3.1	93.0	0.0	302.6	16.4
7X-3, 74–101	53.4	8.5	—	—	32.0	212.1	0.0	1.2	1.9	—	—	—	—	—	—	—	—	—	—
9X-2, 0–25	70.7	34	8.24	2.7	29.2	565.0	0.0	1.4	1.9	187.0	413.8	4.6	20.0	18.8	1.1	92.1	0.0	408.3	16.3
9X-3, 66–91	72.9	23	8.17	2.7	32.0	570.5	0.0	1.2	1.8	173.8	432.8	5.7	23.6	15.2	1.6	91.5	0.0	399.4	15.0
10X-2, 0–30	80.4	7	—	—	32.1	570.0	0.0	1.2	1.8	363.9	413.4	5.4	25.8	17.2	1.5	87.8	0.0	407.6	14.9
12P-1, 3–14	83.8	16	—	—	11.4	438.9	0.0	—	—	—	—	—	—	—	—	—	—	—	—
12P-1, 14–24	83.9	8	—	—	27.8	503.3	0.0	—	—	—	—	—	—	—	—	—	—	—	—
311-U1326D-																			
2X-2, 128–150	91.3	23.0	8.10	6.3	32.0	564.9	0.0	4.5	2.5	238.2	421.0	5.2	33.5	8.3	4.0	89.9	3.4	274.3	15.6
2X-5, 104–144	95.6	30.0	7.94	9.0	32.2	570.0	0.0	6.2	2.7	248.0	416.1	5.5	32.4	8.4	3.9	91.5	3.0	279.1	16.0
3X-4, 61–90	103.4	4.5	—	—	32.1	571.0	0.0	—	4.8	146.2	411.1	6.8	33.3	6.0	5.5	77.0	5.4	177.7	18.6
3X-4, 90–119	103.6	2.0	—	—	20.4	359.2	0.0	—	3.1	—	—	—	—	—	—	—	—	—	—
3X-4, 90–119	103.6	17.0	—	—	32.1	567.9	0.0	6.2	4.0	196.4	418.1	6.4	36.7	5.6	6.5	80.8	6.1	226.4	18.9
4X-3, 40–106	111.4	29.0	8.23	14.0	31.5	553.0	0.0	8.5	4.9	301.1	398.1	5.1	33.5	4.0	8.4	77.2	0.0	199.7	21.5
4X-5, 126–146	114.5	14.0	—	—	20.2	327.3	0.0	5.0	3.3	190.6	256.1	3.0	19.5	2.6	7.6	42.2	0.0	110.0	11.6
5X-3, 102–150	121.3	9.0	—	—	33.1	571.3	0.0	10.1	6.2	329.3	451.6	7.3	36.6	4.8	7.7	79.8	1.0	217.1	19.9
5X-4, 115–150	122.9	17.0	7.97	17.1	33.7	574.7	0.0	9.7	6.0	321.2	394.6	6.2	31.8	4.8	6.6	80.3	3.2	238.4	18.2
6X-3, 100–113	131.1	8.0	—	—	16.8	304.2	0.0	7.1	3.4	242.6	224.2	3.0	17.3	3.3	5.3	40.9	0.0	140.0	9.4
6X-4, 90–132	132.2	23.0	8.14	17.2	32.0	564.9	0.0	12.0	6.7	452.6	429.8	7.1	34.4	5.7	6.1	80.0	3.1	248.0	18.7
7X-1, 73–96	137.4	5.0	—	—	25.1	426.1	0.0	10.8	6.0	—	—	—	—	—	—	—	—	—	—
7X-3, 0–50	139.0	28.0	8.04	17.0	33.4	573.5	0.0	11.0	7.2	461.6	425.4	6.8	33.3	6.1	5.5	85.5	5.3	256.2	22.4
8X-2, 36–86	148.4	25.0	—	—	33.7	577.5	0.0	9.8	7.8	583.1	432.2	6.9	33.3	7.5	4.5	87.3	22.7	237.0	29.1
8X-2, 86–96	148.7	3.0	—	—	23.1	371.0	0.0	—	7.2	—	—	—	—	—	—	—	—	—	—

Table T4 (continued).

Core, section, interval (cm)	Depth (mbsf)	Volume (mL)	pH	Alkalinity (mM)	Salinity	Cl (mM)	SO_4 (mM)	PO_4 (µM)	NH_4 (mM)	H_4SiO_4 (µM)	Cations (mM)					Trace elements (µM)			
											Na	K	Mg	Ca	Mg/Ca	Sr	Li	B	Ba
9X-1, 84–134	157.0	31.0	—	—	33.4	578.5	0.0	12.4	8.1	867.4	433.9	6.5	30.5	7.9	3.9	83.8	25.6	264.6	29.7
9X-4, 35–48	158.5	2.0	—	—	19.1	452.4	0.0	—	5.5	429.6	322.3	5.2	19.6	5.1	3.8	58.4	19.1	136.4	21.7
9X-4, 35–48	158.5	12.0	8.21	12.3	26.2	294.1	0.0	4.0	7.5	—	—	—	—	—	—	—	—	—	—
10X-2, 97–142	168.3	37.0	7.79	14.7	33.8	582.4	0.0	7.1	7.5	763.7	425.3	6.2	30.2	8.0	3.8	91.8	25.2	246.7	19.7
10X-6, 0–66	172.4	34.0	8.05	11.9	33.8	516.4	0.0	3.7	7.7	498.1	432.2	6.8	28.6	8.2	3.5	92.8	23.9	187.4	21.3
10X-6, 0–66	172.4	12.5	—	—	29.9	581.8	0.0	—	8.0	287.6	229.3	3.8	14.8	4.1	3.6	76.2	22.2	153.0	21.4
11X-1, 38–49	175.6	2.5	—	—	26.4	441.5	0.0	2.9	7.4	—	—	—	—	—	—	—	—	—	—
11X-1, 38–49	175.6	15.0	—	—	26.2	434.5	0.0	3.0	7.7	433.2	318.5	4.7	19.6	5.6	3.5	68.7	21.5	134.4	13.2
11X-4, 100–150	179.9	18.5	—	—	33.8	580.8	0.0	5.2	7.5	708.1	416.5	6.0	28.2	8.2	3.5	96.0	22.8	241.8	26.0
12X-1, 75–125	185.8	25.0	7.85	12.1	33.5	579.8	0.0	6.8	7.1	731.9	404.2	5.6	29.4	7.9	3.7	97.1	18.7	245.1	24.3
12X-3, 100–150	188.8	15.0	—	—	31.8	536.3	0.0	2.8	7.5	400.0	380.4	5.6	27.3	7.0	3.9	92.5	27.5	179.7	25.7
12X-3, 100–150	188.8	42.0	7.97	11.3	32.5	560.0	0.0	3.5	7.5	583.8	384.5	5.9	24.2	7.3	3.3	95.3	18.6	228.9	25.7
13X-1, 100–110	195.5	9.0	—	—	31.7	555.4	0.0	3.5	6.4	584.2	407.3	5.9	29.0	7.4	3.9	90.5	13.8	215.8	24.7
13X-1, 100–110	195.5	2.0	—	—	30.8	525.7	0.0	—	9.6	—	—	—	—	—	—	—	—	—	—
13X-4, 60–112	198.9	46.0	8.07	9.8	32.4	576.9	0.0	1.8	7.4	328.9	479.0	7.7	20.1	7.0	2.9	95.2	23.8	198.7	21.9
14X-3, 58–73	206.9	3.5	—	—	29.2	515.0	0.0	—	6.3	—	—	—	—	—	—	—	—	—	—
14X-3, 58–73	206.9	18.0	—	—	31.8	528.1	0.0	1.9	6.7	448.2	371.5	4.9	26.1	6.4	4.1	89.0	15.8	218.2	21.8
14X-5, 0–50	208.8	16.0	—	—	33.7	593.3	0.0	4.2	8.3	755.0	418.6	4.7	24.4	7.2	3.4	103.0	9.4	145.9	29.2
15X-3, 100–150	217.6	22.5	8.06	9.4	33.0	580.2	0.0	2.6	7.0	395.9	416.4	5.8	30.8	7.8	4.0	98.6	8.0	231.7	23.9
15X-5, 50–100	220.1	23.0	—	—	32.8	571.0	0.0	2.6	6.7	430.6	434.2	5.6	30.0	7.6	3.9	105.8	8.0	215.6	21.8
16X-3, 0–50	226.6	8.0	—	—	33.0	579.7	0.0	2.6	6.9	258.7	425.2	6.3	30.8	7.8	4.0	104.4	9.1	180.3	27.7
16X-5, 0–52	229.2	26.0	7.95	9.2	33.7	578.6	0.0	2.6	7.1	266.2	21.8	0.9	—	—	—	107.0	10.4	204.9	28.9
17X-3, 0–100	236.4	21.0	—	—	33.7	580.7	0.0	2.6	7.1	306.9	417.8	6.0	29.3	8.6	3.4	110.2	16.7	219.7	31.7
18X-3, 0–90	245.1	1.5	7.85	10.6	11.8	151.5	0.0	2.0	8.4	492.9	407.4	5.2	22.0	9.4	2.3	115.0	30.7	206.2	44.0
18X-3, 109–120	245.8	22.0	—	—	33.7	582.2	0.0	—	3.8	—	—	—	—	—	—	—	—	—	—
19X-2, 0–83	254.0	4.0	—	—	19.8	311.2	0.0	—	5.9	—	—	—	—	—	—	—	—	—	—
19X-2, 0–83	254.0	24.0	7.82	9.9	33.5	578.7	0.0	3.4	7.2	639.5	473.0	6.8	31.7	11.4	2.8	111.3	36.2	245.5	40.1
20X-2, 33–45	263.7	15.0	—	—	31.9	556.3	0.0	—	7.0	—	—	—	—	—	—	—	—	—	—
20X-4, 50–150	266.0	22.0	—	—	33.5	583.6	0.0	1.8	6.6	409.3	408.3	5.6	27.0	10.7	2.5	111.4	33.4	195.4	49.5
20X-6, 0–100	268.5	30.0	—	—	33.3	584.6	0.0	1.8	7.0	201.1	401.4	6.1	25.2	10.1	2.5	113.0	34.3	162.3	43.4

Notes: Corrections based on dissolved sulfate concentrations assuming zero sulfate concentration below the sulfate/methane interface, which at this site occurs in the uppermost ~2.5 m. * = no interstitial water squeezed because of poor quality of sample. — = no data.

Table T5. Headspace gas concentrations of hydrocarbons, Holes U1326C and U1326D. (See table note. Continued on next page.)

Core, section, interval (cm)	Depth (mbsf)	C_1/C_2	C_1 (ppmv)	C_2 (ppmv)	$C_{2=}$ (ppmv)	C_3 (ppmv)	C_1 (mM)*
311-U1326C-							
1H-1, 80–85	0.80		37	0	0	0	0.02
1H-2, 0–5	1.50		25	0	0	0	0.01
1H-2, 80–85	2.30	213	149	0.7	0	0	0.08
1H-3, 0–5	3.00		3,943	0	0	0	2.10
2H-1, 75–80	4.65		13,275	0	0	0	7.10
2H-2, 0–5	5.40		14,783	0	0	0	8.00
2H-2, 80–85	6.20		16,892	0	0	0	9.10
2H-3, 0–5	6.90	17,964	14,371	0.8	0	0	7.80
2H-3, 75–80	7.65		9,988	0	0	0	5.40
2H-4, 0–5	8.40	19,431	11,659	0.6	0	0	6.30
2H-4, 80–85	9.20	15,108	10,576	0.7	0	0	5.70
2H-5, 0–5	9.90		13,612	0	0	0	7.40
2H-6, 0–5	11.40	8,169	4,902	0.6	0	0	2.70
2H-7, 0–5	12.90		4,429	0	0	0	2.40
3H-3, 0–5	16.40		5,165	0	0.4	0	2.80
3H-5, 0–5	19.40		4,437	0	0.4	0	2.40
4H-3, 0–5	25.90	8,136	8,136	1	0	0	4.50
5X-3, 0–5	33.32		5,197	0	0	0	2.90
5X-4, 135–140	36.00		3,570	0	0	0	2.00
6X-3, 0–5	43.00	17,143	6,858	0.4	0	0	4.00
6X-4, 78–83	44.80		7,112	0	0	0	4.10
6X-4, 92–93	44.94		3,206	0	0	0	1.90
7X-2, 0–5	51.03	15,457	7,729	0.5	0	0	4.10
7X-3, 69–74	53.22		5,190	0	0	0	2.80
7X-3, 77–78	53.30	15,347	12,278	0.8	0	0	6.60
7X-3, 85–86	53.38		3,245	0	0	0	1.70
8X-1, 90–95	60.30		8,290	0	0	0	4.50
9X-2, 25–30	70.85	9,608	5,765	0.6	0	0	3.20
9X-3, 61–66	72.71		7,932	0	0	0	4.40
10X-1, 145–150	80.15		3,293	0	0	0	1.80
311-U1326D-							
2X-3, 0–5	91.40		3,086	0	0	0	1.70
2X-6, 0–5	95.84		3,494	0	0	0	2.00
3X-3, 0–5	101.10		2,891	0	0	0	1.70
3X-5, 0–5	103.79		3,443	0	0	0	2.00
4X-3, 35–40	111.05		2,723	0	0	0	1.60
4X-6, 8–13	114.65		2,989	0	0	0	1.70
5X-4, 0–5	121.54		3,147	0	0	0	1.80
5X-6, 0–5	123.60		9,163	0	0	0	5.40
6X-4, 85–90	131.98		3,161	0	0	0	1.90
6X-6, 0–5	133.45		2,540	0	0	0	1.50
7X-1, 68–73	137.28		3,037	0	0	0	1.80
7X-4, 0–5	140.19		7,553	0	0	0	4.60
8X-2, 31–36	148.11		1,842	0	0	0	1.10
8X-3, 0–5	148.76		4,060	0	0	0	2.50
9X-1, 79–84	156.69		3,725	0	0	0	2.30
9X-4, 40–45	158.51		4,388	0	0	0	2.70
9X-5, 0–5	158.59		5,549	0	0	0	3.40
10X-2, 92–97	168.02	7,222	9,389	1.3	0	0	5.90
10X-6, 0–5	172.02		3,421	0	0	0	2.20
11X-1, 41–46	175.61	5,813	8,138	1.4	0	0	5.20
12X-1, 70–75	185.50		3,448	0	0	0	2.20
12X-4, 0–5	189.05		2,922	0	0	0	1.90
13X-1, 95–100	195.35	5,452	4,362	0.8	0	0	2.90
13X-1, 103–106	195.43		2,078	0	0	0	1.40
13X-4, 55–60	198.55		2,906	0	0	0	1.90
14X-3, 65–67	206.92		5,311	0	0	0	3.60
14X-4, 0–5	207.00		6,237	0	0	0	4.20
14X-5, 50–55	209.00	7,263	4,358	0.6	0	0	2.90
15X-3, 95–100	217.31		3,785	0	0	3.3	2.60
15X-6, 0–5	220.36		3,634	0	0	3.8	2.50
16X-3, 50–55	226.80		4,148	0	0	0	2.90
16X-5, 52–57	229.42		3,556	0	0	0	2.50
17X-3, 100–105	236.90		2,031	0	0	0	1.40
17X-6, 0–5	240.34		3,666	0	0	0	2.60
18X-1, 79–84	243.39	3,595	5,752	1.6	0	0	4.10

Table T5 (continued).

Core, section, interval (cm)	Depth (mbsf)	C_1/C_2	C_1 (ppmv)	C_2 (ppmv)	$C_{2=}$ (ppmv)	C_3 (ppmv)	C_1 (mM)*
18X-2, 91–96	244.56		2,792	0	0	0	2.00
19X-1, 36–41	252.56		1,941	0	0	0	1.40
20X-2, 28–33	263.58	5,431	5,975	1.1	0	0	4.40

Note: * = dissolved residual methane obtained by the headspace equilibration method.

Table T6. Concentrations of light hydrocarbon and nonhydrocarbon gases in void gas samples, Holes U1326C and U1325D.

Core, section, interval (cm)	Depth (mbsf)	C_1/C_2	Hydrocarbons (ppmv)							Volatiles (ppmv)			
			C_1	C_2	C_3	*i*-C_4	*n*-C_4	*i*-C_5	*n*-C_5	H_2S	CO_2	O_2	N_2
311-U1326C-													
2H-2, 65–66	6.05	33,073	241,430	7.3	0	3.4	0	0	0	0	1,294	136,024	565,528
2H-6, 108–109	12.48	37,803	805,208	21.3	0	19.2	0	0.1	0	0	2,904	4,309	139,797
3H-2, 78–79	15.68	35,996	867,494	24.1	0	0.8	0	0	0	0	3,770	10,202	61,891
3H-5, 77–78	20.17	36,302	885,767	24.4	0	0.6	0.2	0	2.1	0	3,274	3,407	49,660
4H-1, 36–37	23.26	40,407	913,201	22.6	0	0	0	0	0	0	2,836	2,004	20,626
4H-3, 145–146	27.35	36,398	815,319	22.4	0	0.4	4.1	0.5	0	0	3,787	56,011	227,538
5X-2, 26–27	32.16	43,665	899,497	20.6	0	4.4	0	0	0	0	1,141	982	33,417
5X-4, 71–72	35.36	42,758	889,364	20.8	0	0	0	0	0	0	1,161	831	43,650
6X-4, 63–64	44.65	11,132	916,131	82.3	0	0	0	0	0	0	0	1,287	9,936
7X-3, 19–20	52.72	17,081	906,995	53.1	0	0	0	0	0	0	3,590	3,880	23,269
9X-2, 26–27	70.86	15,168	923,747	60.9	0	0	0	0	0	0	0	676	6,975
9X-2, 135–136	71.95	20,959	920,096	43.9	0	0.2	0	0	0	0	0	868	10,649
311-U1326D-													
2X-4, 66–67	93.56	40,092	918,100	22.9	6.6	0	0	0	0	0	0	701	19,072
2X-5, 2–3	94.42	50,343	911,206	18.1	8.9	0	0	0	0	0	3,159	923	22,465
3X-2, 148–149	101.08	57,000	461,701	8.1	0	0.5	0	0	0	0	1,218	1,812	19,850
3X-4, 35–36	102.95	59,111	756,623	12.8	0	0.3	0	0	0	0	779	29,347	135,386
4X-2, 1–2	109.21	28,657	891,223	31.1	0	0.4	0	0	0	0	688	1,903	37,344
5X-2, 1–2	118.71	26,566	895,280	33.7	3.3	0.8	0	0	0	0	781	930	18,429
5X-5, 8–9	123.12	19,309	922,961	47.8	2.5	0.3	0	0	0	0	0	851	8,005
6X-2, 140–141	129.90	20,391	917,584	45.0	3.8	1	0	0	0	0	490	728	7,541
6X-5, 46–47	132.91	26,184	921,689	35.2	6	1.7	0.2	0	0	0	823	4,596	23,187
7X-2, 11–12	137.67	33,684	902,726	26.8	12.9	2.5	0	0	0	0	2,033	2,114	21,201
7X-4, 16–17	140.35	33,523	921,869	27.5	8.9	2.1	0	0	0	0	977	612	7,850
8X-3, 1–2	148.77	20,643	918,628	44.5	10.6	2.8	0	0.7	0	0	1,450	700	10,708
9X-1, 24–25	156.14	10,733	906,926	84.5	0	1.2	0	0.8	0	0	1,622	1,422	16,114
9X-4, 4–5	158.15	16,469	918,993	55.8	8.1	3.7	0	1.9	0	0	2,989	372	7,244
10X-2, 72–73	167.82	17,256	918,034	53.2	13	3.5	0.3	1.3	0	0	1,981	990	10,230
11X-2, 140–141	177.09	15,942	916,684	57.5	13.3	2.1	0	0.9	0	0	1,820	1,722	14,318
11X-4, 57–58	179.26	39,593	926,482	23.4	17.9	2.9	0	0.5	0	0	934	422	9,977
12X-2, 40–42	186.45	22,566	925,188	41.0	22.4	2.7	0.3	0.9	0	0	812	800	10,046
13X-2, 144–145	196.94	8,658	926,421	107.0	10.6	1	0	0.7	0	0	0	840	7,602
13X-4, 62–63	198.62	21,030	925,334	44.0	34.4	3.8	0.2	1.1	0	0	839	1,051	10,250
14X-1, 26–27	204.26	11,987	925,389	77.2	28.6	3.1	0.2	0.8	0	0	511	1,183	10,268
14X-4, 137–138	208.37	16,575	933,150	56.3	35.1	3.9	0	0.7	0	0	364	609	7,239
15X-1, 104–105	214.64	26,830	912,208	34.0	52.5	7.9	0.6	1.2	0	0	658	989	9,806
15X-3, 63–64	216.99	27,612	924,992	33.5	54.6	8.4	0.5	1.1	0	0	899	1,042	10,321
16X-3, 27–28	226.57	24,808	816,199	32.9	35.7	8.4	0.9	1.2	0	0	345	339	4,189
16X-4, 93–94	228.73	23,710	934,177	39.4	30.5	9.7	0.9	1.2	0	0	869	25,997	100,111
17X-3, 136–137	237.26	23,796	839,984	35.3	25	7.1	0.7	1.1	0	0	1,618	14,125	84,535
18X-2, 88–89	244.53	7,497	919,152	122.6	0	0.4	0	0	0	0	0	6,350	26,334
18X-3, 85–86	245.46	7,476	907,581	121.4	4.7	0.3	0	0.1	0	0	0	5,054	20,943
19X-1, 10–11	252.30	6,153	230,732	37.5	0	0.4	12.1	0	0	0	429	169,219	568,907
20X-4, 1–2	265.05	11,717	928,021	79.2	15.1	2	0.3	0.4	0	0	560	745	6,199
20X-7, 1–2	269.05	12,915	932,457	72.2	14.2	1.4	0.2	0	0	0	669	668	5,675

Table T7. Concentrations of light hydrocarbons from dissociated gas hydrate, Hole U1326C.

Core, section, interval (cm)	Depth (mbsf)	C_1/C_2	C_1 (ppmv)	C_2 (ppmv)	$C_{2=}$ (ppmv)	C_3 (ppmv)
311-U1326C-						
6X-4, 63-64	44.87	10,682	386,710	36	0.7	0
7X-3, 19-20	53.30	12,167	843,193	69	1.6	0

Table T8. Concentrations of inorganic carbon, $CaCO_3$, total carbon, total organic carbon, total nitrogen, and C/N ratios in sediment, Holes U1326C and U1326D.

Core, section, interval, cm	Depth (mbsf)	Carbon (wt%)				Total nitrogen (wt%)	C/N
		Inorganic	$CaCO_3$	Total	Total organic		
311-U1326C-							
1H-1, 65–80	0.65	0.44	3.65	0.91	0.47	0.031	15.2
1H-1, 135–150	1.35	0.59	4.94	0.78	0.19	0.017	11.2
1H-2, 65–80	2.15	1.95	16.27	2.37	0.42	0.037	11.4
1H-2, 135–150	2.85	0.62	5.18	1.04	0.42	0.044	9.5
1H-3, 60–72	3.60	0.93	7.78	1.43	0.50	0.039	12.8
2H-1, 135–150	5.25	0.32	2.64	0.81	0.49	0.034	14.4
2H-2, 65–80	6.05	0.63	5.27	1.43	0.80	0.080	10.0
2H-3, 60–75	7.50	1.05	8.72	1.74	0.69	0.061	11.3
2H-3, 135–150	8.25	0.73	6.11	1.34	0.61	0.051	12.0
2H-4, 65–80	9.05	0.38	3.21	0.80	0.42	0.040	10.5
2H-5, 135–150	11.25	0.86	7.19	1.36	0.50	0.048	10.4
2H-6, 135–150	12.75	0.32	2.66	0.77	0.45	0.056	8.0
3H-2, 135–150	16.25	0.74	6.16	1.34	0.60	0.081	7.4
3H-4, 135–150	19.25	0.70	5.86	1.30	0.60	0.056	10.7
4H-2, 130–150	25.70	0.30	2.49	0.63	0.33	0.042	7.9
6X-2, 125–150	42.75	0.24	1.97	0.52	0.28	0.039	7.2
7X-3, 74–101	53.27	0.17	1.38	0.72	0.55	0.052	10.6
10X-2, 0–30	80.20	0.13	1.12	0.37	0.24	0.024	10.0
311-U1326D-							
2X-2, 125–150	91.15	0.11	0.96	0.47	0.36	0.043	8.3
3X-4, 61–90	103.21	0.31	2.62	0.61	0.30	0.030	10.1
4X-3, 40–106	111.10	0.21	1.73	0.72	0.51	0.055	9.2
5X-3, 102–150	121.06	0.14	1.17	0.54	0.40	0.044	9.0
6X-3, 100–113	131.00	0.08	0.64	0.11	0.03	0.015	2.1
7X-3, 0–50	138.74	0.23	1.95	0.61	0.38	0.066	5.8
8X-2, 36–86	148.16	0.72	6.02	1.20	0.48	0.061	7.9
9X-4, 35–48	158.46	0.26	2.17	0.75	0.49	0.062	7.9
10X-2, 97–142	168.07	0.48	4.00	1.11	0.63	0.086	7.3
11X-4, 100–150	179.69	0.25	2.07	0.68	0.43	0.054	7.9
12X-1, 75–125	185.55	0.60	5.00	1.18	0.58	0.073	8.0
13X-4, 60–112	198.60	0.14	1.14	0.23	0.09	0.013	7.2

Table T9. Perfluorocarbon tracer and fluorescent microsphere concentrations, Site U1326.

Core, section, interval (cm)	Depth (mbsf)	Detected PFT (ng/g sediment)		Detected particles (number/g sediment)		Comments
		Inner	Outer	Inner	Outer	
APC cores						
311-U1326C-						
1H-2, 85–90	2.35	ND	ND	$>0.1 \times 10^4$	0.8×10^4	Near mudline
1H-3, 0–5	3.00	BDL	0.0013	BDL	$>0.1 \times 10^4$	
4H-1, 5–6	22.95	ND	ND	$>0.1 \times 10^4$	$>0.1 \times 10^4$	Sand layer
4H-2, 0–5	24.40	BDL	BDL	BDL	BDL	
4H-3, 110–111	24.00	ND	ND	BDL	$>0.1 \times 10^4$	Sand layer
XCB cores						
311-U1326D-						
10X-3, 135–150	169.87	ND	ND	BDL	$>0.1 \times 10^4$	Gas hydrate sample
14X-1, 103–116	205.03	ND	ND	$>0.1 \times 10^4$	$>0.1 \times 10^4$	Gas hydrate sample
20X-5, 119–120	267.73	ND	ND	BDL	1.4×10^4	Biscuit
20X-5, 124–125	267.78	ND	ND	$>0.1 \times 10^4$	$>0.1 \times 10^4$	Nonbiscuit

Notes: PFT = perfluorocarbon tracers. APC = advanced piston corer, XCB = extended core barrel. ND = no data, BDL = below detection limit.

Table T10. Moisture and density, Holes U1326B, U1326C, and U1326D. (Continued on next page.)

Core, section, interval (cm)	Depth (mbsf)	Density (g/cm^3)		Porosity (%)
		Bulk	Grain	
311-U1326B-				
1H-1, 17–19	0.17	1.779	2.780	57.0
1H-1, 118–120	1.18	1.867	2.768	51.6
311-U1326C-				
1H-1, 54–56	0.54	2.036	2.753	41.5
1H-1, 58–60	0.58	1.830	2.769	53.8
1H-2, 19–21	1.69	1.834	2.742	52.8
1H-2, 30–32	1.80	1.697	2.739	60.7
1H-2, 55–57	2.05	1.754	2.817	59.3
2H-2, 3–5	5.43	2.050	2.758	40.8
2H-2, 25–27	5.65	1.953	2.738	45.8
2H-2, 48–50	5.88	1.893	2.758	49.9
2H-4, 7–9	8.47	1.882	2.771	50.9
2H-4, 53–55	8.93	1.776	2.789	57.4
2H-5, 10–12	10.00	1.722	2.746	59.5
2H-5, 56–58	10.46	1.966	2.767	46.0
2H-6, 15–17	11.55	1.853	2.754	52.1
2H-6, 75–77	12.15	1.761	2.742	57.1
2H-7, 4–6	12.94	1.797	2.746	55.1
2H-7, 49–51	13.39	1.895	2.751	49.6
3H-1, 3–5	13.43	1.943	2.739	46.4
3H-1, 133–135	14.73	1.796	2.738	55.0
3H-2, 44–46	15.34	1.776	2.740	56.2
3H-2, 123–125	16.13	1.912	2.750	48.5
3H-3, 12–14	16.52	1.781	2.755	56.3
3H-3, 71–73	17.11	1.890	2.759	50.1
3H-3, 132–134	17.72	2.059	3.768	62.3
3H-4, 35–37	18.25	1.765	2.715	56.2
3H-5, 34–36	19.74	1.794	2.765	55.8
3H-5, 75–77	20.15	1.871	2.705	49.6
3H-5, 120–122	20.60	2.201	3.710	56.2
3H-5, 138–140	20.78	1.807	2.718	53.8
3H-6, 97–99	21.87	1.780	2.691	54.6
4H-1, 10–12	23.00	2.021	2.757	42.5
4H-1, 48–50	23.38	2.552	3.828	45.5
4H-1, 99–101	23.89	1.925	2.768	48.3
4H-1, 118–120	24.08	2.116	2.728	35.9
4H-3, 17–19	26.07	1.916	2.780	49.2
4H-3, 88–90	26.78	2.104	2.741	37.1
4H-3, 142–144	27.32	1.934	2.741	47.0
4H-4, 6–8	27.46	2.006	2.764	43.6
5X-1, 16–18	30.56	1.792	2.795	56.7
5X-1, 121–123	31.61	1.795	2.782	56.2
5X-3, 30–32	33.62	1.842	2.774	53.3
5X-3, 105–107	34.37	1.837	2.751	52.9
5X-4, 34–36	34.99	1.905	2.765	49.4
5X-4, 122–124	35.87	1.920	2.782	49.0
6X-1, 25–27	40.25	1.850	2.783	53.1
6X-1, 129–131	41.29	1.871	2.755	51.1
6X-3, 17–19	43.17	1.996	2.752	43.7
6X-3, 76–78	43.76	1.820	2.718	53.0
6X-4, 4–6	44.06	1.949	2.760	46.7
6X-4, 35–37	44.37	2.103	2.830	40.3
6X-4, 63–65	44.65	2.059	2.747	39.9
6X-4, 86–88	44.88	2.213	2.843	34.7
6X-5, 12–13	45.10	2.097	2.754	38.0
6X-5, 66–68	45.64	1.933	2.725	46.6
7X-2, 18–20	51.21	1.868	2.741	50.8
7X-2, 117–119	52.20	1.951	2.874	49.9
7X-3, 30–32	52.83	1.995	2.684	41.5
7X-3, 58–60	53.11	1.888	2.745	49.8
7X-3, 79–81	53.32	2.005	2.823	45.5
8X-1, 23–25	59.63	1.888	2.709	48.7
8X-1, 70–72	60.10	1.950	2.759	46.6
9X-2, 32–34	70.92	1.927	2.748	47.6
9X-2, 82–84	71.42	1.983	2.747	44.3
9X-2, 98–100	71.58	1.964	2.739	45.2
9X-3, 10–12	72.20	1.978	2.796	46.2
9X-4, 26–28	73.42	2.040	2.800	42.8
10X-1, 12–14	78.82	2.025	3.267	55.4
10X-1, 51–53	79.21	2.056	2.760	40.5
10X-1, 57–59	79.27	1.872	2.845	53.4
10X-1, 140–142	80.10	2.003	2.894	47.6
311-U1326D-				
2X-1, 38–70	88.78	1.987	2.902	48.7
2X-1, 39–41	88.79	1.892	2.792	50.9
2X-1, 118–120	89.58	1.925	2.784	48.8
2X-3, 29–31	91.69	1.934	2.774	48.0
2X-3, 115–117	92.55	1.947	2.747	46.4
2X-4, 23–25	93.13	1.900	2.781	50.1
2X-4, 125–127	94.15	1.902	2.747	49.0
2X-5, 23–25	94.63	1.969	2.761	45.6
2X-5, 89–91	95.29	1.885	2.779	51.0
2X-6, 18–20	96.02	1.904	2.734	48.5
2X-6, 78–80	96.62	1.935	2.699	45.6
3X-1, 86–88	98.96	2.059	2.750	40.0
3X-1, 124–126	99.34	2.056	2.758	40.5
3X-3, 12–14	101.22	2.008	2.776	43.8
3X-4, 25–27	102.85	1.944	2.764	47.1
3X-5, 10–12	103.89	1.955	2.733	45.5
3X-5, 30–32	104.09	2.033	2.763	42.0
4X-1, 37–39	108.07	1.790	2.775	56.3
4X-1, 123–125	108.93	1.832	2.755	53.4
4X-3, 27–29	110.97	1.902	2.776	49.9
4X-4, 95–97	112.71	2.059	2.763	40.5
4X-4, 128–130	113.04	1.876	2.752	50.7
4X-5, 5–7	113.16	1.878	2.753	50.6
4X-5, 54–56	113.65	1.994	2.769	44.4
4X-5, 102–104	114.13	1.980	2.764	45.1
4X-6, 16–18	114.73	1.938	2.783	48.0
5X-1, 63–65	117.93	1.898	2.809	51.0
5X-1, 113–115	118.43	1.862	2.770	52.0
5X-2, 68–70	119.38	1.892	2.854	52.6
5X-2, 90–92	119.60	1.902	2.833	51.5
5X-4, 61–63	122.15	1.954	2.806	47.8
5X-4, 110–112	122.64	2.053	2.789	41.7
5X-5, 22–24	123.26	2.113	2.761	37.3
5X-6, 23–25	123.83	2.017	2.781	43.5
6X-1, 53–55	127.53	2.007	2.780	44.0
6X-1, 114–116	128.14	1.843	2.732	52.1
6X-3, 21–23	130.21	1.985	2.760	44.6
6X-3, 80–82	130.80	1.895	2.779	50.4
6X-4, 63–65	131.76	2.002	2.776	44.2
6X-5, 22–24	132.67	2.126	2.806	38.1
6X-6, 79–81	134.24	1.979	2.761	45.0
7X-1, 18–20	136.78	1.826	2.743	53.3
7X-1, 66–68	137.26	2.008	2.749	43.0
7X-3, 57–59	139.31	1.919	2.788	49.3
7X-3, 121–123	139.95	1.947	2.753	46.6
7X-4, 24–123	140.43	1.970	2.783	46.2
7X-4, 125–127	141.44	1.988	2.785	45.2
8X-2, 1–3	147.81	1.848	2.719	51.4
8X-3, 46–48	149.22	1.798	2.772	55.7
8X-3, 115–117	149.91	1.792	2.751	55.5
8X-4, 11–13	150.25	2.086	2.768	39.1
9X-1, 43–45	156.33	1.787	2.646	53.0
9X-2, 28–30	157.52	1.928	2.692	45.8
9X-3, 5–7	157.76	1.762	2.690	55.7
9X-4, 27–29	158.38	1.922	2.710	46.7
10X-1, 36–38	165.96	1.933	2.705	45.9
10X-1, 124–126	166.84	1.800	2.739	54.8
10X-2, 22–24	167.32	1.968	2.749	45.3
10X-2, 73–75	167.83	2.111	2.736	36.5
10X-3, 34–36	168.86	2.048	2.749	40.7
10X-3, 125–127	169.77	2.089	2.728	37.5
10X-4, 24–26	170.26	1.897	2.694	47.7

Table T10 (continued).

Core, section, interval (cm)	Depth (mbsf)	Density (g/cm^3)		Porosity (%)
		Bulk	Grain	
10X-4, 76–78	170.78	2.106	2.754	37.5
11X-1, 19–21	175.39	1.990	2.739	43.7
11X-2, 22–24	175.91	1.834	2.805	54.5
11X-2, 101–103	176.70	1.937	2.809	48.8
11X-4, 22–24	178.91	2.115	2.737	36.3
11X-4, 78–80	179.47	1.848	2.759	52.5
11X-5, 30–32	180.49	1.952	2.797	47.7
11X-5, 105–107	181.24	1.906	2.823	51.0
14X-4, 113–115	208.13	2.039	2.790	42.5
14X-5, 91–93	209.41	1.951	2.796	47.7
14X-6, 51–53	210.01	1.885	2.723	49.3
15X-1, 74–76	214.34	1.973	2.810	46.9
15X-2, 91–93	215.93	1.981	2.764	45.0
15X-3, 19–21	216.55	2.042	2.809	42.9
15X-3, 88–90	217.24	2.068	2.734	39.0
15X-5, 6–8	219.42	1.940	2.768	47.5
15X-6, 38–40	220.74	2.100	2.787	39.0
16X-1, 35–37	223.65	1.923	2.753	48.0
16X-1, 119–121	224.49	1.999	2.785	44.6
16X-3, 78–80	227.08	2.054	2.785	41.5

Table T11. Compressional wave velocity, Holes U1326B and U1326C.

Core, section, interval (cm)	Depth (mbsf)	Velocity (m/s)		
		PWS1	PWS2	PWS3
311-U1326B-				
1H-1, 4	0.04	1589.9		
1H-1, 4	0.04			1487.1
1H-1, 69	0.69	1549.3		
1H-1, 69	0.69		1556.9	
1H-1, 69	0.69			1547.3
1H-1, 120	1.20			1503.6
311-U1326C-				
1H-2, 45	1.95	1537.2		
1H-2, 45	1.95			1517.2
1H-2, 59	2.09			1570.9

Note: PWS = *P*-wave sensor.

Table T12. Torvane shear strength, Holes U1326C and U1326D. (See table note. Continued on next page.)

Core, section, interval (cm)	Depth (mbsf)	Torvane shear strength (kPa)	Torvane size
311-U1326C-			
1H-2, 61–63	2.11	31	M
2H-2, 16–18	5.56	15	M
2H-2, 51–53	5.91	51	M
2H-4, 12–14	8.52	60	M
2H-4, 48–50	8.88	75	M
2H-5, 18–20	10.08	83	M
2H-5, 51–53	10.41	82	M
2H-6, 10–12	11.50	80	M
2H-7, 11–13	13.01	75	M
2H-7, 41–43	13.31	65	M
2H-2, 10–12	5.50	10	S
2H-2, 42–44	5.82	70	S
2H-4, 15–17	8.55	80	S
2H-4, 44–46	8.84	92.5	S
2H-5, 14–16	10.04	67.5	S
2H-5, 48–50	10.38	110	S
2H-6, 19–21	11.59	87.5	S
2H-6, 53–55	11.93	80	S
2H-7, 15–17	13.05	100	S
3H-1, 9–11	13.49	39	M
3H-1, 93–95	14.33	67	M
3H-1, 131–132	14.71	62	M
3H-1, 6–8	13.46	30	S
3H-1, 88–90	14.28	72.5	S
3H-1, 137–139	14.77	85	S
3H-2, 40–42	15.30	75	S
3H-2, 121–123	16.11	55	S
3H-2, 48–50	15.38	62	M
3H-2, 119–121	16.09	37	M
3H-3, 17–19	16.57	80	M
3H-3, 129–131	17.69	73	M
3H-3, 20–21	16.60	35	M
3H-3, 134–136	17.74	23	M
3H-4, 39–41	18.29	20	M
3H-4, 39–41	18.29	63	M
3H-5, 38–40	19.78	75	M
3H-5, 83–85	20.23	86	M
3H-5, 142–144	20.82	85	M
3H-5, 33–35	19.73	62.5	S
3H-5, 90–92	20.30	95	S
3H-5, 135–137	20.75	100	S
3H-6, 45–47	21.35	97.5	S
3H-6, 96–98	21.86	105	S
3H-6, 48–50	21.38	75	M
3H-6, 105–107	21.95	75	M
4H-1, 45–47	23.35	5	M
4H-1, 94–96	23.84	70	M
4H-2, 35–37	24.75	78	M
5X-1, 21–23	30.61	19	M
5X-1, 129–131	31.69	25	M
5X-3, 37–39	33.69	24	M
5X-3, 108–110	34.40	37	M
5X-4, 38–40	35.03	55	M
5X-4, 112–114	35.77	49	M
5X-4, 41–43	35.06	55	S
5X-4, 115–117	35.80	70	S
6X-1, 33–35	40.33	27	M
6X-1, 126–128	41.26	50	M
6X-3, 22–24	43.22	74	M
6X-3, 81–83	43.81	36	M
6X-4, 9–11	44.11	16	M
6X-4, 30–32	44.32	16	M
6X-4, 59–61	44.61	13	M
6X-5, 18–20	45.16	70	M
6X-1, 121–123	41.21	55	S
6X-3, 12–14	43.12	82.5	S
6X-3, 71–73	43.71	42.5	S
6X-4, 16–18	44.18	40	S
6X-5, 22–24	45.20	97.5	S
6X-5, 73–75	45.71	125	S
7X-2, 73–75	51.76	56	M
7X-2, 90–92	51.93	75	S
7X-3, 67–69	53.20	56	M
7X-3, 52–54	53.05	55	S
9X-2, 85–87	71.45	37	M
9X-2, 93–95	71.53	20	S
9X-3, 53–55	72.63	37	M
9X-3, 40–41	72.50	45	S
9X-4, 91–93	74.07	83	M
9X-4, 54–56	73.70	105	S
10X-1, 98–100	79.68	32	M
10X-1, 26–28	78.96	47.5	S
311-U1326D-			
2X-1, 45–47	88.85	41	M
2X-1, 135–137	89.75	82	M
2X-1, 112–114	89.52	13	M
2X-3, 35–37	91.75	58	M
2X-3, 119–121	92.59	73	M
2X-4, 20–22	93.10	77	M
2X-5, 19–21	94.59	69	M
2X-5, 84–86	95.24	80	M
2X-6, 27–29	96.11	92	M
2X-6, 74–76	96.58	89	M
2X-1, 49–51	88.89	47.5	S
2X-1, 141–143	89.81	95	S
2X-3, 38–40	91.78	82.5	S
2X-3, 119–121	92.59	82.5	S
2X-4, 132–134	94.22	112.5	S
2X-5, 28–30	94.68	130	S
2X-5, 80–82	95.20	122.5	S
2X-6, 29–31	96.13	97.5	S
2X-6, 81–83	96.65	100	S
3X-1, 52–55	98.62	28	M
3X-1, 141–143	99.51	38	M
3X-2, 19–21	99.79	175	S
3X-2, 65–67	100.25	200	S
3X-2, 109–111	100.69	202.5	S
3X-4, 14–16	102.74	202.5	S
3X-4, 51–53	103.11	155	S
3X-5, 6–8	103.85	210	S
3X-5, 36–38	104.15	237.5	S
3X-5, 53–55	104.32	225	S
4X-1, 33–35	108.03	22	M
4X-1, 120–122	108.90	30	M
4X-3, 32–34	111.02	63	M
4X-4, 24–26	112.00	65	M
4X-4, 85–86	112.61	62	M
4X-4, 118–120	112.94	42	M
4X-5, 11–13	113.22	48	M
4X-5, 50–52	113.61	52	M
4X-5, 25–27	113.36	66	M
4X-1, 42–44	108.12	45	S
4X-1, 128–130	108.98	37.5	S
4X-3, 30–32	111.00	62.5	S
4X-4, 28–30	112.04	62.5	S
4X-4, 99–101	112.75	25	S
4X-4, 117–119	112.93	55	S
4X-5, 9–11	113.20	50	S
4X-5, 48–50	113.59	82.5	S
4X-6, 28–30	114.85	65	S
5X-1, 37.5–39	117.68	35	M
5X-1, 66–68	117.96	37.5	S
5X-2, 28–30	118.98	49	M
5X-2, 65–67	119.35	62.5	S
5X-4, 83–85	122.37	41	M
5X-4, 91–93	122.45	50	S
5X-5, 10–12	123.14	11	M

Table T12 (continued).

Core, section, interval (cm)	Depth (mbsf)	Torvane shear strength (kPa)	Torvane size
5X-5, 2–4	123.06	12.5	S
5X-6, 82–84	124.42	60	M
5X-6, 79–81	124.39	90	S
6X-1, 101–103	128.01	20	M
6X-1, 117–119	128.17	40	S
6X-3, 30–32	130.30	25	M
6X-3, 56–58	130.56	57.5	S
6X-4, 35–37	131.48	75	M
6X-4, 32–34	131.45	100	S
6X-5, 73–75	133.18	48	M
6X-5, 77–79	133.22	35	S
6X-6, 36–38	133.81	36	M
6X-6, 28–30	133.73	45	S
7X-4, 1.4–1.6	140.20	57.5	S
7X-4, 107–109	141.26	48	M
8X-2, 20–22	148.00	31	M
8X-2, 25–26	148.05	72.5	S
8X-3, 81–83	149.57	40	M
8X-3, 93–95	149.69	67.5	S
8X-4, 18–20	150.32	25	M
8X-4, 24–26	150.38	57.5	S
9X-1, 30–32	156.20	20	M
9X-4, 13–15	158.24	27	M
9X-4, 10–12	158.21	25	S
10X-1, 54–56	166.14	25	M
10X-1, 118–120	166.78	43	M
10X-2, 26–28	167.36	47	M
10X-2, 66–68	167.76	23	M
10X-4, 23–25	170.25	54	M
10X-4, 84–86	170.86	60	M
10X-3, 29–31	168.81	30	M
10X-2, 30–32	167.40	60	S
10X-2, 76–78	167.86	25	S
10X-3, 25–28	168.77	37.5	S
10X-3, 129–131	169.81	50	S
10X-4, 91–93	170.93	40	S
11X-1, 24–26	175.44	10	M
11X-2, 102–104	176.71	67	M
11X-4, 15–17	178.84	33	M
11X-5, 25–27	180.44	95	S
11X-5, 102–104	181.21	177.5	S
12X-1, 14–16	184.94	25	M
12X-1, 42–44	185.22	28	M
12X-2, 26–28	186.31	70	M
12X-2, 103–105	187.08	77	M
12X-4, 53–55	189.58	57	M
12X-5, 32–34	190.04	15	M
12X-2, 26–28	186.31	70	S
12X-2, 91–93	186.96	65	S
12X-4, 23–25	189.28	80	S
12X-4, 50–52	189.55	55	S
12X-5, 22–24	189.94	42.5	S
13X-1, 36–38	194.76	45	M
13X-3, 15–17	197.15	20	M
13X-4, 37–39	198.37	25	M
14X-1, 62–64	204.62	25	M
14X-3, 13–15	206.40	41	M
14X-4, 119–121	208.19	40	M
14X-5, 95–97	209.45	50	M
14X-6, 46–48	209.96	95	S
15X-1, 65–67	214.25	100	S
15X-2, 96–98	215.98	122.5	S
15X-3, 23–25	216.59	92.5	S
15X-3, 81–83	217.17	80	S
15X-5, 2–4	219.38	32.5	S
15X-6, 36–38	220.72	87.5	S
16X-1, 112–114	224.42	90	S
16X-3, 75–77	227.05	85	S
16X-4, 12–14	227.92	125	S
16X-4, 89–91	228.69	162.5	S
16X-5, 78–80	229.68	167.5	S
17X-1, 115–117	234.05	37.5	S
17X-3, 129–131	237.19	82.5	S
17X-4, 36–38	237.76	62.5	S
17X-5, 75–77	239.65	82.5	S
17X-6, 53–55	240.87	70	S
18X-2, 17–19	243.82	45	S
20X-3, 30–32	264.05	50	S
20X-4, 31–33	265.35	37.5	S
20X-5, 49–51	267.03	22	M
20X-7, 44–46	269.48	75	S

Note: L = large (4.8 cm diameter), M = medium (2.5 cm diameter), S = small (1.9 cm diameter).

Table T13. AVS shear strength, Holes U1326C and U1326D.

Core, section, interval (cm)	Depth (mbsf)	Vane size	Shear strength (kPa) Peak	Residual
311-U1326C-				
1H-2, 33	1.83	B	26.7	13.4
2H-1, 46	4.36	B	42.0	37.2
2H-2, 34	5.74	B	45.0	10.4
2H-5, 17	10.07	B	61.5	38.2
2H-6, 35	11.75	B	72.2	28.0
2H-7, 8	12.98	B	81.9	33.5
3H-1, 56	13.96	B	31.3	26.0
3H-1, 91	14.31	B	47.2	35.2
3H-2, 59	15.49	B	52.3	35.5
3H-2, 109	15.99	B	59.0	30.1
3H-3, 27	16.67	B	74.8	51.8
3H-3, 111	17.51	B	71.9	53.3
3H-4, 33	18.23	B	66.1	50.5
3H-5, 32	19.72	B	60.7	44.5
3H-5, 134	20.74	B	74.2	45.4
3H-6, 39	21.29	B	85.6	48.9
3H-6, 102	21.92	B	63.7	47.2
4H-1, 79	23.69	B	65.4	19.5
4H-3, 32	26.22	B	44.2	26.2
5X-1, 119	31.59	A	31.5	27.3
5X-3, 114	34.46	A	50.3	39.4
5X-4, 31	34.96	A	59.4	50.3
5X-4, 76	35.41	A	56.2	44.1
6X-1, 110	41.10	A	80.9	44.3
6X-3, 33	43.33	A	76.5	62.9
6X-4, 64	44.66	A	7.0	4.7
6X-5, 14	45.12	A	109.1	67.6
7X-2, 88	51.91	A	65.0	49.9
7X-2, 130	52.33	A	44.1	35.9
8X-1, 80	60.20	A	7.2	5.6
9X-2, 58	71.18	B	35.2	20.7
9X-3, 30	72.40	B	43.8	19.2
9X-4, 40	73.56	B	84.8	21.9
10X-1, 24	78.94	B	22.1	12.7
311-U1326D-				
2X-1, 138	89.78	A	72.7	46.9
2X-3, 11	91.51	A	87.2	47.1
2X-4, 137	94.27	A	71.6	55.5
2X-5, 31	94.71	A	103.3	70.9
2X-6, 59	96.43	A	84.4	60.1
2X-6, 37	96.21	A	115.6	79.5
3X-1, 71	98.81	A	6.3	2.8
3X-3, 61	101.71	A	121.7	82.5
3X-4, 21	102.81	A	155.7	78.3
3X-5, 36	104.15	A	345.2	110.0
3X-5, 46	104.25	A	219.1	114.7
3X-5, 24	104.03	A	171.6	126.8
4X-1, 56	108.26	A	25.2	22.4
4X-3, 25	110.95	A	55.7	46.9
4X-4, 60	112.36	A	88.6	65.5
4X-5, 33	113.44	A	74.8	63.4
4X-6, 32	114.89	A	66.4	53.4
5X-1, 104	118.34	B	21.6	12.9
5X-2, 97	119.67	B	36.9	11.0
5X-4, 45	121.99	B	36.7	15.6
5X-5, 7	123.11	B	18.9	7.6
5X-6, 73	124.33	B	56.2	13.9
6X-1, 68	127.68	B	21.2	9.2
6X-3, 59	130.59	B	42.8	16.3
6X-4, 42	131.55	B	35.7	16.3
6X-5, 56	133.01	B	58.6	15.6
6X-6, 33	133.78	B	49.1	19.0
7X-3, 117	139.91	B	33.0	13.9
7X-4, 41	140.60	B	31.4	11.7
8X-2, 14	147.94	B	34.7	12.2
8X-3, 86	149.62	B	41.5	8.3
8X-4, 37	156.32	B	83.2	18.0
9X-1, 42	158.32	B	11.9	–0.7
9X-4, 21	167.61	B	38.1	17.8
10X-2, 51	168.69	B	43.0	34.7
10X-3, 17	170.72	B	53.3	32.8
10X-4, 70	176.53	B	67.6	41.8
11X-2, 84	178.82	A	23.3	20.5
11X-4, 13	180.42	A	19.3	18.6
11X-5, 23	181.31	A	90.4	33.6
11X-5, 112	185.07	A	203.0	86.5
12X-1, 27	186.43	A	24.0	16.8
12X-2, 38	189.35	A	81.3	46.6
12X-4, 30	190.41	A	31.0	24.2
12X-5, 69	194.66	A	44.1	15.6
13X-1, 26	207.30	A	58.3	28.2
14X-4, 30	207.95	A	48.5	38.7
14X-4, 95	210.01	A	56.6	35.7
14X-6, 51	216.08	A	117.9	85.5
15X-2, 106	216.95	A	107.7	85.3
15X-3, 59	219.61	A	51.0	42.9
15X-5, 25	220.62	A	96.3	75.1
15X-6, 26	226.93	A	75.3	64.8
16X-3, 63	228.02	A	110.3	99.8
16X-4, 22	229.11	A	96.7	75.5
16X-5, 21	234.12	A	104.2	48.9
17X-1, 122	237.30	A	31.2	4.4
17X-3, 140	238.15	A	72.7	21.9
17X-4, 75	239.76	A	136.8	46.6
17X-5, 86	240.50	A	108.9	38.2
17X-6, 16	243.90	A	115.8	28.4
18X-2, 25	263.93	A	42.7	4.2
20X-3, 18	267.10	A	86.7	4.7
20X-5, 56	269.40	B	62.3	17.3
20X-7, 36		A	76.9	16.1

Notes: A = small vane, B = medium vane. AVS values were calibrated for the spring constant used to calculate shear strength.

Table T14. Contact resistivity, Holes U1326B, U1326C, and U1326D. (Continued on next two pages.)

Core, section, interval (cm)	Depth (mbsf)	Resistivity (Ωm)
Perpendicular		
311-U1326B-		
1H-1, 8	0.08	0.513
1H-1, 18	0.18	0.539
1H-1, 28	0.28	0.572
1H-1, 38	0.38	0.671
1H-1, 48	0.48	0.522
1H-1, 49	0.49	0.499
1H-1, 54	0.54	0.645
1H-1, 58	0.58	0.566
1H-1, 59	0.59	0.594
1H-1, 62	0.62	0.632
1H-1, 68	0.68	0.594
1H-1, 78	0.78	0.555
1H-1, 88	0.88	0.493
1H-1, 98	0.98	0.640
1H-1, 108	1.08	0.545
1H-1, 118	1.18	0.619
1H-1, 128	1.28	0.562
1H-1, 138	1.38	0.650
311-U1326C-		
1H-2, 7	1.57	0.476
1H-2, 13	1.63	0.492
1H-2, 17	1.67	0.618
1H-2, 23	1.73	0.605
1H-2, 33	1.83	0.482
1H-2, 43	1.93	0.478
1H-2, 53	2.03	0.572
1H-2, 63	2.13	0.455
2H-2, 5	5.45	0.891
2H-2, 9	5.49	0.638
2H-2, 11	5.51	1.125
Parallel		
311-U1326C-		
2H-2, 14	5.54	0.758
2H-2, 17	5.57	0.973
2H-2, 21	5.61	0.800
2H-2, 26	5.66	1.112
2H-2, 38	5.78	0.750
2H-2, 50	5.90	0.833
2H-2, 61	6.01	0.838
2H-4, 4	8.44	0.869
2H-4, 8	8.48	0.892
2H-4, 18	8.58	0.582
2H-4, 19	8.59	0.869
2H-4, 24	8.64	0.760
2H-4, 34	8.74	0.874
2H-4, 37	8.77	0.960
2H-4, 44	8.84	0.968
2H-4, 50	8.90	0.881
2H-4, 54	8.94	0.960
2H-4, 64	9.04	0.851
2H-5, 7	9.97	0.845
2H-5, 12	10.02	0.888
2H-5, 17	10.07	1.004
2H-5, 27	10.17	0.985
2H-5, 31	10.21	0.943
2H-5, 37	10.27	0.817
2H-5, 43	10.33	0.864
2H-5, 47	10.37	0.889
2H-5, 57	10.47	1.075
2H-5, 60	10.50	1.114
2H-5, 67	10.57	1.011
2H-5, 77	10.67	1.143
2H-5, 84	10.74	0.962
2H-6, 7	11.47	1.177
2H-6, 12	11.52	1.100
2H-6, 17	11.57	1.043
2H-6, 21	11.61	1.075
2H-6, 30	11.70	0.912
2H-6, 36	11.76	0.953
2H-6, 45	11.85	0.925
2H-6, 50	11.90	0.913
2H-6, 59	11.99	1.022
2H-6, 67	12.07	1.093
2H-6, 75	12.15	0.855
2H-7, 5	12.95	0.923
2H-7, 10	13.00	0.829
2H-7, 15	13.05	0.964
2H-7, 28	13.18	0.989
2H-7, 42	13.32	1.023
2H-7, 52	13.42	0.870
3H-1, 6	13.46	1.105
3H-1, 14	13.54	0.839
3H-1, 39	13.79	0.946
3H-1, 45	13.85	0.777
3H-1, 55	13.95	0.906
3H-1, 62	14.02	0.980
3H-1, 71	14.11	0.977
3H-1, 85	14.25	0.807
3H-1, 91	14.31	1.009
3H-1, 101	14.41	1.003
3H-1, 113	14.53	0.847
3H-1, 123	14.63	0.993
3H-1, 136	14.76	0.840
3H-1, 146	14.86	0.818
3H-2, 6	14.96	1.121
3H-2, 16	15.06	0.835
3H-2, 26	15.16	0.837
3H-2, 36	15.26	0.780
3H-2, 46	15.36	0.939
3H-2, 56	15.46	0.926
3H-2, 66	15.56	0.879
3H-2, 76	15.66	0.854
3H-2, 86	15.76	0.787
3H-2, 96	15.86	0.856
3H-2, 105	15.95	1.094
3H-3, 4	16.44	0.852
3H-3, 14	16.54	0.746
3H-3, 24	16.64	0.754
3H-3, 34	16.74	0.838
3H-3, 42	16.82	0.950
3H-3, 52	16.92	0.837
3H-3, 62	17.02	0.916
3H-3, 72	17.12	1.016
3H-3, 86	17.26	0.782
3H-3, 96	17.36	0.909
3H-3, 106	17.46	0.857
3H-3, 116	17.56	0.919
3H-3, 126	17.66	0.953
3H-3, 136	17.76	0.890
3H-4, 6	17.96	0.796
3H-4, 16	18.06	0.805
3H-4, 26	18.16	0.768
3H-4, 36	18.26	0.793
3H-4, 48	18.38	0.852
3H-5, 12	19.52	0.833
3H-5, 26	19.66	0.765
3H-5, 36	19.76	0.788
3H-5, 46	19.86	0.917
3H-5, 53	19.93	0.781
3H-5, 63	20.03	0.995
3H-5, 77	20.17	0.949
3H-5, 87	20.27	1.068
3H-5, 97	20.37	0.873
3H-5, 128	20.68	0.842
3H-5, 129	20.69	1.655
3H-5, 138	20.78	1.206
3H-5, 148	20.88	0.944
3H-6, 5	20.95	0.995
3H-6, 15	21.05	1.474
3H-6, 23	21.13	1.318
3H-6, 33	21.23	1.171
3H-6, 43	21.33	1.127
3H-6, 53	21.43	0.958
3H-6, 59	21.49	0.803
3H-6, 69	21.59	0.917
3H-6, 78	21.68	1.310
3H-6, 93	21.83	1.349
3H-6, 103	21.93	0.928
3H-6, 116	22.06	0.929
4H-1, 4	22.94	0.777
4H-1, 13	23.03	0.944
4H-1, 23	23.13	1.446
4H-1, 48	23.38	0.978
4H-1, 58	23.48	1.424
4H-1, 76	23.66	1.661
4H-1, 92	23.82	0.959
4H-1, 102	23.92	0.990
4H-1, 118	24.08	1.583
4H-1, 129	24.19	1.124
4H-1, 138	24.28	1.346
4H-1, 143	24.33	1.098
4H-3, 7	25.97	2.024
4H-3, 8	25.98	1.089
4H-3, 17	26.07	1.971
4H-3, 18	26.08	1.829
4H-3, 18	26.08	1.025
4H-3, 25	26.15	1.990
4H-3, 28	26.18	1.486
4H-3, 31	26.21	2.183
4H-3, 32	26.22	1.159
4H-3, 39	26.29	2.393
4H-3, 39	26.29	1.243
4H-3, 47	26.37	1.184
4H-3, 48	26.38	2.223
4H-3, 58	26.48	1.451
4H-3, 59	26.49	1.155
4H-3, 69	26.59	1.204
4H-3, 70	26.60	1.573
4H-3, 73	26.63	1.092
4H-3, 77	26.67	1.974
4H-3, 84	26.74	1.144
4H-3, 85	26.75	1.568
4H-3, 87	26.77	1.242
4H-3, 88	26.78	1.265
4H-3, 94	26.84	1.238
4H-3, 94	26.84	1.168
4H-3, 104	26.94	1.179
4H-3, 106	26.96	1.146
4H-3, 128	27.18	1.196
4H-3, 137	27.27	1.288
4H-3, 142	27.32	1.495
4H-4, 7	27.47	1.242
4H-4, 17	27.57	1.169
5X-1, 5	30.45	0.882
5X-1, 15	30.55	0.761
5X-1, 25	30.65	0.700
5X-1, 45	30.85	0.822
5X-1, 55	30.95	1.013
5X-1, 72	31.12	1.038
5X-1, 82	31.22	0.831
5X-1, 92	31.32	0.710
5X-1, 105	31.45	1.025
5X-1, 118	31.58	0.895
5X-1, 130	31.70	0.842
5X-1, 145	31.85	0.784
5X-3, 10	33.42	0.773
5X-3, 20	33.52	0.671
5X-3, 33	33.65	0.816
5X-3, 43	33.75	0.851
5X-3, 61	33.93	0.941
5X-3, 71	34.03	0.685
5X-3, 92	34.24	0.821
5X-3, 106	34.38	0.901
5X-3, 116	34.48	0.936
5X-3, 125	34.57	0.909
5X-4, 6	34.71	1.095
5X-4, 16	34.81	0.997
5X-4, 26	34.91	0.934
5X-4, 36	35.01	0.930
5X-4, 46	35.11	0.884
5X-4, 53	35.18	1.022
5X-4, 68	35.33	0.978
5X-4, 78	35.43	0.888
5X-4, 88	35.53	0.873
5X-4, 109	35.74	0.852
5X-4, 123	35.88	0.869
5X-4, 136	36.01	0.896
6X-1, 12	40.12	0.780
6X-1, 26	40.26	0.827
6X-1, 49	40.49	0.855
6X-1, 70	40.70	0.872
6X-1, 93	40.93	1.066
6X-1, 108	41.08	1.208
6X-1, 118	41.18	1.045
6X-1, 131	41.31	0.976
6X-1, 144	41.44	1.011
6X-3, 10	43.10	1.079
6X-3, 20	43.20	1.126
6X-3, 33	43.33	1.095
6X-3, 43	43.43	1.067
6X-3, 53	43.53	0.951
6X-3, 63	43.63	1.217
6X-3, 73	43.73	0.799
6X-3, 78	43.78	0.893
6X-3, 88	43.88	0.892
6X-4, 6	44.08	1.071
6X-4, 17	44.19	0.869
6X-4, 29	44.31	0.974
6X-4, 39	44.41	1.108
6X-4, 44	44.46	1.451
6X-4, 50	44.52	4.222
6X-4, 60	44.62	1.101
6X-4, 66	44.68	1.215
6X-4, 72	44.74	0.941
6X-5, 3	45.01	1.247
6X-5, 6	45.04	1.166
6X-5, 13	45.11	1.285
6X-5, 25	45.23	1.135
6X-5, 40	45.38	1.073
6X-5, 54	45.52	1.110
6X-5, 67	45.65	1.042
6X-5, 70	45.68	1.432
6X-5, 79	45.77	1.050
7X-2, 16	51.19	1.168
7X-2, 17	51.20	0.985
7X-2, 27	51.30	1.222
7X-2, 37	51.40	1.035
7X-2, 47	51.50	0.942
7X-2, 57	51.60	0.999
7X-2, 62	51.65	1.076
7X-2, 72	51.75	1.091
7X-2, 85	51.88	1.040
7X-2, 95	51.98	1.059

Table T14 (continued).

Core, section, interval (cm)	Depth (mbsf)	Resistivity (Ωm)
7X-2, 105	52.08	1.060
7X-2, 116	52.19	1.048
7X-2, 126	52.29	1.079
7X-2, 136	52.39	1.135
7X-2, 146	52.49	1.054
7X-3, 4	52.57	1.075
7X-3, 22	52.75	0.952
7X-3, 37	52.90	0.972
7X-3, 52	53.05	1.049
7X-3, 61	53.14	1.232
7X-3, 71	53.24	1.344
7X-4, 3	53.57	0.972
7X-4, 13	53.67	0.241
8X-1, 5	59.45	0.528
8X-1, 15	59.55	0.470
8X-1, 25	59.65	46.962
8X-1, 35	59.75	0.615
8X-1, 45	59.85	0.657
8X-1, 55	59.95	0.579
8X-1, 65	60.05	0.623
8X-1, 75	60.15	0.641
8X-1, 85	60.25	0.728
9X-2, 33	70.93	0.837
9X-2, 43	71.03	0.812
9X-2, 53	71.13	0.673
9X-2, 63	71.23	0.710
9X-2, 73	71.33	0.689
9X-2, 79	71.39	1.130
9X-2, 89	71.49	1.025
9X-2, 95	71.55	0.814
9X-2, 99	71.59	1.172
9X-2, 109	71.69	1.120
9X-2, 119	71.79	0.680
9X-2, 129	71.89	0.802
9X-2, 139	71.99	0.769
9X-3, 5	72.15	1.001
9X-3, 15	72.25	0.710
9X-3, 25	72.35	0.647
9X-3, 35	72.45	0.795
9X-3, 45	72.55	0.726
9X-3, 55	72.65	0.737
9X-3, 63	72.73	0.904
9X-4, 10	73.26	0.819
9X-4, 20	73.36	0.926
9X-4, 30	73.46	0.760
9X-4, 40	73.56	0.882
9X-4, 50	73.66	0.928
9X-4, 60	73.76	1.274
9X-4, 65	73.81	1.007
9X-4, 80	73.96	0.967
9X-4, 90	74.06	0.910
9X-4, 100	74.16	1.143
10X-1, 10	78.80	0.581
10X-1, 20	78.90	0.714
10X-1, 30	79.00	0.773
10X-1, 40	79.10	0.668
10X-1, 45	79.15	0.765
10X-1, 55	79.25	0.607
10X-1, 65	79.35	0.666
10X-1, 75	79.45	0.806
10X-1, 85	79.55	0.667
10X-1, 95	79.65	0.725
10X-1, 105	79.75	1.622
10X-1, 115	79.85	0.739
10X-1, 130	80.00	0.679
10X-1, 140	80.10	0.821
311-U1326D-2X-1, 40	88.80	1.129
2X-1, 50	88.90	1.084
2X-1, 60	89.00	1.087
2X-1, 68	89.08	0.814
2X-1, 121	89.61	0.962
2X-1, 135	89.75	1.232
2X-1, 145	89.85	1.164
2X-1, 147	89.87	1.047
2X-1, 149	89.89	0.886
2X-3, 9	91.49	1.172
2X-3, 19	91.59	0.999
2X-3, 29	91.69	1.078
2X-3, 39	91.79	0.928
2X-3, 49	91.89	1.109
2X-3, 59	91.99	1.040
2X-3, 69	92.09	1.056
2X-3, 83	92.23	1.111
2X-3, 96	92.36	0.991
2X-3, 106	92.46	1.122
2X-3, 117	92.57	1.023
2X-3, 136	92.76	1.121
2X-3, 142	92.82	0.906
2X-4, 5	92.95	1.116
2X-4, 26	93.16	0.852
2X-4, 41	93.31	1.060
2X-4, 49	93.39	0.714
2X-4, 57	93.47	0.920
2X-4, 78	93.68	0.901
2X-4, 90	93.80	1.046
2X-4, 107	93.97	1.018
2X-4, 116	94.06	0.926
2X-4, 127	94.17	0.932
2X-4, 136	94.26	1.218
2X-4, 146	94.36	1.009
2X-5, 4	94.44	1.034
2X-5, 16	94.56	1.032
2X-5, 25	94.65	0.954
2X-5, 32	94.72	1.105
2X-5, 42	94.82	1.035
2X-5, 58	94.98	0.809
2X-5, 71	95.11	1.126
2X-5, 82	95.22	1.201
2X-5, 92	95.32	0.908
2X-6, 20	96.04	0.865
2X-6, 30	96.14	1.061
2X-6, 38	96.22	1.160
2X-6, 48	96.32	1.191
2X-6, 58	96.42	1.037
2X-6, 68	96.52	1.068
2X-6, 84	96.68	1.104
2X-6, 89	96.73	1.064
3X-1, 6	98.16	0.775
3X-1, 21	98.31	0.825
3X-1, 30	98.40	0.846
3X-1, 36	98.46	1.066
3X-1, 46	98.56	0.994
3X-1, 56	98.66	1.029
3X-1, 65	98.75	0.973
3X-1, 75	98.85	0.997
3X-1, 80	98.90	1.101
3X-1, 90	99.00	1.010
3X-1, 98	99.08	0.960
3X-1, 108	99.18	1.047
3X-1, 118	99.28	0.911
3X-1, 127	99.37	0.913
3X-3, 14	101.24	1.470
3X-3, 24	101.34	1.431
3X-3, 34	101.44	1.506
3X-3, 44	101.54	1.179
3X-3, 54	101.64	1.220
3X-3, 64	101.74	1.324
3X-3, 74	101.84	1.253
3X-3, 85	101.95	1.162
3X-3, 95	102.05	1.282
3X-3, 105	102.15	1.549
3X-3, 115	102.25	1.361
3X-3, 125	102.35	1.630
3X-3, 140	102.50	1.426
3X-4, 6	102.66	1.374
3X-4, 16	102.76	1.342
3X-4, 26	102.86	1.241
3X-4, 36	102.96	1.706
3X-4, 46	103.06	1.446
3X-4, 56	103.16	1.478
3X-5, 10	103.89	1.475
3X-5, 20	103.99	1.884
3X-5, 30	104.09	1.583
3X-5, 40	104.19	1.708
3X-5, 50	104.29	1.448
3X-5, 62	104.41	1.804
4X-1, 11	107.81	1.042
4X-1, 21	107.91	0.831
4X-1, 31	108.01	1.018
4X-1, 41	108.11	0.702
4X-1, 51	108.21	0.984
4X-1, 61	108.31	0.794
4X-1, 71	108.41	0.909
4X-1, 81	108.51	0.933
4X-1, 91	108.61	0.832
4X-1, 102	108.72	1.068
4X-1, 112	108.82	1.017
4X-1, 122	108.92	0.831
4X-1, 132	109.02	0.830
4X-1, 142	109.12	0.689
4X-3, 6	110.76	1.142
4X-3, 20	110.90	0.980
4X-3, 30	111.00	1.224
4X-3, 40	111.10	1.169
4X-4, 6	111.82	1.014
4X-4, 21	111.97	0.896
4X-4, 31	112.07	1.224
4X-4, 41	112.17	1.175
4X-4, 55	112.31	1.158
4X-4, 65	112.41	1.072
4X-4, 74	112.50	1.041
4X-4, 84	112.60	1.041
4X-4, 94	112.70	0.889
4X-4, 98	112.74	1.157
4X-4, 108	112.84	1.073
4X-4, 118	112.94	1.000
4X-4, 130	113.06	1.037
4X-5, 6	113.17	0.990
4X-5, 16	113.27	1.103
4X-5, 26	113.37	1.125
4X-5, 36	113.47	1.173
4X-5, 46	113.57	1.286
4X-5, 56	113.67	1.312
4X-5, 66	113.77	1.198
4X-5, 73	113.84	1.291
4X-5, 83	113.94	1.323
4X-5, 105	114.16	1.056
4X-6, 17	114.74	1.027
4X-6, 24	114.81	1.190
4X-6, 32	114.89	1.320
5X-1, 6	117.36	0.966
5X-1, 32	117.62	0.948
5X-1, 54	117.84	0.965
5X-1, 83	118.13	1.158
5X-1, 103	118.33	1.376
5X-1, 124	118.54	1.151
5X-2, 15	118.85	0.979
5X-2, 33	119.03	1.612
5X-2, 55	119.25	0.992
5X-2, 75	119.45	1.078
5X-2, 97	119.67	0.947
5X-2, 126	119.96	1.124
5X-4, 12	121.66	1.145
5X-4, 26	121.80	1.420
5X-4, 46	122.00	0.950
5X-4, 66	122.20	0.990
5X-4, 86	122.40	0.986
5X-4, 106	122.60	1.408
5X-5, 5	123.09	1.310
5X-5, 25	123.29	1.564
5X-6, 10	123.70	1.182
5X-6, 30	123.90	1.438
5X-6, 50	124.10	1.928
5X-6, 73	124.33	1.671
6X-1, 10	127.10	0.885
6X-1, 30	127.30	0.679
6X-1, 50	127.50	0.714
6X-1, 70	127.70	0.740
6X-1, 90	127.90	0.922
6X-1, 110	128.10	1.714
6X-3, 10	130.10	0.692
6X-3, 30	130.30	0.702
6X-3, 50	130.50	1.063
6X-3, 70	130.70	0.811
6X-3, 90	130.90	0.794
6X-4, 9	131.22	0.918
6X-4, 29	131.42	0.898
6X-4, 49	131.62	0.963
6X-4, 71	131.84	0.884
6X-4, 83	131.96	0.948
6X-5, 8	132.53	1.374
6X-5, 28	132.73	0.963
6X-5, 48	132.93	1.187
6X-5, 68	133.13	1.319
6X-5, 88	133.33	0.948
6X-6, 11	133.56	0.934
6X-6, 31	133.76	0.904
6X-6, 55	134.00	1.067
6X-6, 79	134.24	0.883
7X-1, 8	136.68	0.754
7X-1, 28	136.88	0.738
7X-1, 48	137.08	0.683
7X-1, 68	137.28	0.903
7X-2, 9	137.65	0.770
7X-2, 10	137.66	0.939
7X-2, 29	137.85	0.747
7X-2, 49	138.05	0.717
7X-2, 69	138.25	0.816
7X-2, 89	138.45	1.046
7X-4, 30	140.49	0.788
7X-4, 50	140.69	0.839
7X-4, 70	140.89	1.093
7X-4, 92	141.11	0.893
7X-4, 112	141.31	0.964
7X-4, 132	141.51	1.166
8X-1, 13	146.43	0.882
8X-1, 29	146.59	0.557
8X-3, 15	148.91	0.657
8X-3, 35	149.11	1.238
8X-3, 49	149.25	0.661
8X-3, 55	149.31	1.720

Table T14 (continued).

Core, section, interval (cm)	Depth (mbsf)	Resistivity (Ωm)
8X-3, 75	149.51	2.158
8X-3, 95	149.71	0.830
8X-3, 98	149.74	0.824
8X-3, 118	149.94	0.871
8X-3, 133	150.09	0.944
8X-4, 6	150.20	1.952
8X-4, 13	150.27	1.454
8X-4, 23	150.37	0.952
8X-4, 32	150.46	1.277
9X-1, 7	155.97	0.558
9X-1, 31	156.21	0.911
9X-1, 51	156.41	0.579
9X-1, 74	156.64	0.672
9X-2, 10	157.34	0.782
9X-2, 30	157.54	1.031
9X-2, 33	157.57	1.161
9X-2, 44	157.68	1.015
9X-3, 8	157.79	0.718
9X-3, 12	157.83	3.236
9X-4, 7	158.18	1.085
9X-4, 17	158.28	1.136
9X-4, 30	158.41	1.391
10X-1, 49	166.09	0.769
10X-1, 65	166.25	0.942
10X-1, 85	166.45	0.943
10X-1, 105	166.65	0.991
10X-1, 125	166.85	0.927
10X-2, 17	167.27	0.989
10X-2, 37	167.47	0.729
10X-2, 56	167.66	1.098
10X-2, 68	167.78	1.157
10X-2, 88	167.98	0.990
10X-3, 6	168.58	0.946
10X-3, 16	168.68	1.001
10X-3, 26	168.78	0.842
10X-3, 36	168.88	1.134
10X-3, 52	169.04	0.684
10X-3, 62	169.14	0.776
10X-3, 116	169.68	1.128
10X-3, 126	169.78	1.047
10X-4, 13	170.15	1.215
10X-4, 26	170.28	1.715
10X-4, 41	170.43	1.205
10X-4, 55	170.57	1.343
10X-4, 67	170.69	1.694
10X-4, 77	170.79	1.481
10X-4, 87	170.89	1.416
11X-1, 9	175.29	0.767
11X-1, 19	175.39	0.938
11X-2, 5	175.74	0.631
11X-2, 25	175.94	0.597
11X-2, 50	176.19	0.829
11X-2, 67	176.36	1.519
11X-2, 77	176.46	1.504
11X-2, 87	176.56	0.972
11X-2, 118	176.87	1.259
11X-4, 8	178.77	2.070
11X-4, 18	178.87	1.626
11X-4, 25	178.94	1.363
11X-4, 48	179.17	0.888
11X-4, 74	179.43	1.218
11X-4, 93	179.62	0.776
11X-5, 12	180.31	0.890
11X-5, 23	180.42	1.151
11X-5, 53	180.72	1.428
11X-5, 66	180.85	1.701
11X-5, 86	181.05	1.214
11X-5, 110	181.29	0.904
12X-1, 6	184.86	0.744
12X-1, 16	184.96	0.813
12X-1, 37	185.17	0.866
12X-1, 47	185.27	0.945
12X-1, 65	185.45	1.003
12X-2, 10	186.15	0.768
12X-2, 20	186.25	0.953
12X-2, 30	186.35	0.823
12X-2, 45	186.50	0.916
12X-2, 58	186.63	0.782
12X-2, 75	186.80	0.844
12X-2, 97	187.02	0.946
12X-2, 110	187.15	1.029
12X-2, 133	187.38	1.061
12X-2, 146	187.51	1.064
12X-4, 6	189.11	1.042
12X-4, 16	189.21	0.989
12X-4, 26	189.31	1.027
12X-4, 38	189.43	1.314
12X-4, 48	189.53	1.580
12X-4, 64	189.69	1.180
12X-5, 23	189.95	1.475
12X-5, 38	190.10	1.406
12X-5, 58	190.30	1.390
12X-5, 70	190.42	1.583
13X-1, 37	194.77	0.832
13X-1, 70	195.10	0.785
13X-1, 90	195.30	1.055
13X-3, 11	197.11	0.978
13X-3, 21	197.21	1.331
13X-3, 31	197.31	1.194
13X-3, 41	197.41	0.868
13X-3, 51	197.51	1.055
13X-3, 90	197.90	1.126
13X-4, 4	198.04	0.963
13X-4, 15	198.15	0.968
13X-4, 25	198.25	1.351
13X-4, 33	198.33	1.142
13X-4, 44	198.44	1.006
13X-4, 54	198.54	1.363
14X-1, 37	204.37	0.799
14X-1, 47	204.47	1.000
14X-1, 57	204.57	1.019
14X-1, 101	205.01	0.924
14X-3, 9	206.36	0.926
14X-3, 19	206.46	0.742
14X-3, 39	206.66	0.920
14X-3, 49	206.76	0.889
14X-4, 11	207.11	0.930
14X-4, 22	207.22	1.394
14X-4, 32	207.32	1.045
14X-4, 42	207.42	1.301
14X-4, 62	207.62	0.946
14X-4, 111	208.11	1.045
14X-4, 121	208.21	1.366
14X-4, 134	208.34	1.620
14X-5, 71	209.21	1.785
14X-5, 81	209.31	1.302
14X-5, 93	209.43	1.057
14X-5, 99	209.49	1.508
14X-6, 4	209.54	2.347
14X-6, 10	209.60	3.881
14X-6, 43	209.93	2.078
14X-6, 53	210.03	1.012
15X-1, 20	213.80	1.060
15X-1, 30	213.90	0.944
15X-1, 40	214.00	1.062
15X-1, 76	214.36	1.006
15X-1, 91	214.51	1.088
15X-1, 114	214.74	0.938
15X-1, 129	214.89	1.101
15X-2, 6	215.08	1.393
15X-2, 21	215.23	0.991
15X-2, 42	215.44	1.235
15X-2, 52	215.54	19.786
15X-2, 62	215.64	1.020
15X-2, 93	215.95	0.909
15X-2, 107	216.09	1.079
15X-2, 115	216.17	1.207
15X-2, 124	216.26	1.064
15X-2, 131	216.33	1.050
15X-3, 6	216.42	1.028
15X-3, 20	216.56	1.037
15X-3, 36	216.72	1.033
15X-3, 46	216.82	1.159
15X-3, 65	217.01	1.687
15X-3, 79	217.15	2.322
15X-3, 89	217.25	1.198
15X-5, 8	219.44	0.990
15X-5, 18	219.54	1.087
15X-5, 28	219.64	1.013
15X-5, 38	219.74	0.978
15X-5, 43	219.79	1.239
15X-6, 7	220.43	1.988
15X-6, 17	220.53	1.178
15X-6, 27	220.63	1.506
15X-6, 37	220.73	1.386
15X-6, 47	220.83	2.083
16X-1, 10	223.40	1.338
16X-1, 37	223.67	1.002
16X-1, 54	223.84	0.921
16X-1, 78	224.08	1.291
16X-1, 88	224.18	2.544
16X-1, 111	224.41	1.697
16X-1, 130	224.60	1.383
16X-2, 42	225.22	2.879
16X-2, 58	225.38	1.664
16X-2, 78	225.58	1.856
16X-2, 92	225.72	1.153
16X-2, 119	225.99	0.783
16X-4, 8	227.88	1.587
16X-4, 23	228.03	0.752
16X-4, 57	228.37	0.785
16X-4, 74	228.54	1.147
16X-4, 90	228.70	1.008
16X-4, 107	228.87	1.078
16X-5, 63	229.53	1.208
16X-5, 73	229.63	1.000
16X-5, 83	229.73	1.166
16X-5, 97	229.87	1.035
16X-5, 109	229.99	1.476
17X-1, 8	232.98	0.638
17X-1, 18	233.08	0.736
17X-1, 28	233.18	0.484
17X-1, 38	233.28	0.624
17X-1, 48	233.38	0.662
17X-1, 68	233.58	1.086
17X-1, 88	233.78	0.816
17X-1, 108	233.98	1.257
17X-1, 136	234.26	0.829
17X-3, 108	236.98	0.965
17X-3, 118	237.08	1.170
17X-3, 130	237.20	1.249
17X-3, 146	237.36	1.011
17X-4, 8	237.48	1.404
17X-4, 28	237.68	0.781
17X-4, 48	237.88	0.893
17X-4, 56	237.96	1.016
17X-4, 74	238.14	0.794
17X-4, 100	238.40	0.997
17X-4, 112	238.52	1.175
17X-4, 127	238.67	1.130
17X-5, 9	238.99	1.400
17X-5, 16	239.06	1.264
17X-5, 30	239.20	1.036
17X-5, 42	239.32	0.918
17X-5, 53	239.43	1.095
17X-5, 76	239.66	1.534
17X-5, 96	239.86	1.240
17X-5, 116	240.06	0.666
17X-5, 126	240.16	0.770
17X-5, 140	240.30	0.736
17X-6, 14	240.48	1.097
17X-6, 28	240.62	1.247
17X-6, 37	240.71	1.105
17X-6, 52	240.86	0.968
18X-2, 7	243.72	0.875
18X-2, 30	243.95	0.979
18X-2, 57	244.22	0.616
18X-2, 80	244.45	1.076
20X-1, 4	261.84	0.488
20X-1, 42	262.22	0.801
20X-1, 54	262.34	1.936
20X-3, 10	263.85	1.083
20X-3, 30	264.05	1.140
20X-3, 50	264.25	1.575
20X-3, 70	264.45	1.107
20X-3, 90	264.65	0.905
20X-3, 110	264.85	1.299
20X-3, 123	264.98	1.195
20X-4, 6	265.10	0.748
20X-4, 26	265.30	0.908
20X-4, 42	265.46	0.943
20X-5, 8	266.62	0.744
20X-5, 28	266.82	1.238
20X-5, 48	267.02	1.764
20X-5, 72	267.26	0.907
20X-5, 85	267.39	1.350
20X-5, 111	267.65	1.778
20X-5, 131	267.85	1.258
20X-7, 9	269.13	0.344
20X-7, 13	269.17	0.788
20X-7, 33	269.37	0.790
20X-7, 33	269.37	1.222
20X-7, 53	269.57	1.138
20X-7, 71	269.75	1.163
20X-7, 81	269.85	1.113
20X-7, 102	270.06	1.242

Table T15. Thermal conductivity, Holes U1326B, U1326C, and U1326D.

Core, section, interval (cm)	Depth (mbsf)	Thermal conductivity (W/[m·K])			
		Average	1	2	3
311-U1326B-					
1H-1, 68	0.68	1.027	1.006	1.040	1.036
311-U1326C-					
1H-2, 37	1.87	0.881	0.888	0.875	0.879
2H-2, 27	5.67	1.134	1.145	1.148	1.108
2H-4, 42	8.82	0.973	0.971	0.974	0.974
2H-6, 50	11.90	0.986	0.984	0.986	0.987
3H-2, 26	15.16	1.172	1.182	1.158	1.175
3H-4, 37	18.27	1.198	1.194	1.200	1.201
3H-6, 72	21.62	1.173	1.170	1.172	1.178
4H-1, 92	23.82	1.226	1.227	1.231	1.219
4H-3, 104	26.94	0.894	0.893	0.893	0.897
5X-1, 29	30.69	1.042	0.970	1.062	1.094
6X-1, 73	40.73	0.820	0.815	0.826	0.820
6X-3, 30	43.30	1.061	1.061	1.058	1.063
7X-3, 11	52.64	1.208	1.208	1.208	1.208
8X-1, 25	59.65	1.037	1.021	1.041	1.050
9X-2, 53	71.13	1.048	1.052	1.047	1.046
9X-2, 66	71.26	1.078	1.077	1.075	1.082
10X-1, 53	79.23	1.048	1.059	1.045	1.040
311-U1326D-					
2X-3, 99	92.39	0.965	0.963	0.967	0.966
2X-4, 134	94.24	1.259	1.253	1.252	1.273
3X-4, 28	102.88	0.965	0.967	0.965	0.964
3X-5, 28	104.07	0.960	0.962	0.959	0.959
4X-1, 16	107.86	0.971	0.991	0.962	0.960
4X-5, 32	113.43	1.305	1.295	1.314	1.307
5X-1, 130	118.60	1.014	1.010	1.017	1.016
5X-4, 47	122.01	0.903	0.908	0.903	0.898
6X-1, 85	127.85	1.218	1.219	1.218	1.217
6X-4, 27	131.40	1.122	1.122	1.121	1.122
6X-6, 26	133.71	1.151	1.150	1.151	1.153
7X-1, 43	137.03	0.779	0.796	0.789	0.751
7X-3, 76	139.50	1.325	1.310	1.332	1.333
8X-2, 29	148.09	1.130	1.128	1.130	1.133
8X-4, 29	150.43	0.949	0.949	0.948	0.951
9X-2, 35	157.59	1.085	1.093	1.092	1.069
10X-1, 65	166.25	1.260	1.263	1.260	1.258
10X-3, 52	169.04	1.067	1.067	1.067	1.067
11X-2, 102	176.71	1.069	1.083	1.064	1.060
11X-4, 56	179.25	1.180	1.186	1.177	1.178
12X-1, 32	185.12	0.832	0.832		
12X-4, 11	189.16	1.272	1.282	1.271	1.264
13X-3, 69	197.69	0.718	0.720	0.716	0.717
13X-4, 27	198.27	1.006	1.000	1.010	1.008
14X-3, 21	206.48	0.287	0.279	0.294	
14X-6, 11	209.61	1.026	1.038	1.021	1.020
15X-2, 40	215.42	0.875	0.878	0.874	0.873
15X-6, 31	220.67	1.240	1.238	1.244	1.237
16X-4, 55	228.35	0.912	0.921	0.911	0.904
16X-5, 51	229.41	1.215	1.219	1.206	1.219
17X-3, 9	235.99	1.329	1.331	1.329	1.327
17X-5, 56	239.46	0.996	0.998	0.994	0.996
19X-1, 20	252.40	1.053	1.058	1.049	1.052
20X-3, 62	264.37	1.247	1.249	1.241	1.251
20X-5, 85	267.39	1.220	1.206	1.218	1.236

Table T16. In situ temperature, Holes U1326C and U1326D.

Core	Depth (mbsf)	Temperature (°C)		Thermal conductivity (W/[m·K])	Calibration correction (°)	Temperature tool	Solution reliability
		Corrected	Uncorrected				
311-U1326C-							
4H	30.4	4.3	4.3	1.1	0	APCT-3	Very good
311-U1326D-							
19X	252	NA*	NA	1.1	0	DVTP	Poor (heave)
21X	271.4	NA	NA	1.1	0	DVTP	Fair (heave)
Base of hole	300	NA	NA	1.1	0	DVTP	Fair (heave)

Notes: NA = not available. * = tool did not stay in the seafloor long enough to obtain an in situ temperature reading using CONEFIT; these data will be modeled postcruise in an attempt to place an upper bound on the in situ temperature. APCT-3 = third-generation advanced piston corer temperature tool, DVTP = Davis-Villinger Temperature Probe.

Table T17. Summary of pressure coring operations at Site U1326.

Core	Core-top depth (mbsf)	Length recovered (cm)*	Length curated (cm)	Pressure at core depth (MPa)	Pressure recovered (MPa)		Comments
					Logged†	Gauge‡	
311-U1326C-							
11Y	82.7	15	15	19.2	17.5	17.5	Sand in bottom-hole assembly
12P	83.7	35–40	27	19.2	3.4	3.4	Normal operation
13E	85.7	0	0	19.2	0	—	Reversal of motor unscrewed joints and left bit in hole

Notes: Water depth at Site U1326C is 1828 mbsl. P = Pressure Core Sampler (PCS), Y = Fugro Percussion Corer (FPC), E = HYACE Rotary Corer (HRC). * = based on X-ray imaging and gamma ray density profiling prior to degassing. † = last pressure recorded before data logger disconnected from corer autoclave. Temperature 2°–4°C unless otherwise noted. ‡ = pressure measured when autoclave pressure transducer connected to computer (PCS cores) or external gauge (PCS, FPC, HRC cores). Pressure measured at 7°C unless otherwise noted. — = no data.

Table T18. In situ conditions of PCS cores recovered from Site U1326.

Core	Depth (mbsf)		Temperature (°C)	Pressure (MPa)	Salinity	Methane saturation (mM)
	Top	Bottom				
311-U1326C-						
12P	83.7	84.7	8.1	19.2	32.0	64.0

Notes: Background salinity was extrapolated from adjacent cores (Table T3). Temperature was calculated from sediment depth assuming a seafloor temperature of 3.03°C and a thermal gradient of 60.0°C/km. Pressure was calculated from sediment and water depth (1828 mbsl). Methane saturation was calculated based on sediment and water depth, seafloor temperature, thermal gradient, and salinity according to Xu (2002, 2004).

Table T19. Results from degassing experiments at Site U1326.

Core	Total volume of gas released (mL)	Total volume of methane released (mL)	Average concentration of released gas components (%)*					Total volume of water released (mL)	Salinity of released water	Temperature during degassing (°C)	Air pressure during degassing (MPa)
			C_1	C_2†	CO_2	N_2	C_1/C_2†				
311-U1326C-											
12P	20,960	19,086	91.7	0.0054	BD	6.1	16,929	486	—	7.1 ± 0.5	0.1013

Notes: * = excludes initially released gas increments that are diluted by dead volume of manifold system. † = subset of seven samples analyzed using methods described in **"Organic geochemistry"** in the "Methods" chapter. BD = below detection limit, — = no data.

Table T20. Characteristics of PCS core used for mass balance calculations, Site U1326.

Core	Core length recovered (m)	Sediment volume in inner core barrel (mL)	Porosity (%)	Pore water volume in inner core barrel (mL)	Volume of water in outer core barrel (mL)	Sediment extruded with outer core barrel water, dry weight (g)	Headspace volume in outer core barrel (mL)	Salinity of water in outer core barrel
311-U1326C-12P	0.40	586	49	288	2,850	801	114	31.0

Table T21. Mass balance calculations based on degassing experiments, Site U1326.

Core	Depth (mbsf) Top	Depth (mbsf) Bottom	Total C_1 released (10^{-3} mole)	C_1 concentration (mM) Total	At laboratory conditions Dissolved*	At laboratory conditions Free†	In situ Dissolved‡	In situ Nondissolved	In situ nondissolved C_1 as percentage of pore volume if present as Free gas	In situ nondissolved C_1 as percentage of pore volume if present as Gas hydrate	Potential pore water freshening caused by gas hydrate decomposition Water release (mL)	Potential pore water freshening caused by gas hydrate decomposition Freshening (%)
311-U1326C-12P	83.7	84.7	855	2965	1.8	2963	64.0	2901	35	40	90	18

Notes: * = extrapolated from analysis of Sample 311-U1326C-10X-1, 145–150 cm. † = calculated based on the total amount of C_1 released during the degassing experiment and the pore water volume recovered by the PCS. ‡ = methane saturation from Table **T18.**